# A COMPUTATIONAL STUDY OF THE STRUCTURAL, ELECTRONIC, OPTICAL AND THERMAL PROPERTIES OF HEXAGONAL AND CUBIC GERMANIUM-ANTIMONY-TELLURIDE

BY

HENRY ODHIAMBO OTUNGA

A THESIS SUBMITTED IN FULFILMENT OF THE REQUIREMENTS FOR THE DEGREE OF DOCTOR OF PHILOSOPHY IN PHYSICS

DEPARTMENT OF PHYSICS AND MATERIALS SCIENCE

MASENO UNIVERSITY

# Declaration of Authorship

This thesis is my original work and has not been presented for a degree award in any university or institution.

**Henry Odhiambo Otunga**: PG/PhD/0034/2008

Signature:.....Date:.....

Department of Physics and Materials Science, Maseno University.

This thesis has been submitted to the School of Graduate Studies (SGS), Maseno University, with our approval as university supervisors.

**Prof. George Amolo**

Signature:.....Date:.....

Department of Physics and Space Science, Technical University of Kenya.

**Prof. Herick Othieno**

Signature:.....Date:.....

Department of Physics and Materials Science, Maseno University.

**Prof. Andrew Oduor**

Signature:.....Date:.....

Department of Physics and Materials Science, Maseno University.

# Acknowledgement

First and foremost, I would like to thank God for giving me the wisdom, strength, support and knowledge during the study.

I sincerely acknowledge my family for their support and encouragement during the course of the study.

I would like to extend my sincere thanks to my supervisors George Amolo (assisted by Nicholas Makau), Herick Othieno and Andrew Oduor for giving thought, advice and ideas for improvement of the study.

I offer my profound gratitude to the developers of Quantum ESPRESSO and Yambo computer codes. This work was mainly done using Quantum ESPRESSO and Yambo computer packages.

I take immense pleasure to express my sincere and deep sense of gratitude to the management and staff of the Center for High Performance Computing, Cape Town, Republic of South Africa, for allowing me access to their super-computing facilities.

I am grateful to the African School on Electronic Structure Methods and Applications (ASESMA) for their hands-on tutorials.

I also thank Maseno University for hosting and financing the study.

# Dedication

To developers and users of Quantum ESPRESSO and Yambo computer codes

# Abstract

The electronic, optical and thermal properties of hexagonal and cubic phases of $Ge_2Sb_2Te_5$ (GST) have been calculated using density functional theory (DFT) as implemented in the Quantum ESPRESSO computer package. GST is successfully applied in optical memory such as rewritable CDs and is a promising candidate for non-volatile electronic memory. In optical storage, the reflectivity contrast can be optimized towards the ultraviolet spectral range, thereby increasing data storage capacity and doping with nitrogen is one way to achieve this aim. In this study, the reflectivity of pure and nitrogen-doped GST have been computed from the dielectric function, which is obtainable from DFT calculations. We show that nitrogen doped GST has a higher reflectivity contrast in the blue and ultraviolet spectral range and this reflectivity contrast increases with rising nitrogen content for 10-20 at. % doping levels. Because DFT underestimates band gaps of semiconductors and insulators, since it is a ground-state theory and does not take into account many-body effects, the Liouville-Lanczos approach to time-dependent density functional theory (TDDFT) has been employed giving optical band gaps of about 0.48 eV and 0.66 eV for hexagonal and cubic phases, respectively. This is in reasonably good agreement with optical measurements which suggest a value of 0.5 eV for both phases. Analyzing the thermal properties of GST can be useful in validating the structural models such as those used in this study. Thermal properties have been calculated using the quasi-harmonic approximation. The specific heat of both phases is found to exceed the classical Dulong-Petit limit at high temperatures in agreement with experiment. The heat capacity curves are found to exhibit the same trend as experimental curves. The entropy of the hexagonal phase is found to vanish at 0 K, in agreement with experiment.

# Table of Contents

# List of Tables

# List of Figures

# List of Appendices

# Chapter 1
# Introduction

## 1.1 Introduction

Phase-change materials show a significant change in optical as well as electronic properties upon undergoing a reversible crystalline-to-amorphous phase transition. Phase-change materials are often $Te$-based semiconducting or semimetallic alloys, such as those on the pseudobinary line $(GeTe)_m(Sb_2Te_3)_n$ or $AgInSbTe$.

Upon phase transition, which is the result of a rearrangement in the microscopic structure [1–3], the electrical conductivity can change by several orders of magnitude [1] whereas the optical reflectivity can change (depending on layer thickness and wavelength) by up to 30% [4]. Phase-change materials have been successfully applied in optical storage media such as rewritable compact disks (RW-CDs), digital versatile disks (DVDs) and blu-ray disks and are possible candidates for a new generation of non-volatile electronic storage devices known as phase-change random access memory (PCRAM) [1, 5, 6].

In optical storage, information is written using a focused laser beam to locally melt the crystalline material and then rapidly quenching it. This results in an amorphous part of the material which exhibits a lower reflectivity than the surrounding crystalline background. Erasure is achieved by heating this amorphous region above the crystallization temperature and thereafter gently quenching it. The current state of a region on the storage device is then read by a low-intensity laser pulse.

In electronic data storage, electric pulses are used to switch the material between amorphous and crystalline phases. The difference in electrical conductivity between the amorphous and crystalline phases is used to store data.

Among phase-change materials, $Ge_2Sb_2Te_5$ (GST) is the most widely ap-

plied and is the focus of scientific research because of its enhanced properties in terms of speed of transition ($\cong$ 50 ns), thermal stability and cyclability (the number of write-erase cycles that can be performed by a storage device) [7]. Most current applications of GST exploit the reversible amorphous-to-crystalline phase transition. However, including the hexagonal phase offers the possibility of a tri-state memory, hence the importance of hexagonal GST.

## 1.2 Statement of the Problem

First principles calculation of thermal properties such as heat capacity and entropy are useful in validating structural models such as those used in this study. By the time of writing, there was no first principles calculation of the heat capacity of the cubic GST phase in the available literature. Also lacking in the available literature is first principles calculation of the entropy of both hexagonal and cubic GST.

Density functional theory (DFT) is known to underestimate band gaps of insulators and semiconductors since it is a ground-state theory and does not take into account many-body effects. Processes such as inter-band transitions that involve electronic excitations are accounted for by post-DFT theories that include many body perturbation theory (MBPT) and time dependent density functional theory (TDDFT). In this study, a computationally efficient approach to TDDFT, known as Liouville-Lanczos method has been used to estimate the band gap of hexagonal and cubic GST.

The range of application of GST in optical storage is in the infrared. However, to increase data storage density it would be necessary to optimize the reflectivity contrast towards shorter wavelengths (blue and ultraviolet spectral range). Doping with impurity atoms such as nitrogen is one way to achieve this. At the time of writing, no theoretical study had investigated this concept.

## 1.3 Objectives of the Study

The objectives of this study are:

1. To compute the temperature dependence of the heat capacity of cubic $Ge_2Sb_2Te_5$ and to compute the temperature dependence of the entropy of cubic and hexagonal $Ge_2Sb_2Te_5$ from first principles using QUANTUM ESPRESSO computer code.

2. To estimate the optical band gap of hexagonal and cubic $Ge_2Sb_2Te_5$ from optical absorption spectra calculated using the Liouville-Lanczos approach to TDDFT as implemented in the QUANTUM ESPRESSO computer code.

3. To investigate the effect of nitrogen doping on the optical properties of hexagonal and cubic $Ge_2Sb_2Te_5$ from first principles using QUANTUM ESPRESSO computer code.

## 1.4 Significance of the Study

First principles calculation of the heat capacity and entropy as functions of temperature are useful in validating the structural models such as those used in this study. In particular, the heat capacity can reveal the presence of lattice defects whereas the entropy can reveal the state of the structural configuration (ordered or disordered lattice).

Estimating optical band gaps from absorption spectra calculated using the Liouville-Lanczos approach to TDDFT serves to validate the theoretical model.

Reducing the wavelength of the writing laser (optimizing the reflectivity contrast towards the ultraviolet spectral range) reduces the size of the written bits thereby increasing the data storage density.

## 1.5 Limitations of the Study

This study does not consider amorphous GST since Quantum ESPRESSO only takes crystalline structures as input.

# Chapter 2
# Literature Review

## 2.1 Electronic Properties

In this section, we review *ab initio* electronic structure methods and their accuracy in the calculation of electronic band gaps.

### 2.1.1 Density Functional Theory

One of the long-standing problems in theoretical physics and chemistry is the solution of the Schrödinger equation for a many-atom interacting system. DFT is a way of approaching any interacting problem by mapping it exactly to a much easier-to-solve non-interacting problem. The main idea in DFT is the substitution of the many-electron wave-function, which contains $3N$ variables ($N$ is the number of electrons and each electron has 3 spatial coordinates) with the electron density $n(r)$ (which only depends on 3 spatial coordinates) as the main variable.

DFT rests on two fundamental mathematical theorems originally proved by Hohenberg and Kohn in 1964 [10] and the derivation of a set of equations by Kohn and Sham in 1965 [11]. The Thomas-Fermi equation [12, 13], which is a predecessor to the Kohn-Sham equations of DFT [10, 11], can be derived from DFT as an approximation.

**Theorem I**: For any system of interacting particles in an external potential $V_{ext}$, the external potential is uniquely determined, except for a constant, by the ground-state particle density, $n_{GS}(\mathbf{r})$.

*Corollary I*: Therefore, all properties of the system are completely determined

given only the ground-state density, $n_{GS}(\mathbf{r})$.

**Theorem II**: An energy functional, $E[n(\mathbf{r})]$, can be defined, valid for any external potential, $V_{ext}$. For any external potential, $V_{ext}$, the exact ground state energy of the system is the global minimum of this functional, and the density, $n(\mathbf{r})$, that minimizes the functional is the exact ground-state density, $n_{GS}(\mathbf{r})$.

*Corollary II*: The energy functional, $E[n(\mathbf{r})]$, alone is sufficient to determine the exact ground-state energy and density. In general, the excited states of electrons must be determined by other means.

The Kohn-Sham energy functional can be written as

$$E[n(\mathbf{r})] = T[n(\mathbf{r})] + \int \mathrm{d}^3\mathrm{r}\, V_{ext}(\mathbf{r})n(\mathbf{r}) + \frac{1}{2}\int \mathrm{d}^3\mathrm{r}\ \mathrm{d}^3\mathrm{r}'\, \frac{n(\mathbf{r})n(\mathbf{r}')}{|\mathbf{r}-\mathbf{r}'|} + E_{XC}[n(\mathbf{r})], \tag{2.1}$$

where $T[n(\mathbf{r})]$ is the kinetic energy of a system with density $n(\mathbf{r})$ in the absence of electron-electron interactions,

$$\int \mathrm{d}^3\mathrm{r}\, V_{ext}(\mathbf{r})n(\mathbf{r})$$

is the interaction energy of electrons and the external potential,

$$\frac{1}{2}\int \mathrm{d}^3\mathrm{r}\, \mathrm{d}^3\mathrm{r}'\, \frac{n(\mathbf{r})n(\mathbf{r}')}{|\mathbf{r}-\mathbf{r}'|}$$

is the classical Coulomb potential of electrons and $E_{XC}$ is the exchange-correlation (XC) energy functional. The variational principle applied to eqn. (2.1) under the constraint that the number of electrons is conserved yields

$$\frac{\delta E[n]}{\delta n(\mathbf{r})} = \frac{\delta T}{\delta n(\mathbf{r})} + V_{ext}(\mathbf{r}) + \int \mathrm{d}^3\mathrm{r}' \, \frac{n(\mathbf{r}')}{|\mathbf{r} - \mathbf{r}'|} + \frac{\delta E_{XC}}{\delta n(\mathbf{r})} = \mu, \tag{2.2}$$

where $\mu$ is the Lagrange multiplier associated with the requirement of constant particle number. If we compare this with the corresponding equation for a system with an effective potential $V_{eff}(\mathbf{r})$ but without electron-electron interactions,

$$\frac{\delta E[n]}{\delta n(\mathbf{r})} = \frac{\delta T}{\delta n(\mathbf{r})} + V_{eff}(\mathbf{r}) = \mu, \tag{2.3}$$

it can be seen that the mathematical problems are identical, provided that

$$V_{eff}(\mathbf{r}) = V_{ext}(\mathbf{r}) + \int \mathrm{d}^3\mathrm{r}' \, \frac{n(\mathbf{r}')}{|\mathbf{r} - \mathbf{r}'|} + \frac{\delta E_{XC}}{\delta n(\mathbf{r})}, \tag{2.4}$$

where

$$V_H = \int \mathrm{d}^3\mathrm{r}' \frac{n(\mathbf{r}')}{|\mathbf{r} - \mathbf{r}'|}$$

is the Hartree potential that describes electronic self-interaction and

$$\frac{\delta E_{XC}}{\delta n(\mathbf{r})}$$

is the exchange-correlation potential.

Hence, a system of interacting particles can be mapped onto a system of non-interacting particles using the equation

$$\left[ -\frac{\hbar^2}{2m} \nabla^2 + V_{eff}(\mathbf{r}) \right] \psi_i = \epsilon_i \psi_i, \tag{2.5}$$

where

$$n(\mathbf{r}) = \sum_{i=1}^{N} |\psi_i(\mathbf{r})|^2. \tag{2.6}$$

.

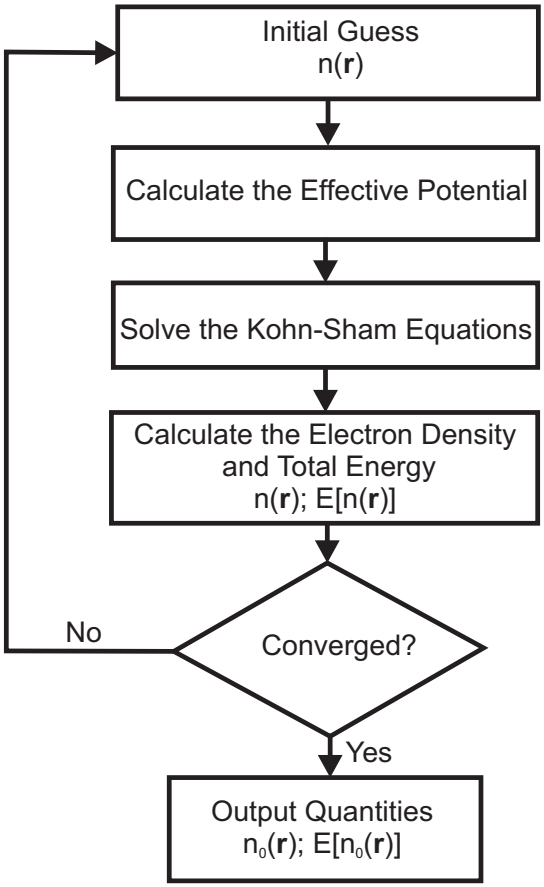


Figure 2.1: Flow diagram showing the practical implementation of DFT.

The set of single particle equations (2.5) are known as the Kohn-Sham (K-S) equations. To solve the Kohn-Sham equations [11] we need to define the Hartree potential, and to define the Hartree potential we need to know the electron density. But to define the electron density, we need to know the single-electron wave-functions and to define single-electron wave-functions we must solve the Kohn-Sham equations [11]. To break this cycle, the problem is treated in an iterative way as outlined in Fig. 2.1. Eqns. (2.5) and (2.6) are often called self-consistent field (SCF) equations and the process of solving them is known as an SCF calculation.

There is just one critical complication to this otherwise beautiful formu-

lation: To solve the single-particle Kohn-Sham equations [11], we must specify the exchange-correlation energy functional, $E_{XC}$, whose exact form is not known. Developing approximate functionals is the core problem of DFT. There are a number of approximate functionals that have been found to give good results in a large variety of physical problems. The local density approximation (LDA) uses only the local density to define the approximate exchange-correlation functional. The LDA is exact in the limit of slowly-varying densities. The local spin-density approximation (LSDA) is a straightforward generalization of the LDA to include electron spin. Numerous parameterizations for the LDA energy functional have been reported in the literature, for example, by Perdew and Zunger [14]. Although the density in systems of interest is generally rapidly varying, the use of LDA is justified *a posteriori* by its surprising success at predicting physical properties in real systems. This success may be due in part to the fact that the sum rule for the XC hole [15], which must be obeyed by the real functional, is reproduced by the LDA. The best known class of functionals after the LDA uses information about the local electron density as well as the local gradient in the electron density. This approach defines the generalized gradient approximation (GGA). In recent years, the GGA has attracted a great deal of interest as one of the simplest approaches to improve upon the LDA in first principles calculations of material properties. The success of GGA derives from its ability to correct with a modest computational workload some deficiencies of LDA. Many forms of GGA functionals have been suggested, and some of the most important (and all their parameters) are given by Filippi *et al* [16]. For example, Perdew, Burke and Ernzerhof [17] have described a functional form (PBE) that has several attractive features. The PBE functional has been shown to correct substantially cohesive energies of a large set of molecules [18] and solids [19–21], and to accurately predict bond lengths in weakly bonded systems [22–25]. However, calculations on covalent solids indicate a tendency of the PBE scheme to underestimate bulk moduli

[20, 21, 26]. Recently, Perdew and Wang have proposed a new GGA functional, the Perdew-Wang 1991 (PW91) [27], which shares several properties with the exact XC functional. The PW91 functional is more satisfactory from a conceptual point of view and it is, therefore, expected to improve over previous proposals. However, recent applications of the PW91 functional do not always confirm these expectations [28].

More recently, a new class of very promising DFT functionals based on the GGA was developed by including additional semi-local information beyond the first-order density gradient contained in the GGA. These functionals, which are termed meta-GGA (M-GGA) depend explicitly on higher order density gradients. These methods represent a significant improvement in the determination of properties such as atomization energies. However, they are more technically challenging, with several difficulties in terms of numerical stability. Several M-GGA functionals for the exchange functional, correlation functional or both have been developed. Examples include B95 [29], KCIS [30], TPSS [31] and VSXC [32].

Another group of functionals known as Hybrid GGA (H-GGA) combine the XC of a conventional GGA method with a percentage of Hartree-Fock exchange. Examples of H-GGA functionals include B3LYP [29, 33], B3P86 [29, 33], B3PW91 [29, 33], B97-1 [34], B97-2 [34], B98 [35], BH&HLYP [33, 36], MPW1K [27, 37], mPW3LYP [27, 37], O3LYP [36] and X3LYP [33, 36].

Hybrid meta-GGA (HM-GGA) functionals are based on a similar concept to the M-GGA functionals and are under active development. The difference lies in the fact that they start from M-GGA instead of standard GGAs. Hence, these methods depend on the Hartree-Fock exchange, the electron density and its gradient, and the kinetic energy density. Examples of HM-GGA XC functionals include B1B95 [29, 33], BB1K [29, 33], MPW1B95 [29, 37], MPW1KCIS [27, 37], PBE1KCIS [17, 30], TPSS1KCIS [30, 31] and TPSSh [31]. These methods represent an improvement over the previous formalisms,

particularly in the determination of barrier heights and atomization energies. It is clear from the foregoing discussion that density functional calculations cover a variety of approximations to the XC energy functional. The number and sophistication of available density functionals is rapidly increasing. The higher the sophistication, the greater the accuracy but at the expense of more computational resources.

Apart from hybrid functionals, DFT significantly underestimates the band gaps of insulators and semiconductors since it is a ground-state theory and does not take into account many-body effects (Appendix A). Optical measurements suggest an optical band gap of about 0.5 eV for both hexagonal and cubic GST [38, 39]. However, theoretical studies based on DFT suggest smaller band gaps. Using the GGA for the XC energy functional, Lee and Jhi [40] have calculated an indirect band gap of about 0.26 eV along the Γ-K line for the sequence of Kooi and de Hosson [41]. In yet another theoretical study, Tsafack *et al* [8], using the LDA for the XC energy functional, found out that hexagonal GST is semi-metallic whereas the cubic phase has a direct band gap of about 0.2 eV at Γ and an indirect band gap of about 0.1 eV along the Γ-K line. Over the years, *ab initio* theories and frameworks which are able to describe electronic excitations and spectroscopy have become available. These include many-body perturbation theory (MBPT) and time-dependent density functional theory (TDDFT). In this work, the optical absorption spectra of crystalline GST are calculated using TDDFT and the $GW_0$ approximation of MBPT. TDDFT extends the basic ideas of ground-state DFT to the treatment of excitations or, generally, time-dependent phenomena. On the other hand, MBPT is a way to account for electron correlation by treating it as a perturbation to the Hartree-Fock wave function.

### 2.1.2 Time Dependent Density Functional Theory

This brief review of TDDFT is based on Ref. [42]. For simplicity, the Hartree atomic units ($e = \hbar = m = 1$) have been used and the spin degrees of freedom are excluded in the notation.

As with DFT, the basic variable is the electron density, $n(\mathbf{r})$, which is obtained with the help of a fictitious system of non-interacting electrons. The electrons feel an effective time-dependent potential. The exact form of this potential is unknown and has to be approximated. If the time-dependent potential is weak, it is sufficient to resort to linear-response theory to study the system. In this way, it is possible to calculate, for example, the optical absorption spectra. On the other hand, if the time-dependent potential is very strong, a full solution of the Kohn-Sham equations is required. We will be concerned with the former case. The Runge-Gross theorem [43] is the time-dependent extension of the ordinary Hohenberg-Kohn theorems [10]. The Runge-Gross theorem asserts that all observables can be calculated with the knowledge of one-body density, $n(\mathbf{r})$. Nothing is, however, stated on how to calculate $n(\mathbf{r})$. To avoid the cumbersome task of solving the interacting Schrödinger equation, Kohn and Sham utilized the idea of an auxiliary non-interacting Kohn-Sham electrons, subject to an external local potential, $v_{KS}$. This potential is unique, by virtue of the Runge-Gross theorem applied to the non-interacting system and is chosen so that the density of the Kohn-Sham electrons is the same as the density of the original interacting system. In the time-dependent case, these Kohn-Sham electrons obey the time-dependent Schrödinger equation:

$$i\frac{\partial}{\partial t}\psi_i(\mathbf{r},t) = \left[-\frac{\nabla^2}{2} + v_{KS}(\mathbf{r},t)\right]\psi_i(\mathbf{r},t). \tag{2.7}$$

The density of the interacting system can then be obtained from the time-

dependent Kohn-Sham orbitals,

$$n(r,t) = \sum_{i}^{N} |\psi(\mathbf{r},t)|^2 . \tag{2.8}$$

The Kohn-Sham potential is conventionally given by

$$v_{KS}(\mathbf{r},t) = v_{ext}(\mathbf{r},t) + v_H + v_{XC}, \tag{2.9}$$

where $v_{ext}(\mathbf{r},t)$ is the external potential, $v_H(\mathbf{r},t)$ accounts for the classical electrostatic interaction between the electrons:

$$v_H(\mathbf{r},t) = \int \mathrm{d}^3\mathrm{r}' \frac{n(\mathbf{r},t)}{|\mathbf{r}-\mathbf{r}'|}, \tag{2.10}$$

and $v_{XC}$ accounts for all the non-trivial many-body effects and can be written as the functional derivative of the $XC$ part of a new action functional $\tilde{\mathcal{A}}$ [44]:

$$v_{xc}(\mathbf{r},t) = \left.\frac{\delta\tilde{\mathcal{A}}}{\delta n(\mathbf{r},\tau)}\right|_{n(\mathbf{r},t)}, \tag{2.11}$$

where $\tau$ stands for the Keldish pseudo time.

The exact expression for $v_{XC}$ as a functional of the density is not known and approximations are in order. In contrast to stationary-state DFT [10, 11] where very good XC functionals exist, approximations to $v_{XC}$ are still in their infancy. The first and simplest of these is the adiabatic local density approximation (ALDA). More recently, other functionals have been proposed such as the time-dependent exact-exchange (EXX) [45].

As already noted, for a small external time-dependent potential, perturbation theory is sufficient to determine the behavior of the system. The focus is in the linear change of the density that allows for the calculation of the optical absorption spectrum. If the perturbing potential is well-behaved (like almost always in physics) the density can be expanded in a perturbative series:

$$n(\mathbf{r},t) = n^{(0)}(\mathbf{r}) + n^{(1)}(\mathbf{r},t) + n^{(2)}(\mathbf{r},t) + \cdots , \tag{2.12}$$

where $n^{(1)}$ is the component of $n(\mathbf{r},t)$ that depends linearly on the perturbation $v^{(1)}$, $n^{(2)}$ depends quadratically, etc. In frequency space, it reads:

$$n^{(1)}(\mathbf{r},\omega) = \int \mathrm{d}^3\mathrm{r}'\chi(\mathbf{r},\mathbf{r}',\omega)v^{(1)}(\mathbf{r}',\omega), \tag{2.13}$$

where $\chi$ is the linear electron-density response function of the system. The evaluation of $\chi$ through perturbation theory is demanding. However, use can be made of TDDFT to simplify this process.

The linear change in density using the Kohn-Sham system is given by:

$$n^{(1)}(\mathbf{r},\omega) = \int \mathrm{d}^3\mathrm{r}'\chi_{KS}(\mathbf{r},\mathbf{r}',\omega)v^{(1)}_{KS}(\mathbf{r}',\omega), \tag{2.14}$$

where $\chi_{KS}$ is the density response function of a Kohn-Sham system (which is much easier to solve than the fully-interacting $\chi$) and $v^{(1)}_{KS}$ is the linear change in $v_{KS}$. $v^{(1)}_{KS}$ can be calculated explicitly from the definition of the Kohn-Sham potential:

$$v^{(1)}_{KS}(\mathbf{r},t) = v^{(1)}(\mathbf{r},t) + v^{(1)}_H(\mathbf{r},t) + v^{(1)}_{XC}(\mathbf{r},t), \tag{2.15}$$

where $v^{(1)}$ is the variation of the external potential and $v^{(1)}_H$ is the change in the Hartree potential:

$$v^{(1)}_H(\mathbf{r},t) = \int \mathrm{d}^3\mathrm{r}'\frac{n^{(1)}(\mathbf{r}',t)}{|\mathbf{r}-\mathbf{r}'|}. \tag{2.16}$$

Finally, $v^{(1)}_{XC}(\mathbf{r},t)$ is the linear part in $n^{(1)}$ of the functional $v^{(1)}_{XC}[n]$:

$$v^{(1)}_{XC}(\mathbf{r},t) = \int \mathrm{dt}' \int \mathrm{d}^3\mathrm{r}'\frac{\delta v_{XC}(\mathbf{r},t)}{\delta n(\mathbf{r}',t')}n^{(1)}(\mathbf{r}',t'). \tag{2.17}$$

It is useful to introduce the exchange-correlation kernel, $f_{XC}$, defined by:

$$f_{XC}(\mathbf{r}t,\mathbf{r}'t') = \frac{\delta v_{XC}(\mathbf{r},t)}{\delta n(\mathbf{r}',t')}. \tag{2.18}$$

Combining the previous results and transforming to frequency space, it can be

shown that

$$n^{(1)}(\mathbf{r},\omega) = \int \mathrm{d}^3\mathrm{r}'\chi_{KS}(\mathbf{r},\mathbf{r}',\omega)v^{(1)}(\mathbf{r},\omega) + \int \mathrm{d}^3\mathrm{x} \int \mathrm{d}^3\mathrm{r}'\chi_{KS}(\mathbf{r},\mathbf{x},\omega)\left[\frac{1}{|\mathbf{x}-\mathbf{r}'|} + f_{XC}(\mathbf{x},\mathbf{r}',\omega)\right] n^{(1)}(\mathbf{r}',\omega). \tag{2.19}$$

From eqns. (2.13) and (2.19) trivially follows the relation:

$$\chi(\mathbf{r},\mathbf{r}',\omega) = \chi_{KS}(\mathbf{r},\mathbf{r}',\omega) + \int \mathrm{d}^3\mathrm{x} \int \mathrm{d}^3\mathrm{x}'\chi(\mathbf{r},\mathbf{x},\omega)\left[\frac{1}{|\mathbf{x}-\mathbf{x}'|} + f_{XC}(\mathbf{x},\mathbf{x}',\omega)\right] \chi_{KS}(\mathbf{x}',\mathbf{r}',\omega). \tag{2.20}$$

This equation is a formally exact representation of the linear density response.

Current implementations of TDDFT fall into three broad categories. In the first, the TDDFT charge susceptibility is obtained from the independent-electron susceptibility using a Dyson-like linear equation [46, 47]; in the second, the poles of the susceptibility, corresponding to excitation energies, are addressed as the eigenvalues of a suitable linear operator equation [47, 48]; finally, the full spectrum of a system can be transformed by Fourier analyzing all the time series generated by the expectation of some observable (such as the dipole) calculated along the perturbed time-evolution of the TDDFT molecular orbitals [49, 50].

A new approach to linearized TDDFT has been recently introduced allowing one to simulate molecular systems made of up to several hundred atoms. This is the Liouville-Lanczos approach, originally proposed by Walker *et al* [51] and implemented in the turboTDDFT package [52] of the QUANTUM ESPRESSO distribution [9]. This approach has been used in this study to calculate the optical absorption spectra of hexagonal and cubic GST.

### 2.1.3 Many Body Perturbation Theory

This brief review of many-body perturbation theory is based on Refs. [53, 54].

Band gaps are experimentally measured by photoelectron spectroscopy. In direct photoelectron spectroscopy, a photon impinges on a sample and ejects an electron whose energy is measured. In inverse photoelectron spectroscopy, an electron is injected into a sample and the energy of the emitted photon is measured. The fact that the independent-electron picture breaks down due to the strong Coulomb interaction puts in doubt single-electron concepts such as band structure or Fermi surface. However, the nearly-independent picture can be retained if quasi-particles, instead of electrons or holes, are considered. The addition (removal) of an electron in indirect (direct) photoelectron spectroscopy creates (annihilates) an ensemble consisting of the bare electron and its oppositely charged Coulomb hole. This ensemble behaves in many ways as a single particle and is called a *quasi-particle*. The Coulomb hole reduces the total charge of the quasi-particle and the effective interaction between quasi-particles is screened and considerably weaker than the bare Coulomb interaction between electrons. The screened interaction is sufficiently small so that the quasi-particle can be regarded as approximately independent. Many-body perturbation theory is the theoretical framework that links the $N$-particle and the $N \pm 1$-particle systems and the central variable is the time-ordered Green function, $G(\mathbf{r}'t', \mathbf{r}'t')$.

The Green function $G^e(\mathbf{r}t, \mathbf{r}'t')$ is defined such that $i\hbar G^e(\mathbf{r}t, \mathbf{r}'t')$ is the probability amplitude for the propagation of an additional electron from $(\mathbf{r}'t')$ to $(\mathbf{r}t)$ in a many-electron system. Similarly, $G^h(\mathbf{r}'t', \mathbf{r}t)$ is defined as the Green function for the propagation of an additional hole from $(\mathbf{r}t)$ to $(\mathbf{r}'t')$. For con-

venience, the two can be combined in one time-ordered Green function

$$\begin{aligned} G(\mathbf{r}t, \mathbf{r}'t') &= G^e(\mathbf{r}t, \mathbf{r}'t') - G^h(\mathbf{r}'t', \mathbf{r}t) \\ &= -\frac{i}{\hbar} \left\langle \Psi_0^N \left| \hat{T} \left[ \hat{\psi}(\mathbf{r}t) \hat{\psi}^\dagger(\mathbf{r}'t') \right] \right| \Psi_0^N \right\rangle, \end{aligned} \tag{2.21}$$

where $\hat{T}$ is the time ordering operator and $\hat{\psi}^\dagger$ and $\hat{\psi}$ are the creation and annihilation operators, respectively. Consider the time-ordered Green function $G(\mathbf{r}, \mathbf{r}'; \tau)$ of a stationary system with $\tau = t - t'$. It can be shown that

$$\begin{aligned} G(\mathbf{r}, \mathbf{r}'; \tau) = &- \frac{i}{\hbar} \sum_i \psi_i^{N+1}(\mathbf{r}) \psi_i^{N+1^*}(\mathbf{r}') e^{-i\epsilon_i^{N+1}\tau/\hbar} \theta(\tau) \\ &+ \frac{i}{\hbar} \sum_i \psi_i^{N-1}(\mathbf{r}) \psi_i^{N-1^*}(\mathbf{r}') e^{-i\epsilon_i^{N-1}\tau/\hbar} \theta(-\tau), \end{aligned} \tag{2.22}$$

where the sums run over the ground state and all the excited states of the $N-1$-particle and $N+1$-particle systems and $\theta(\tau)$ is the Heaviside step function defined by

$$\theta(\tau) = \begin{cases} 1, & \text{if } \tau > 0. \\ 0, & \text{if } \tau < 0. \end{cases} \tag{2.23}$$

The Green function contains the complete excitation spectrum of the $N \pm 1$-particle system. Fourier transformation of eqn. (2.22) to the frequency axis, using the Fourier transform of the Heaviside step function, finally yields the *Lehmann* representation of the Green function

$$G(\mathbf{r}', \mathbf{r}; \omega) = \sum_i \frac{\psi_i^{N+1}(\mathbf{r}) \psi_i^{N+1^*}(\mathbf{r})}{\hbar\omega - \epsilon_i^{N+1} + i\eta} + \sum_i \frac{\psi_i^{N+1}(\mathbf{r}) \psi_i^{N-1^*}(\mathbf{r})}{\hbar\omega - \epsilon_i^{N-1} - i\eta}, \tag{2.24}$$

where $\eta$ is an infinitesimal positive number and $\epsilon_i^{N\pm1}$ are the true many-particle excitation energies corresponding to the excitations of an $N+1$-particle and $N-1$-particle systems and hence to those processes measured in inverse and direct photoelectron spectroscopy.

In connection with eqn.(2.22) can be defined the spectral function, $A(\mathbf{r}, \mathbf{r}'; \omega)$,

that is, the density of the excited (or quasiparticle) states that contribute to the electron or hole propagation:

$$A(\mathbf{r},\mathbf{r}';\omega) = \sum_i \psi_i(\mathbf{r})\psi_i^*(\mathbf{r}')\delta(\hbar\omega - \epsilon_i). \tag{2.25}$$

Eqn. (2.24) can then be re-written as an integral over frequencies:

$$G(\mathbf{r},\mathbf{r}';\omega) = \hbar\int_{-\infty}^{\infty} \frac{A(\mathbf{r},\mathbf{r}';\omega)}{\hbar\omega - \hbar\omega' + sgn(\hbar\omega' - \mu)i\eta}\mathrm{d}\omega. \tag{2.26}$$

It can be shown that the time-ordered Green function, $G(\mathbf{r},\mathbf{r}';\omega)$, of the interacting system obeys an integral equation, the *Dyson* equation:

$$\begin{aligned} G(\mathbf{r},\mathbf{r}';\omega) =& G_0(\mathbf{r},\mathbf{r}';\omega) \\ &+ \int\int G_0(\mathbf{r},\mathbf{r}'';\omega)\sum(\mathbf{r}'',\mathbf{r}''';\omega)G(\mathbf{r}''',\mathbf{r}';\omega)\mathrm{d}^3\mathrm{r}''\mathrm{d}^3\mathrm{r}''', \end{aligned} \tag{2.27}$$

where $G_0(\mathbf{r},\mathbf{r}';\omega)$ is the Green function of a mean-field system defined by

$$\hat{h}_0(\mathbf{r})\varphi_i^0(\mathbf{r}) = \epsilon_i^0\varphi_i^0(\mathbf{r}), \tag{2.28}$$

with the single-particle hamiltonian

$$\hat{h}_0 = -\frac{\hbar^2}{2m}\nabla^2 + V_{ext}(\mathbf{r}) + \frac{e}{4\pi\varepsilon_0}\int\frac{n(\mathbf{r})}{|\mathbf{r}-\mathbf{r}'|}\mathrm{d}^3\mathrm{r}'. \tag{2.29}$$

The Green function, $G_0(\mathbf{r},\mathbf{r}';\omega)$, is obtained from eqn. (2.24) with the wave functions $\varphi_i^0$ and energies $\epsilon_i^0$. The non-local and frequency-dependent function, $\Sigma(\mathbf{r},\mathbf{r}';\omega)$, is the non-Hermitian self-energy operator, which contains all many-body XC effects beyond the electrostatic Hartree potential. By inserting the Lehmann representation (eqn. (2.24)) into eqn. (2.27), it can be shown that the wave functions $\psi_i$ and energies $\epsilon_i$ obey the quasi-particle equation

$$\hat{h}_0(\mathbf{r})\psi_i(\mathbf{r}) + \int\Sigma(\mathbf{r},\mathbf{r}';\epsilon_i/\hbar)\psi_i(\mathbf{r}')\mathrm{d}^3\mathrm{r}' = \epsilon_i\psi_i(\mathbf{r}), \tag{2.30}$$

which is non-linear in $\epsilon_i$. Although very similar to one-particle equations of mean-field approaches like Hartree, Hartree-Fock and DFT, it does not con-

stitute a mean-field formulation, since the self-energy takes all dynamic many-electron processes into account. The Dyson equation (2.27) can be rewritten in the form of a geometric series by subsequently replacing $G$ on the right-hand side by $G_0 + G_0\Sigma G$, which leads to

$$G = G_0 + G_0\Sigma G_0 + G_0\Sigma G_0\Sigma G_0 + G_0\Sigma G_0\Sigma G_0 + \dots \quad . \tag{2.31}$$

This is a typical equation of scattering theory, where the different terms of the geometric series describe single, double, triple, etc., scattering processes and $\sum$ is the scattering potential. Such a succession of scattering processes can be illustrated by Feynman diagrams. It is more natural to describe the Coulomb interaction ($v$) in terms of the screened Coulomb potential ($W$) and then write down the self-energy ($\sum$) as a perturbation series in terms of $W$. Keeping just the first term of such an expansion gives the GW approximation. The self-energy can be obtained from a self-consistent set of Dyson-like equations known as *Hedin's* equations:

$$P(1\ 2) = -i \int \mathrm{d}(3\ 4) G(1\ 3) G(4\ 1^+) \Gamma(3\ 4, 2), \tag{2.32a}$$

$$W(1\ 2) = W(1\ 2) + \int \mathrm{d}(3\ 4) W(1\ 3) P(3\ 4) W(4\ 2), \tag{2.32b}$$

$$\Sigma(1\ 2) = i \int \mathrm{d}(3\ 4) G(1\ 4^+) W(1\ 3) \Gamma(4\ 2, 3), \tag{2.32c}$$

$$\begin{aligned} G(1\ 2) =& G_{KS}(1\ 2) \\ &+ \int \mathrm{d}(3\ 4) G_{KS}(1\ 3) \left[ \sum (3\ 4) - \delta(3\ 4) V_{XC}(4) G(4\ 2) \right], \end{aligned} \tag{2.32d}$$

$$\begin{aligned} \Gamma(1\ 2, 3) =& \delta(1\ 2)\delta(1\ 3) \\ &+ \int \mathrm{d}(4\ 5\ 6\ 7) \frac{\delta\Sigma(1\ 2)}{\delta G(4\ 5)} G(4\ 6) G(7\ 5) \Gamma(6\ 7, 3), \end{aligned} \tag{2.32e}$$

where the space-time coordinates $(\mathbf{r}_1, t_1)$ are denoted by the natural number 1

etc. $P$ is the irreducible polarization, $\Gamma$ is the so-called vertex function and

$$G_{KS}(\mathbf{r},\mathbf{r}';\omega)\Sigma_i \frac{\varphi_i^{KS}(\mathbf{r})\varphi_i^{KS^*}(\mathbf{r}')}{\omega-\epsilon_i^{KS}-sgn(\mu-\epsilon_i^{KS})i\eta}, \tag{2.33}$$

with $G_{KS}$ being the Green function of the Kohn-Sham (KS) system and $\varphi_i^{KS}$ the corresponding KS wave functions with eigenenergies $\epsilon_i^{KS}$. The GW approximation is arrived at by eliminating the 2nd term in the vertex function (eqn. (2.32e)) in such a way that eqns. (2.32a) and (2.32b) reduce to

$$P(1\ 2) = -iG(1\ 2)G(2\ 1^+), \tag{2.34a}$$

$$\Sigma(1\ 2) = iG(1\ 2^+)W(1\ 2). \tag{2.34b}$$

That is, in GW the screened Coulomb potential is calculated at the random phase approximation (RPA) level and $\sum$ is just the direct product of $G$ and $W$ (and hence the name). In most GW applications, self-consistency is set aside, and $P$ and $\Sigma$ are obtained by setting $G = G_{KS}$ in eqns. (2.34a) and (2.34b). The interacting Green function is then obtained by solving eqn. (2.32d) once. Furthermore, in many cases there is almost a complete overlap of the quasi-particle (QP) and Kohn-Sham (KS) wave functions. Consequently, the full resolution of the quasi-particle eqn. (2.30) may be circumvented. Hence, $E_i^{QP}$ is given as a first order perturbation of the KS energy, $\epsilon_i^{KS}$:

$$E_i^{QP} \simeq \epsilon_i^{KS} + \left\langle \varphi_i^{KS} \left| \Sigma(\epsilon_i^{KS}) - V_{XC} - \Delta\mu \right| \varphi_i^{KS} \right\rangle, \tag{2.35}$$

where $\Delta\mu$ has been added to align the chemical potential before and after the inclusion of the GW correction. The procedure has been summarized in Fig. 2.2. Non-self-consistent GW (i.e. $G_0W_0$) has been applied to calculate QP properties (band structures and life times) for a variety of systems. The $G_0W_0$ approximation is able to fairly reproduce the experimental band gaps of many semiconductors and insulators and so circumventing the well-known failure of LDA when calculating excitation gaps. However, $G_0W_0$ has some

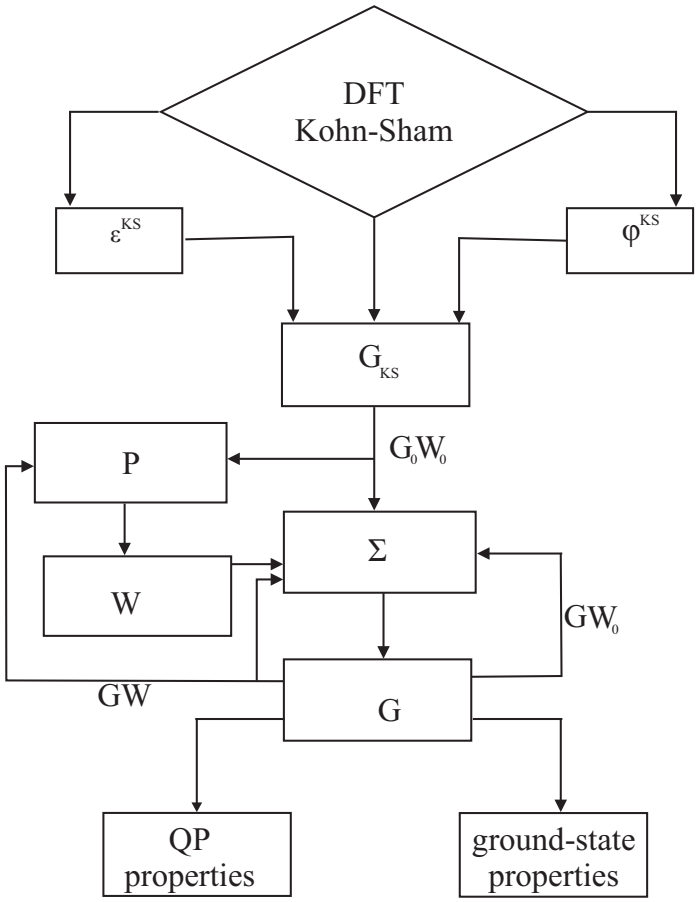


Figure 2.2: Flow diagram showing the practical implementation of the *GW* method.

limitations. In this study, the partially self-consistent $GW_0$ method has been used to compute the absorption spectra of hexagonal and cubic GST. Although the fully self-consistent *GW* method is designed for analysis of excited states of the $(N \pm 1)$-electron systems, the treatment of optical absorption processes where the particle number does not change due to the promotion of valence electrons into unoccupied conduction states rather than emission requires the simultaneous description of two particles: an electron and a hole (i.e. an exciton). This requires a two-particle Green function. In this case many-body perturbation theory leads to the Bethe-Salpeter equation (BSE). Another alternative is the time-dependent perturbation theory, which also gives access to the excited states of an $N$-electron system.

## 2.2 Thermal Properties

In the theory of lattice dynamics, the harmonic approximation (HA) can be used to calculate the phonon dispersion spectra within the framework of density functional perturbation theory (DFPT). However, in the HA the vibrations in the crystal are independent of the interatomic distance, that is, the vibrational energy does not depend on volume and so the equilibrium lattice parameter does not depend on temperature. A proper way to take anharmonic effects into account is to calculate all unharmonic terms, but this is not a reasonable task. A simple way to take anharmonic effects into account is through the Quasiharmonic Approximation (QHA). QHA is a phonon-based model used to treat frequencies as volume dependent so as to account for thermal effects.

The low-temperature heat capacity of solids is experimentally found to vanish as the cube of the temperature, with a cubic coefficient that is system specific [55, 56]. This is contrary to the predictions of classical statistical mechanics according to which the heat capacity of a system of harmonic oscillators is neither dependent on the temperature nor its spectrum. One of the landmarks of modern solid-state physics that greatly contributed to the establishment of our present quantum mechanical picture of matter is the Debye model for the heat capacity of solids [55]. This model naturally explains the low-temperature specific heat of solids in terms of the (quantum) statistical mechanics of an ensemble of harmonic oscillators, which can in turn be periodically described as a gas of non-interacting quasi-particles obeying the Bose-Einstein statistics (i.e. phonons).

The internal energy of a single harmonic oscillator of angular frequency, $\omega$, in thermal equilibrium at temperature, $T$, is

$$< E >= \frac{\hbar\omega}{2} + \frac{\hbar\omega}{e^{\frac{\hbar\omega}{k_B T}} - 1}, \tag{2.36}$$

where $k_B$ is the Boltzmann constant. By differentiating with respect to tem-

perature the sum over all the possible values of the phonon momentum in the Brillouin zone (BZ) of eqn. (2.36), it can be shown that the isochroic specific heat of a crystal is

$$C_V(T) = \frac{1}{V}\sum_{\mathbf{q},\nu} \hbar\omega(\mathbf{q},\nu) n'(\mathbf{q},\nu), \tag{2.37}$$

where $\omega(\mathbf{q},\nu)$ is the frequency of the $\nu$-th mode (phonon) at point $\mathbf{q}$ in the BZ,

$$n'(\mathbf{q},\nu) = \frac{\partial}{\partial T}[e^{(\frac{\hbar\omega(\mathbf{q},\nu)}{k_B T})} - 1]^{-1}, \tag{2.38}$$

and the sum is extended in the first BZ. By assuming that there are three degenerate modes at each point of the BZ, each one with frequency, $\omega(\mathbf{q},\nu) = c|\mathbf{q}|$, $c$ being the velocity of sound, and converting the sum in eqn. (2.37) into an integral, the resulting expression for the heat capacity, valid in the low-temperature limit, is

$$C_V = \frac{1}{\Omega}\frac{12\pi^4}{5} k_B \left(\frac{T}{\Theta_D}\right)^3, \tag{2.39}$$

where $\Omega$ is the volume of the unit cell and $\Theta_D$, given by

$$\Theta_D = \left(\frac{2\pi\hbar}{k_B}\right) c \left(\frac{3}{4\pi\Omega}\right)^{\frac{1}{3}}, \tag{2.40}$$

is the so-called Debye temperature. In the Born-Oppenheimer approximation [57], the vibrational properties of molecules and solids are determined by their electronic structure through the dependence of the ground-state energy on the co-ordinates of the atomic nuclei [58]. At low temperatures, the amplitudes of atomic vibrations are much smaller than interatomic distances, and one can assume that the dependence of the ground-state energy on the deviation from equilibrium of the atomic positions is quadratic. In this so called *harmonic approximation* (HA), energy differences can be calculated from electronic structure theory using static response functions [59, 60] or perturbation theory [61].

As already noted, in the HA vibrational frequencies do not depend on interatomic distances, so that the vibrational contribution to the crystal internal energy does not depend on volume. As a consequence, constant-pressure and constant-volume specific heats coincide in this approximation, and the equilibrium volume of a crystal does not depend on temperature. Other shortcomings of the HA include its prediction of an infinite thermal conductivity, infinite phonon lifetimes, and the independence of the vibrational spectra (as well as the related properties: elastic properties, sound velocities e.t.c.) on temperature, to name but a few. A proper account of anharmonic effects on the static and dynamical properties of materials would require the calculation of phonon-phonon interaction coefficients for all modes in the BZ zone. Although the leading terms of such interactions can be computed even from first principles [62, 63] - and the resulting vibrational line widths have in fact been evaluated in some cases [63–65] - the extensive sampling of the phonon-phonon interactions over the BZ required for free-energy evaluations remains a daunting task. The simplest generalization of the HA, which corrects for most of the above-mentioned deficiencies, while not requiring any explicit calculation of the anharmonic interaction coefficients, is the QHA.

In the QHA, the crystal free energy is assumed to be determined by the vibrational spectrum via the standard harmonic expression:

$$F(X,T) = U_0(X) + \frac{1}{2}\sum_{\mathbf{q},\nu} \hbar\omega(\mathbf{q},\nu|X) + k_B T \sum_{\mathbf{q},\nu} log\Big(1 - e^{\frac{(\hbar\omega(\mathbf{q},\nu)|X)}{k_B T}}\Big), \tag{2.41}$$

where $X$ indicates any global static constraint upon which vibrational frequencies may depend (most commonly just the volume $V$, but $X$ may also include anisotropic components of the strain tensor, some externally applied fields, the internal distortions of the crystal unit cell or other thermodynamic constraints that may be applied to the system), and $U_0(X)$ is the zero-temperature energy

of the crystal as a function of $X$. In the case where $X = V$, differentiation of eqn. (2.41) with respect to the volume gives the equation of state:

$$\begin{aligned} P &= -\frac{\partial F}{\partial V} \\ &= -\frac{\partial U_o}{\partial V} + \frac{1}{V}\sum_{\mathbf{q},\nu} \hbar\omega(\mathbf{q},\nu)\gamma(\mathbf{q},\nu)\left(\frac{1}{2} + \frac{1}{e^{\frac{\hbar\omega(\mathbf{q},\nu)}{k_B T}} - 1}\right), \end{aligned} \tag{2.42}$$

where

$$\gamma(\mathbf{q},\nu) = -\frac{V}{\omega(\mathbf{q},\nu)}\frac{\partial\omega(\mathbf{q},\nu)}{\partial V} \tag{2.43}$$

are the so-called Grüneisen mode parameters. In a perfectly harmonic crystal, phonon frequencies do not depend on the interatomic distances as mentioned earlier and, hence, do not depend on volume too. In such a harmonic crystal, (2.42) implies that the temperature derivative of pressure at fixed volume vanish, that is, $(\partial P/\partial T)_V = 0$. It follows that the thermal expansivity, $\beta = V^{-1}(\partial V/\partial T)_P$, which is given by the thermodynamic relation:

$$\begin{aligned} \beta &= -\frac{(\partial P/\partial T)_V}{(\partial P/\partial V)_T} \\ &= \frac{1}{B_T}\left(\frac{\partial P}{\partial T}\right)_V \\ &= \frac{1}{B_T}\sum_{\mathbf{q},\nu} \hbar\omega(\mathbf{q},\nu)\gamma(\mathbf{q},\nu)n'(\mathbf{q},\nu), \end{aligned} \tag{2.44}$$

where $B_T = V(\partial P/\partial V)_T$ is the crystal bulk modulus, would also vanish for perfectly harmonic crystals. Inspired by eqn. (2.37), let us define

$$C_V(\mathbf{q},\nu) = \frac{\hbar\omega(\mathbf{q},\nu)n'(\hbar\omega)}{V}, \tag{2.45}$$

as the contribution of the $\nu$-th normal mode at the $\mathbf{q}$-point of the BZ to the total specific heat and

$$\hat{\gamma} = \frac{\sum_{\mathbf{q},\nu}\gamma(\mathbf{q},\nu)C_V(\mathbf{q},\nu)}{\sum_{\mathbf{q},\nu}C_V(\mathbf{q},\nu)}, \tag{2.46}$$

as the weighted average of the various Grüneisen parameters. In terms of $\gamma$,

the thermal expansivity simply reads:

$$\beta = \frac{\hat{\gamma} C_V}{B_T}. \tag{2.47}$$

The vanishing of the thermal expansivity in the HA would also imply the equality of the constant-pressure and the constant-volume specific heats. By imposing the constraint that the total differentials of the entropy as a function of pressure and temperature or of volume and temperature coincide, and by using the Maxwell identities, one can show that [56]:

$$\begin{aligned} C_P - C_V &= -\frac{T}{V}\left(\frac{\partial P}{\partial V}\right)_T \left(\frac{\partial V}{\partial T}\right)_P \\ &= T B_T \beta^2. \end{aligned} \tag{2.48}$$

We conclude by noting that the ansatz given by eqn. (2.41) for the crystal free energy in terms of its vibrational frequencies, which are volume-dependent, gives immediate access to all the equilibrium thermal properties of the system. Whether this implicit account of anharmonic effects through the volume dependence of the vibrational frequency only is sufficient to describe the relevant thermal effects, or an explicit account of the various phonon-phonon interactions is in order (calculating each anharmonic term), is a question that can only be addressed by extensive computational experience and comparison to experiment.

In one theoretical study [8], the specific heat capacity for hexagonal GST as a function of temperature has been calculated by integrating the vibrational density of states. In this work, we calculate the heat capacity of cubic GST as well using the QHA. Moreover, we calculate the entropy of hexagonal GST as a function of temperature.

## 2.3 Effect of Nitrogen Doping on Hexagonal and Cubic $Ge_2Sb_2Te_5$

For electronic phase-change memory to be viable, the writing current has to be reduced so as to minimize energy consumption and dissipation. One of the proposals put forward to address this issue is to dope GST with a small amount of impurity atoms such as N, O, Sn, Si, In and Ag [66–74]. Among these, N seems to be the most promising method to improve the physical properties by increasing the resistivity of the crystalline film [66].

Another driving force for research in new phase-change materials is to decrease the wavelength of the laser used for writing, reading and erasing bits. By decreasing the wavelength, the size of the written bits also decreases and hence the storage density increases [75]. Pure GST possesses a high optical contrast in the red and infrared spectral range. Decreasing the wavelength beyond visible blue light is very challenging since light-emitting diodes are not available for this spectral range. Hence, this requires a different approach. This study explores the possibility of incorporating N atoms into GST to optimize the reflectivity contrast in the blue and ultraviolet regions of the electromagnetic spectrum. At the time of writing, no theoretical study had investigated this concept.

# Chapter 3
# Methodology

In this study, the electronic structure calculations were performed within the framework of density functional theory as implemented in the QUANTUM ESPRESSO distribution [9]. Plane wave basis sets were used for the expansion of atomic orbitals. The electron-ion interactions were described using pseudopotentials.

## 3.1 Choice of Pseudopotentials

In describing ion-electron interactions, this study makes use of two sets of pseudopotentials. The first set consists of the norm-conserving pseudopotentials *Te.pz-bhs.UPF*, *Sb.pz-bhs.UPF* and *Ge.pz-bhs.UPF* [76], generated according to the Bachelet-Hamann-Schluter (BHS) scheme without non-linear corrections, the exchange-correlation energy functional being in the Local Density Approximation (LDA) of Perdew and Zunger (PZ) [14]. In this case, only the valence electrons were considered. The valence configurations are $Ge\ 4s^2 4p^2$, $Sb\ 5s^2 5p^3$ and $Te\ 5s^2 5p^4$.

The second set consists of the norm-conserving pseudopotentials *Te.pbe-hgh.UPF*, *Sb.pbe-hgh.UPF* and *Ge.pbe-hgh.UPF* [77, 78] with the exchange and correlation energy in the general gradient approximation (GGA) of Perdew, Burke and Ernzerhof (PBE) [17]. In this case, the $Ge\ 3d$, $Sb\ 4d$ and $Te\ 4d$ semicore electrons were considered alongside the $Ge\ 4s^2 4p^2$, $Sb\ 5s^2 5p^3$, and $Te\ 15s^2 5p^4$ valence electrons. Lee and Jhi [40] and Do *et al* [79] have shown that including the $Te\ 4d$ electrons in the valence configuration has an effect on the value of the calculated lattice constants. If more core states are considered, the accuracy of the calculations is improved, although at a higher computational cost. Van Lenthe *et al* [80] have noted the effect of spin-orbit coupling on

bond distances and, hence, lattice parameters, on such heavy atoms as $Ge$, $Sb$ and $Te$. An accurate description of spin-orbit coupling requires a relativistic treatment. The pseudopotentials used in this study do not take into account relativistic effects. This is due to the limitations of the pseudopotential library at the time of this study.

## 3.2 Convergence Criteria

The size of the basis set is determined by the kinetic cut-off energy. The electronic states in a crystal are given by the Bloch waves,

$$\psi_{\mathbf{k}}(\mathbf{r}) = \sum_{\mathbf{G}} c_{\mathbf{k},\mathbf{G}}\ exp[i(\mathbf{k}+\mathbf{G})\cdot\mathbf{r}], \tag{3.1}$$

where $\mathbf{G}$ is the reciprocal lattice vector, each state having kinetic energy,

$$E = \frac{\hbar^2}{2m}|\mathbf{k}+\mathbf{G}|^2. \tag{3.2}$$

It is usual to truncate the infinite sum in eqn. (3.1) such that

$$\frac{\hbar^2}{2m}|\mathbf{k}+\mathbf{G}|^2 < E_{cut}, \tag{3.3}$$

where $E_{cut}$ is the kinetic energy cutoff. Hence, the infinite sum reduces to

$$\psi_{\mathbf{k}}(\mathbf{r}) = \sum_{|\mathbf{k}+\mathbf{G}|<\mathbf{G}_{cut}} c_{\mathbf{k},\mathbf{G}}\ exp[i(\mathbf{k}+\mathbf{G})\cdot\mathbf{r}]. \tag{3.4}$$

In this study, the kinetic energy cutoff was set to 50 Ry for both hexagonal and cubic GST.

DFT calculations involve the evaluation of integrals of the form:

$$\frac{\Omega}{(2\pi)^3}\int_{IBZ} H(\mathbf{k})d\mathbf{k} = \frac{1}{\Omega'}\int_{IBZ} H(\mathbf{k})d\mathbf{k}, \tag{3.5}$$

where $\Omega$ and $\Omega'$ are the unit cell volumes in real and reciprocal space, respectively and $IBZ$ denotes the irreducible Brillouin zone. In this study, the

Brillouin zone (BZ) integration was performed using an un-unshifted $k$-point grid of $8 \times 8 \times 2$, generated according to the Monkhorst-Pack scheme [81]. Monkhorst-Pack grids are now the most widely used because they lead to a uniform set of points determined by a simple formula valid for any crystal:

$$\mathbf{k}_{n_1,n_2,n_3} \equiv \sum_{i}^{3} \frac{2n_i - N - 1}{2N} \mathbf{G}_i, \tag{3.6}$$

where $\mathbf{G}$ are the primitive vectors of the reciprocal lattice and $n_i = 1, 2, \ldots, N$. For metals and materials with small band gaps (about 0.5 eV for hexagonal and cubic GST), the $k$-grid has a discontinuity at the Fermi surface. This complication causes slow convergence in the total energy. Smearing methods are used to circumvent this difficulty. In this study, gaussian smearing was used.

## 3.3 Bulk Crystal Structures for Input

GST has two crystalline phases, a metastable cubic phase (which undergoes the reversible crystalline-to-amorphous transition) and a stable hexagonal phase. Hexagonal GST has $P\overline{3}m1$ symmetry and nine atoms per unit cell in nine layers stacked along the $c$ axis. Three possible sequences have been proposed. Kooi and de Hosson [41] proposed the sequence $Te-Ge-Te-Sb-Te-Te-Sb-Te-Ge$, which is hereafter referred to as phase A (Fig. 3.1). Petrov *et al* [82] have proposed the sequence in which the positions of $Ge$ and $Sb$ atoms have been reversed. This sequence is hereafter referred to as phase B (Fig. 3.2). Most recent diffraction experiments [83] suggest a random placement of $Ge$ and $Sb$ layers. This configuration is hereafter referred to as phase C (Fig. 3.3) . In this study, total energy calculations were performed for each sequence, thereafter the sequence having the lowest total energy at equilibrium volume was considered. The ball and stick models in Figs. 3.1-3.5 were generated using the crystal/molecular structure visualizing package, `XCrysDen` [84, 85].

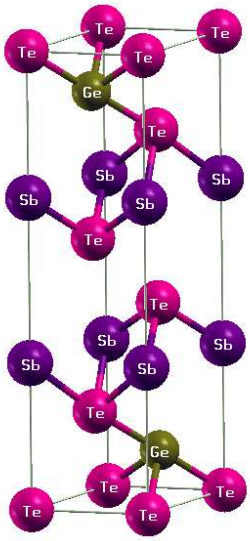


Figure 3.1: A ball and stick model of phase A of hexagonal GST.

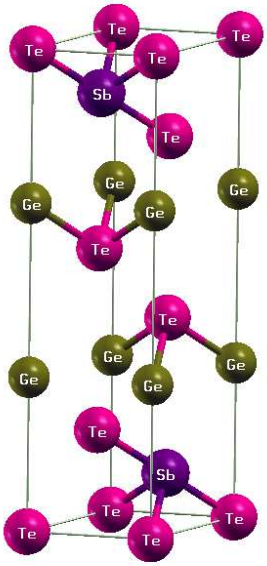


Figure 3.2: A ball and stick model of phase B of hexagonal GST.

Cubic GST has a rock salt structure in which $Te$ atoms occupy the anion (4$a$-type) sites whereas $Ge$, $Sb$ and intrinsic vacancies (v) occupy randomly the cation (4$b$-type) sites [7, 86–89]. Any rock salt structure can be viewed as a

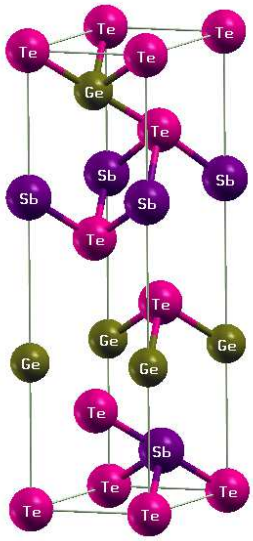


Figure 3.3: A ball and stick model of phase C of hexagonal GST.

close packing of hexagonal planes along any of its diagonals ( [111] direction). For purposes of implementation, this study has replaced cubic GST with an equivalent hexagonal lattice, which is the result of taking the atomic stacking along the [111] direction in the rock salt structure. Hence, the unit cell has 27 atoms and three vacancies arranged in the stacking sequence $Te-Ge-Te-Sb-Te$–v–$Te-Sb-Te-Ge$ repeated three times along the c-axis [8]. Fig. 3.4 shows only one-third of the unit cell.

## 3.4 Nitrogen Doping

The atomic radii of $Ge$, $Sb$ and $Te$ atoms are approximately twice that of $N$ atom [90]. Hence, $N$ cannot substitute $Ge$, $Sb$ or $Te$ under normal circumstances. $N$ can only occupy interstitial sites. The relative concentration of $N$ in hexagonal and cubic GST was set to 10 and 25 at. %, where relative concentration has been defined as the ratio of the number of $N$ atoms to the total number of atoms in the unit cell. The position of $N$ atoms in hexagonal

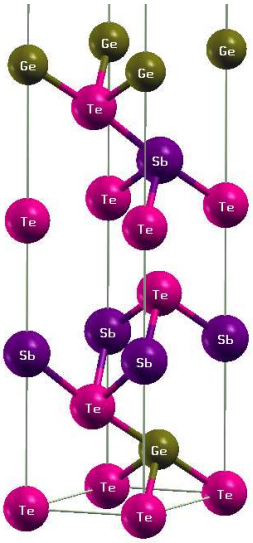


Figure 3.4: A ball and stick model of cubic GST.

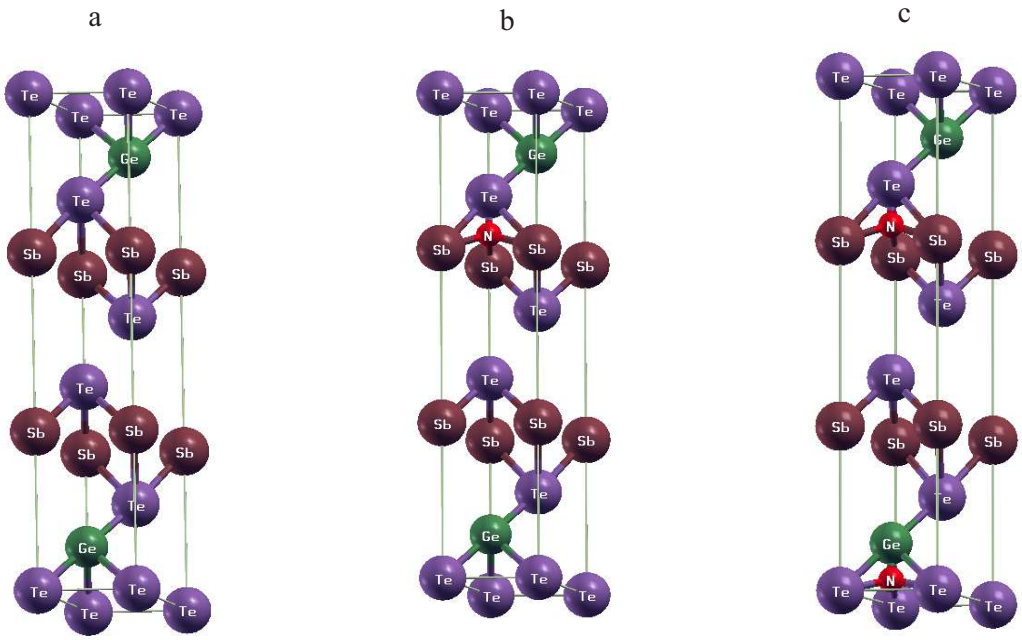


Figure 3.5: A ball and stick model of pure (a) and doped (b and c) hexagonal GST.

GST is shown in Fig. 3.5.

## 3.5 Structural Optimization

### 3.5.1 Optimization of Lattice Parameters

In order to obtain equilibrium lattice parameters, calculations of the total energy were carried out for a number of unit cell volumes. The resulting energy versus volume data were then fitted to the Murnaghan equation of state (EOS) [91]:

$$E(V) = E_0 + \frac{B_0 V}{B_0'}\left(\frac{(V_0/V)^{B_0'}}{B_0' - 1} + 1\right) - \frac{B_0 V_0}{B_0' - 1}, \tag{3.7}$$

where $V$ is the volume of the unit cell, $B_0$ and $B_0'$ are the bulk modulus and its pressure derivative at equilibrium volume, respectively. The Murnaghan EOS is well-known and extensively used.

### 3.5.2 Optimization of Atomic Coordinates

The total energy in not only a function of lattice constants but also a function atomic positions. For simple crystals, the equilibrium atomic positions are known and fixed. However, in more complex crystals, for instance $Ge_2Sb_2Te_5$, the equilibrium atomic positions are not known and have to be calculated. This is done by performing what is known as variable-cell relaxation. In the relaxed structure, the forces acting on the atoms is almost zero. In this study, the structures were relaxed at the optimized cell parameters.

## 3.6 Calculation of the Formation Energy

The formation energy, $E_f$, was calculated using the relation:

$$E_f = \frac{\{E_{total} - E_{clean} - (E_N \times M)\}}{n}, \tag{3.8}$$

where $E_{total}$ is the total energy of nitrogen-doped GST (NGST), $E_{clean}$ is the total energy of pure GST, $E_N$ is the total energy of nitrogen, $M$ is the number

of nitrogen atoms and $n$ is the total number of atoms in the unit cell. In this scheme, $E_f = 0$ for pure GST.

## 3.7 Calculation of Thermal Properties

Phonon dispersion spectra and the associated density of states (DOS) have been calculated within the framework of density functional perturbation theory (DFPT) [61] as implemented in the code `Phonon` within Quantum ESPRESSO [9]. The calculation involves three major steps:

1. The usual ground state SCF calculation for the unperturbed system.

2. Calculation of dynamical matrices on a grid of **q**-vectors which was done on a $4 \times 4 \times 4$ grid of **q**-vectors for both hexagonal and cubic GST. The convergence threshold was set to $10^{-14}$ Ry for hexagonal GST and $10^{-12}$ Ry for cubic GST. The convergence threshold for cubic GST was set lower so as to reduce the computation time. With 60 processors, it took slightly more than a month to calculate the dynamical matrices for the cubic phase whereas for the hexagonal phase, it took about two weeks.

3. The transformation of the dynamical matrices from **G**-space (reciprocal space) to **R**-space (real space).

Thermal properties were then calculated within the framework of the Quasi-Harmonic Approximation (QHA) [92] in which the input includes basic information about the system (such as atomic masses and lattice type) and a file containing the dynamical matrices stored in an appropriate format. In this study, the internal energy, vibrational energy, heat capacity and entropy have been calculated over the temperature range 5-1000 K.

## 3.8 Calculation of Electronic Properties

The electronic DOS is one of the primary quantities used to describe the electronic state of a material. It describes the number of states at each energy level that are available to be occupied by electrons. An expression for the number of available states in a solid can be obtained by considering the electrons in a solid as a free electron gas. If we choose to represent the electron state as a

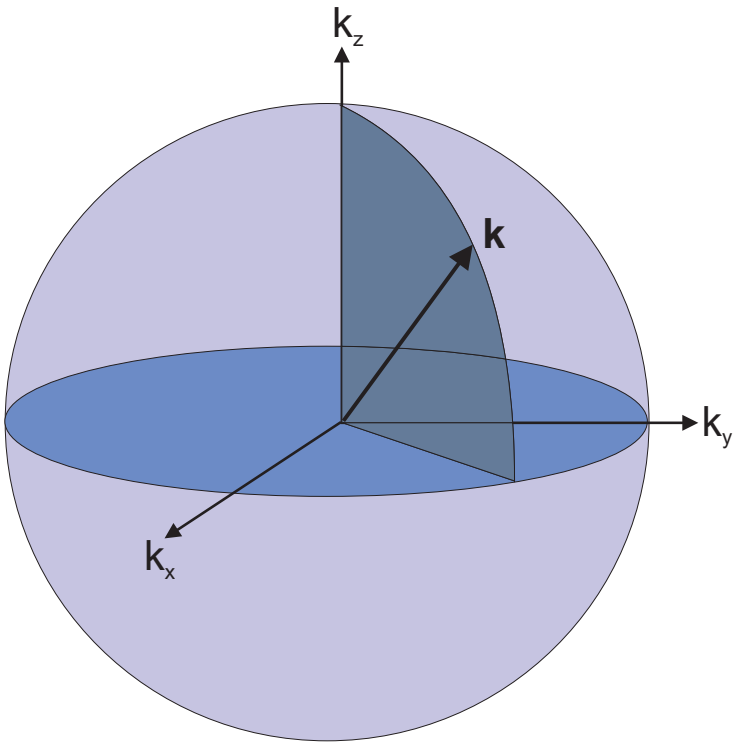


Figure 3.6: Spherical surface in **k**-space for electrons in a three-dimensional crystalline material with isotropic effective mass.

vector in **k**-space, then the energy of the electron is

$$E = \frac{\hbar^2}{2m}(k_x^2 + k_y^2 + k_z^2) = \frac{\hbar^2|\mathbf{k}|^2}{2m}, \tag{3.9}$$

meaning that vectors of the same magnitude have the same energy, forming spherical shells (Fig. 3.6). Classically, all values of energy would be allowed and there would be no restriction on the number of electrons with the same value of

**k**. However, at the atomic scale, the uncertainty and exclusion principles come into play, which means that the wave function for the electron must satisfy the Schrödinger equation, subject to boundary conditions. With the DOS, the situation is complicated by energy degeneracy. That is, for some of the allowed energy levels, there are more than one possible combination of components in $k$-space that will give the same energy. In general, the total DOS can be expressed as

$$g(E) = \frac{2}{V_{BZ}} \sum_{n} \int_{\Omega'} \delta(E - E_n(\mathbf{k}))\mathrm{d}\mathbf{k}, \tag{3.10}$$

where $\Omega'$ is the unit cell volume in reciprocal space and $n$ is the band index. The sum in eqn. (3.10) is over all energy bands and the integral is over all $k$-points in reciprocal space while the factor of two accounts for the spin-up and spin-down electrons.

For a system such as $Ge_2Sb_2Te_5$ built out of three atom types, it is desirable to express the relative contribution of the atoms to the total DOS by calculating the projected density of states for each atom. The projected DOS of the atom of type $t$ is given by

$$g_l^t(E) = \frac{2}{V_{BZ}} \sum_{n} \int_{\Omega'} Q_l^t \, \delta(E - E_n(\mathbf{k}))\mathrm{d}\mathbf{k}, \tag{3.11}$$

where $Q_l^t$ is the partial charge of an atom and $l$ is the atomic orbital index. When plots of the projected DOS are matched with the plots of the total DOS, it can be shown which atom and which orbital delivers the biggest contribution to the total DOS of the system.

A more detailed view of a material's electronic structure is often possible by examination of its band structure from which the band gap can be evaluated. The band structure represents the energy of the available electronic states along a series of lines in reciprocal space that typically forms a closed loop beginning and ending at the Γ-point (Fig. 3.7).

In this study, the electronic band structures and the corresponding density

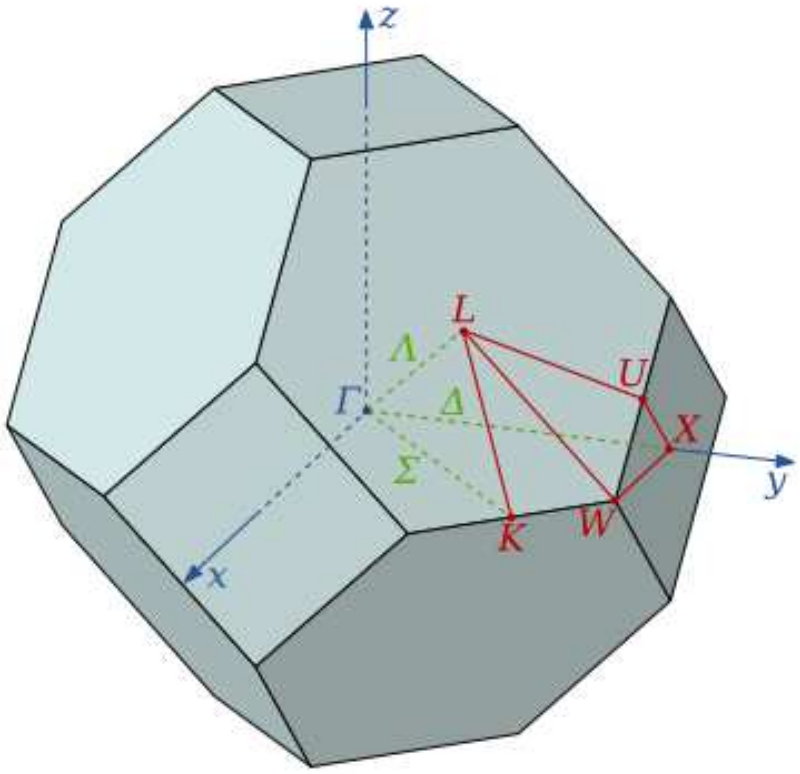


Figure 3.7: First Brillouin zone of fcc lattice showing symmetry labels for high symmetry lines and points.

of states for hexagonal and cubic GST were computed at the equilibrium lattice constants. The first step involved the usual SCF calculation where the Kohn-Sham orbitals were expanded on a plane-wave basis set upto 50 Ry for both hexagonal and cubic GST. $k$-grids of $14 \times 14 \times 4$ and $14 \times 14 \times 2$ were used for hexagonal and cubic GST structures, respectively.

## 3.9 Calculation of Optical Properties

DFT [10, 11] is a ground-state theory and does not take into account many-body effects. Thus, it is inadequate for analyzing material properties such as band structure and optical absorption which involve electronic excitation. However, dielectric properties of materials, which do not involve electronic ex-

citation, can be analyzed using DFT [10, 11]. In this study, the dielectric function ($\epsilon$) was calculated within the framework of DFT as implemented in QUANTUM ESPRESSO [9]. From the calculated dielectric function, the refractive index ($n$), extinction coefficient ($k$), reflectivity ($R$) and conductivity ($\sigma$) were obtained. The refractive index ($n$) and the extinction coefficient ($k$) were calculated using the expressions [93, 94]:

$$n = \sqrt{\frac{|\epsilon| + \epsilon_1}{2}}, \tag{3.12}$$

$$k = \sqrt{\frac{|\epsilon| - \epsilon_1}{2}}, \tag{3.13}$$

were $|\epsilon| = \sqrt{\epsilon_1^2 + \epsilon_2^2}$ is the modulus of the complex dielectric function whose real and imaginary parts are $\epsilon_1$ and $\epsilon_2$, respectively. The reflectivity was calculated using the relation [93, 94]:

$$R = \frac{(n-1)^2 + k^2}{(n+1)^2 + k^2}. \tag{3.14}$$

A high reflectivity contrast is a prerequisite for a high signal-to-noise ratio. The reflectivity contrast ($C$) was calculated using the relation [95]:

$$C = 2 \times \left| \frac{R_1 - R_2}{R_1 + R_2} \right| \times 100\%, \tag{3.15}$$

where $R_1$ and $R_2$ denote the reflectivity of two different phases, cubic and hexagonal structures in this case. The real part of the optical conductivity, $\sigma_1$, was calculated using the relation [93, 94]:

$$\sigma_1 = \frac{\omega}{4\pi}\epsilon_2, \tag{3.16}$$

where $\omega$ is the frequency.

Optical absorption spectra for hexagonal and cubic $Ge_2Sb_2Te_5$ were calculated from first principles using TDDFT and MBPT as implemented in the code `turboTDDFT` [52] (within QUANTUM ESPRESSO [9]) and Yambo [96], re-

spectively. In MBPT, the spectrum was calculated using the partially self consistent $GW_0$ correction to the electronic self-energy, $\sum$.

# Chapter 4
# Results and Discussion

## 4.1 Convergence Criteria

Figs. 4.1-4.4 show the convergence of the total energy with respect to the kinetic energy cutoff and $k$-grid, calculated using the local density approximation for the XC energy functional. Figs. 4.5-4.8 show the convergence of the total energy with respect to the kinetic energy cutoff and $k$-grid, calculated using the generalized gradient approximation for the XC energy functional. From the graphs of total energy versus kinetic energy cut-off, the total energy is seen to stabilize beyond 50 Ry. Subsequently, a value of 50 Ry was chosen for the kinetic energy cut-off. Similarly, from the graphs of total energy versus $k$-grid, the total energy is seen to stabilize beyond $8 \times 8 \times 8$. Subsequently, a $k$-grid of $8 \times 8 \times 8$ was used in this study.

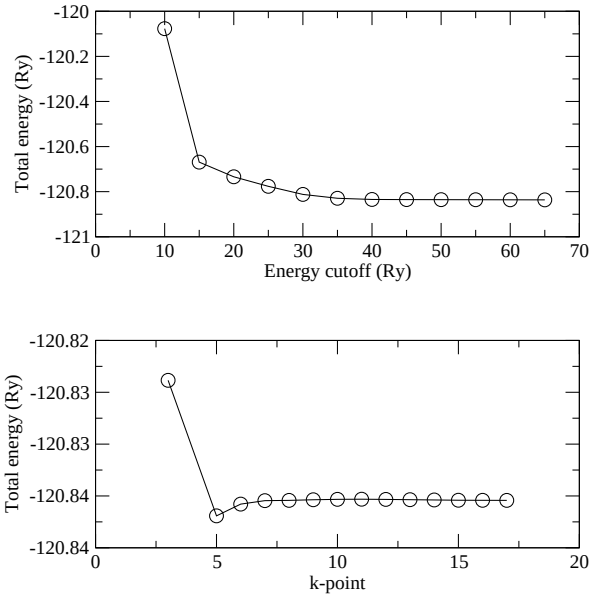


Figure 4.1: The LDA convergence criteria for phase A of hexagonal GST.

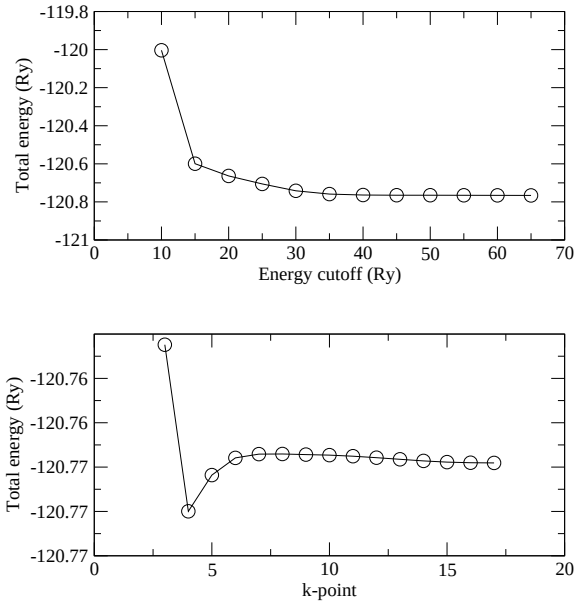


Figure 4.2: The LDA convergence criteria for phase B of hexagonal GST.

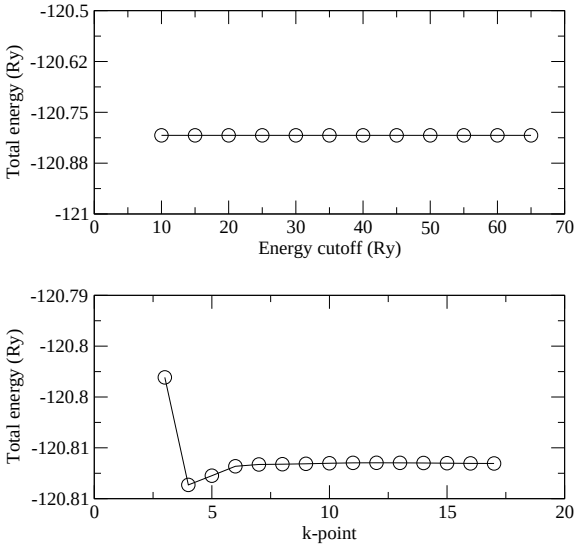


Figure 4.3: The LDA convergence criteria for phase C of hexagonal GST.

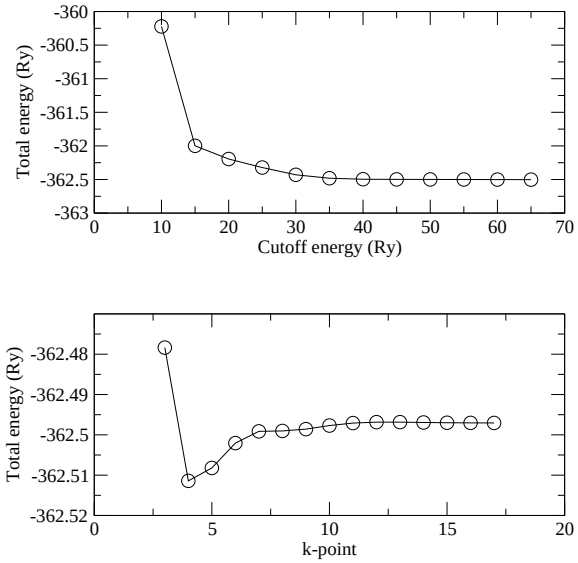


Figure 4.4: The LDA convergence criteria for cubic GST.

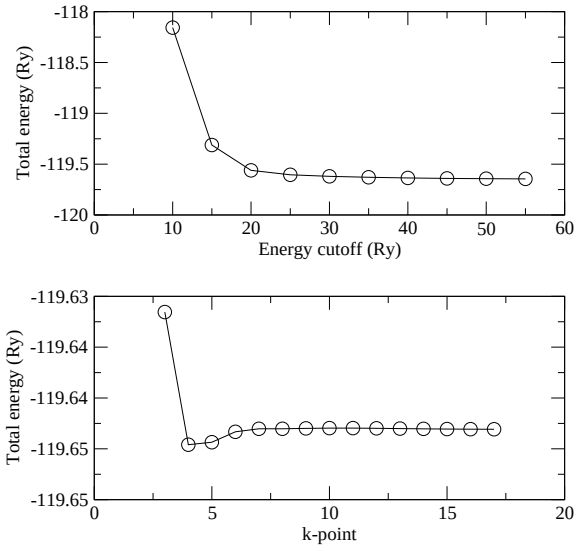


Figure 4.5: The GGA convergence criteria for phase A of hexagonal GST.

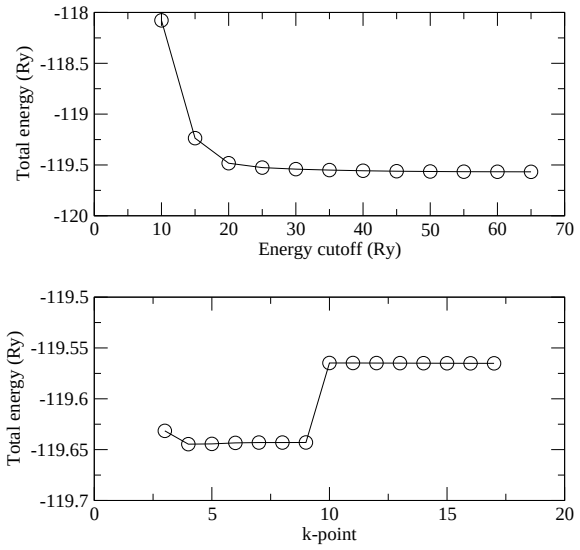


Figure 4.6: The GGA convergence criteria for phase B of hexagonal GST.

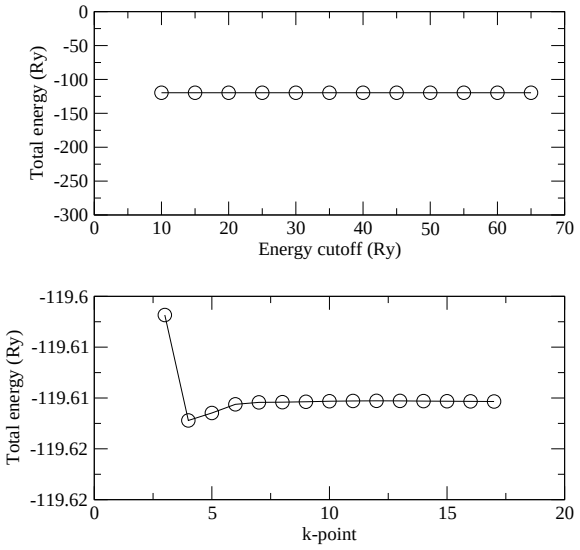


Figure 4.7: The GGA convergence criteria for phase C of hexagonal GST.

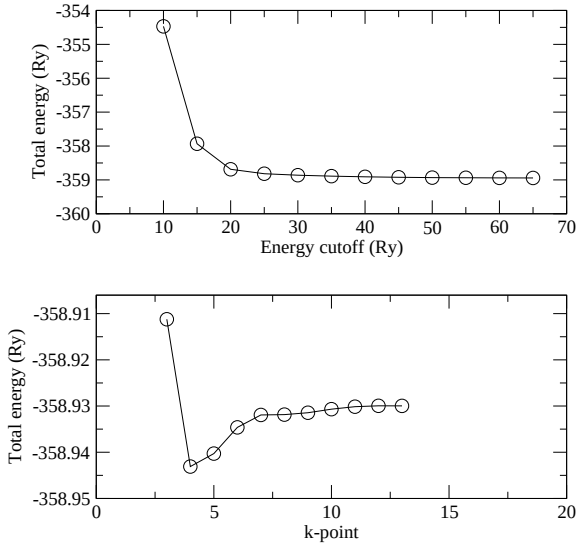


Figure 4.8: The GGA convergence criteria for cubic GST.

## 4.2 Structural Properties

For each structure, the total energy was calculated for a number of unit cell volumes. The energy versus volume data were then fitted to the Murnaghan equation of state [91]. The results are shown in Tables 4.1-4.4 in which $a$ (in a.u.) and $c$ (in a.u.) are the equilibrium lattice constants, $c/a$ is the axial ratio, $V_0$ (in a.u.$^3$) is the equilibrium unit cell volume, $B_0$ is the bulk modulus (in GPa) and $B_0'$ is the pressure derivative of the bulk modulus. The last columns give the percentage deviation from experiment. For GGA calculations, the percentage deviation is enclosed in brackets. The calculated lattice parameters hold for zero pressure and temperature since DFT is a ground state theory. However, experimental measurements of lattice parameters are generally done at non-zero temperature and pressure. This partly accounts for the error in calculating the lattice parameters.

**Table 4.1** LDA and GGA lattice parameters for phase A of hexagonal GST.

| | LDA | GGA | Exp. | % deviation |
|---|---|---|---|---|
| a | 7.81 | 8.21 | 8.034[a] | -2.79%(2.19%) |
| c | 31.38 | 32.60 | 32.647[a] | -3.88%(-0.14%) |
| c/a | 4.02 | 3.97 | 4.064[a] | -1.08%(-2.31%) |
| $V_0$ | 1720.30 | 1900.64 | | |
| $B_0$ | 56.5 | 44.0 | 44[b] | 28.4%(0%) |
| $B_0'$ | 6.21 | 3.25 | 4[b] | 55.25%(-18.75%) |

[a]Experimental data are from [41].

[b]Experimental data are from [97].

**Table 4.2** LDA and GGA lattice parameters for phase B of hexagonal GST.

| | LDA | GGA | Exp. | % deviation |
|---|---|---|---|---|
| a | 8.00 | 8.21 | 8.034[a] | -0.43%(2.19%) |
| c | 31.61 | 32.98 | 32.647[a] | -3.18%(1.02%) |
| c/a | 3.95 | 4.02 | 4.064 [a] | -2.81%(-1.08%) |
| $V_0$ | 1808.49 | 1900.72 | | |
| $B_0$ | 57.5 | 50.8 | 44[b] | 30.68%(15.45%) |
| $B_0'$ | 2.71 | 3.46 | 4[b] | -32.25%(-13.5%) |

[a]Experimental data are from [41].

[b]Experimental data are from [97].

**Table 4.3** LDA and GGA lattice parameters for phase C of hexagonal GST.

| | LDA | GGA | Exp. | % deviation |
|---|---|---|---|---|
| a | 8.00 | 8.21 | 8.034[a] | -0.43%(2.19%) |
| c | 31.59 | 32.78 | 32.647[a] | -3.24%(0.41%) |
| c/a | 3.95 | 3.99 | 4.064[a] | -2.81%(-1.82%) |
| $V_0$ | 1807.28 | 1899.53 | | |
| $B_0$ | 57.3 | 52.2 | 44[b] | 30.23%(18.64%) |
| $B_0'$ | 1.45 | 2.43 | 4[b] | -63.75%(-39.25%) |

[a]Experimental data are from [41].

[b]Experimental data are from[97].

**Table 4.4** LDA and GGA lattice parameters for cubic GST.

| | LDA | GGA | Exp. | % deviation |
|---|---|---|---|---|
| a | 7.80 | 7.80 | 8.053[a] | -3.14%(-3.14%) |
| c | 95.64 | 99.41 | 98.544[a] | -2.95%(0.89%) |
| c/a | 12.26 | 12.74 | 12.237[a] | 0.19%(4.11%) |
| $V_0$ | 5190.92 | 5190.96 | | |
| $B_0$ | 55.3 | 59.2 | 39[b] | 41.80%(51.79%) |
| $B_0'$ | 4.74 | 3.642 | 4 [b] | 18.5%(8.95%) |

[a]Experimental data are from [86].

[b]Experimental data are from [97].

A comparison of total energies can give an indication of the relative stability of structures. Generally, the structure with the lowest total energy at equilibrium volume is considered to be the most stable. In Fig. 4.9, the fitted

energy versus volume curves for the three possible stacking sequences of hexagonal GST are reported . Table 4.5 shows the total energies at equilibrium of phases A, B and C of hexagonal GST. For both LDA and GGA calculations, phase A has the lowest total energy at equilibrium. In Table 4.6, the total energies after structural relaxation of the three phases of hexagonal GST are compared.

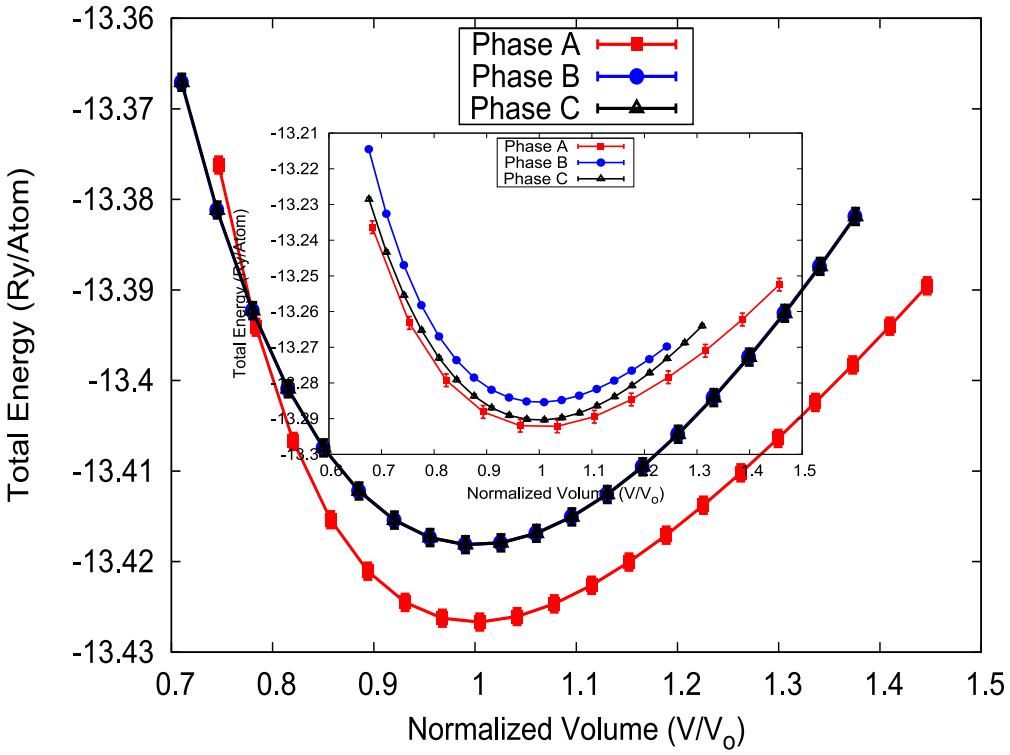


Figure 4.9: The LDA and GGA (inset) total energy versus normalized volume for phases A, B and C of hexagonal GST. In some cases the error bars are smaller than the symbol used.

**Table 4.5** The LDA and GGA total energies (Ry/atom) at equilibrium for phases A, B and C of hexagonal GST. The associated errors are enclosed in brackets.

| | Phase | | |
|---|---|---|---|
| | Phase A | Phase B | Phase C |
| LDA | -13.42668(±0.00087) | -13.41816(±0.00036) | -13.42285(±0.00088) |
| GGA | -13.29241(±0.00179) | -13.28541(±0.00016) | -13.29040(±0.00054) |

**Table 4.6** The LDA and GGA total energies (Ry/atom) after structural relaxation of phases A, B and C of hexagonal GST.

| | Phase | | |
|---|---|---|---|
| | Phase A | Phase B | Phase C |
| LDA | -13.4262 | -13.4259 | -13.4267 |
| GGA | -13.2941 | -13.2928 | -13.2937 |

LDA calculations suggest that phase C is marginally lower in energy than phase A after structural relaxation, with an energy difference of 0.000305 Ry/atom ($\sim$ 4 meV/atom). This difference is of the same order of magnitude expected for the free energy contribution (at 300 K) due to the configurational entropy of the disordered phase C ($\frac{4}{9}k_B\,ln\,2 = 8$ meV/atom) [98]. Using the B3PW hybrid functional, Becke [99] has also found that phase C has a slightly lower energy after structural relaxation. On the other hand, GGA calculations in this study show that phase A has the lowest energy after structural relaxation, in agreement with other theoretical studies using the GGA for the XC energy functional [98, 100]. It can be concluded that the hierarchy in energy between phases A and C depends, to a larger extent, on the choice for the XC energy

functional. Hence, on the basis of energetics, phases A and C seem to be plausible candidates for hexagonal GST. In this study, phase A has been adopted for purposes of comparison with other studies.

Fig. 4.10 shows the fitted energy versus volume curves for hexagonal GST (phase A) as well as cubic GST. The corresponding total energies at equilibrium volume are shown in Table 4.7. It is evident that hexagonal GST has a slightly lower energy at equilibrium for both LDA and GGA calculations.

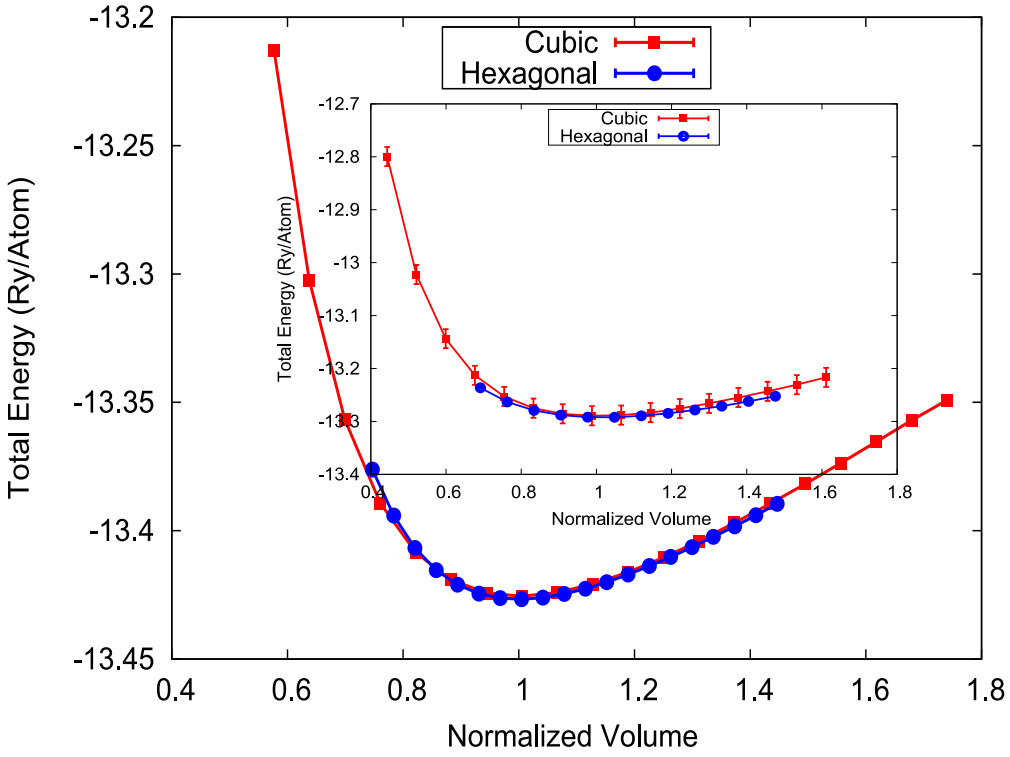


Figure 4.10: The LDA and GGA (inset) total energy as a function of volume for cubic and hexagonal GST.

**Table 4.7** The LDA and GGA total energies (Ry/atom) at equilibrium for hexagonal and cubic GST. The associated errors are enclosed in brackets.

| | Phase | |
|---|---|---|
| | Hexagonal | Cubic |
| LDA | -13.42668(±0.00087) | -13.42552(±0.00170) |
| GGA | -13.29241(±0.00179) | -13.28934(±0.01812) |

**Table 4.8** The LDA and GGA total energies (Ry/atom) after structural relaxation of hexagonal and cubic GST.

| | Phase | |
|---|---|---|
| | Hexagonal | Cubic |
| LDA | -13.42620 | -13.42584 |
| GGA | -13.29412 | -13.29173 |

In Table 4.8, the total energies of hexagonal and cubic GST after structural relaxation are compared. It is evident that for both LDA and GGA calculations, hexagonal GST is marginally lower in energy. Hence, the hexagonal phase is slightly stable than the cubic phase. This is later confirmed through phonon calculations.

In Table 4.9, the lattice parameters for hexagonal and cubic GST are compared with experiment and other theoretical studies. Compared to experimental values, it is evident from Table 4.9, together with Tables 4.1-4.4, that the LDA tends to underestimate whereas the GGA tends to overestimate lattice parameters and the unit cell volume. This is an observation that has been reported in the literature [101]. It is also evident from Table 4.9, together with Tables 4.1-4.4, that lattice constants calculated using the GGA are more accurate than lattice constants calculated using the LDA for the XC energy

functional. Theoretical studies available in the literature show that explicit inclusion of the semi-core $Te$ $4d$ electrons in the valence states results in more accurate lattice constants and bulk moduli for Telluride compounds as compared to experiment and all-electron calculations [102, 103].

**Table 4.9** The LDA and GGA (in brackets) lattice constants for hexagonal and cubic GST compared with experiment and other theoretical studies.

| | Hexagonal | | | |
|---|---|---|---|---|
| | This Study | Exp. | Others | % Dev. |
| a | 7.81(8.21) | 8.034[a] | 8.091[c], 8.072[e] | -2.8%(2.19%) |
| c | 31.38(32.60) | 32.647[a] | 32.722[c], 33.819[e] | -3.9%(-0.14%) |
| c/a | 4.02(3.97) | 4.064[a] | 4.044[c], 4.19[e] | -1.1%(-2.31%) |
| $V_0$ | 1720.30(1900.64) | | | |
| $B_0$ | 56.5(44.0) | 44[g] | | 28.4%(0%) |
| $B_0'$ | 6.21(3.25) | 4[g] | | 55.3%(-18.75%) |
| | Cubic | | | |
| | This Study | Exp. | Others | % Dev. |
| a | 7.80(7.80) | 8.053[b] | 8.11[d], 8.072[f] | -3.1%(-3.14%) |
| c | 95.64(99.41) | 98.544[b] | 100.38[d], 104.121[f] | -2.9%(0.89%) |
| c/a | 12.26(12.74) | 12.237[b] | 12.38[d], 12.899[f] | 0.19%(4.11%) |
| $V_0$ | 5190.92(5190.96) | | | |
| $B_0$ | 55.3(59.2) | 39[g] | | 41.8%(51.79%) |
| $B_0'$ | 4.74(3.642) | 4[g] | | 18.5%(8.95%) |

[a]Experimental data are from [41].

[b]Experimental are from [86].

[c]Theoretical data are from [98].

[d]Theoretical data are from [104]

[e,f]Theoretical data are from [105]; [g]Experimental data are from [97].

For example, the calculated lattice constant for the rocksalt-like structure of $GeTe$ is found to be smaller than the experimental value by more than 5% without the inclusion of the $Te$ $4d$ orbitals in the valence states [79]. In this study, the GGA pseudopotential included the semi-core $Te$ $4d$ in the valence states whereas the LDA pseudopotential did not. In Table 4.9, the lattice parameters for hexagonal and cubic GST have been underestimated by as much as 3.1% without the inclusion of $Te$ $4d$ electrons in the valence states.

The bulk modulus can be defined as a measure of stiffness. It is evident from Table 4.9, together with Tables 4.1-4.4, that the LDA bulk moduli are, in general, greater than the GGA bulk moduli. This is consistent with the earlier observation that the LDA underestimates lattice constants whereas the GGA overestimates lattice constants. Smaller lattice constants correspond to stronger bonds resulting in increased stiffness whereas larger lattice constants correspond weaker bonds and the result is reduced stiffness. The pressure derivative of the bulk modulus is a dimensionless constant and the calculated values compare well with experiment for both hexagonal and cubic GST.

Table 4.10 shows the dependence of lattice parameters and formation energy on $N$ content. It is evident that lattice parameters increase with increasing $N$ content. Jeong *et al* [106] have used x-ray diffraction technique to study the structure and microstructure of $N$-doped GST (NGST). In that study, lattice parameters were found to increase with rising $N$ content. As already noted, $N$ occupies interstitial sites. This stretches the unit cell and makes lattice parameters to increase. It is also clear from Table 4.10 that the formation energy of hexagonal GST becomes more negative whereas that of cubic GST becomes more positive with rising $N$ content. That is, hexagonal GST becomes more stable whereas cubic GST becomes more unstable with rising $N$ content.

**Table 4.10** Dependence of lattice parameters and formation energy $E_f$ (Ry/atom) on $N$ content for hexagonal and cubic GST.

| | Hexagonal GST | | |
|---|---|---|---|
| | Nitrogen Content at. % | | |
| | 0 | 10 | 25 |
| $a$ | 8.200 | 8.207 | 8.210 |
| $c$ | 31.258 | 40.474 | 43.168 |
| $B_0$ | 65.4 | 84.9 | 86.8 |
| $B_0'$ | 2.85 | 5.075 | 5.675 |
| $E_f$ | 0 | -0.0131 | -0.0382 |

| | Cubic GST | | |
|---|---|---|---|
| | Nitrogen Content at. % | | |
| | 0 | 10 | 25 |
| $a$ | 7.799 | 8.201 | 8.602 |
| $c$ | 105.914 | 120.00 | 124.984 |
| $B_0$ | 69.65 | 78.45 | 66.85 |
| $B_0'$ | 3.76 | 5.22 | 2.315 |
| $E_f$ | 0 | 0.0060 | 0.0088 |

**Table 4.11** LDA and GGA (in brackets) bond lengths (a.u.) for hexagonal GST compared to values from experiment and other theoretical calculations.

| | This Study | Experiment[a] | Others |
|---|---|---|---|
| $Ge-Te$ | 5.48, 5.51(5.75, 5.69) | 5.46, 6.03 | 5.65[b], 5.69[b]; 5.34[c], 5.41[c] |
| $Sb-Te$ | 5.59, 5.87(6.08, 5.72) | 5.46, 6.03 | 5.69[b], 6.03[b]; 5.46[c], 5.61[c] |

[a]Experimental data are from reference [83].

[b]Theoretical data are from reference [98].

[c]Theoretical data are from reference [40]

**Table 4.12** LDA and GGA (in brackets) bond lengths (a.u.) for cubic GST compared to values from experiment and other theoretical calculations.

| | This Study | Experiment[a] | Others |
|---|---|---|---|
| $Ge-Te$ | 5.59, 5.52(5.75, 5.69) | 5.35, 6.05 | 5.43[b], 6.12[b]; 5.67[c], 5.71[c] |
| $Sb-Te$ | 5.58, 5.86(6.08, 5.72) | 5.50, 6.05 | 5.60[b], 6.24[b]; 5.69[c], 6.05[c] |

[a]Experimental data are from reference [89].

[b]Theoretical data are from reference [105].

[c]Theoretical data are from reference [40]

Understanding the structure of a solid requires a knowledge of not only the lattice constants but also the bond lengths and bond angles (i.e. angle between each pair of bonds to the same atom). In Tables 4.11 and 4.12, the calculated bond lengths for hexagonal and cubic GST, respectively, are reported alongside experimental values and other theoretical calculations. It is evident that two different bond lengths exist for $Ge-Te$ and $Sb-Te$ bonds in both phases. This is in agreement with experiment and other theoretical calculations. In subsequent discussion, this phenomenon has been referred to as *bond length splitting* and the difference between the two values is denoted by $\Delta_b$.

**Table 4.13** LDA and GGA (in brackets) bond length difference, $\Delta_b$, for hexagonal GST.

| | This Study | Experiment[a] | Others |
|---|---|---|---|
| $Ge-Te$ | 0.04(0.05) | 0.57[c] | 0.04[a], 0.07[b] |
| $Sb-Te$ | 0.28(0.36) | 0.57[c] | 0.34[a], |

[a]Theoretical data are from reference [98].

[b]Theoretical data are from reference [40].

[c]Experimental data are from reference [83]

**Table 4.14** LDA and GGA (in brackets) bond length difference, $\Delta_b$, for cubic GST.

| | This Study | Experiment[a] | Others |
|---|---|---|---|
| $Ge-Te$ | 0.07(0.05) | 0.07[c] | 0.69[a], 0.04[b] |
| $Sb-Te$ | 0.28(0.33) | 0.55[c] | 0.55[a] |

[a]Theoretical data are from reference [105].

[b]Theoretical data are from reference [40].

[c]Experimental data are from reference [89].

In Tables 4.13 and 4.14, the calculated $\Delta_b$ values are compared with experiment and other theoretical calculations. In this study, there was no $Sb-Ge$ bond detected, in agreement with the fact that $Sb$ and $Ge$ do not intermix in the solid phase. Also, there was no $Te-Te$ bond detected.

**Table 4.15** LDA and GGA (in brackets) bond angles (°) for hexagonal and cubic GST.

| | Phase | |
|---|---|---|
| | Hexagonal | Cubic |
| $Te-Ge-Te$ | 89.4-179.4(88.3-170.2) | 90.0-179.6(88.7-179.3) |
| $Sb-Te-Sb$ | 83.4, 88.7(84.9, 91.6) | 83.4, 88.7(81.3, 87.8) |
| $Ge-Te-Ge$ | - | 90.0-180.0(88.7-91.3) |
| $Ge-Te-Sb$ | 92.7, 174.8(91.3, 174.9) | 92.9, 175.0(94.1, 174.6) |
| $Te-Sb-Te$ | 93.9(91.6) | 83.4-176.4(81.3-175.9) |

In Table 4.15, the calculated bond angles for the configurations $Te-Ge-Te$, $Te-Sb-Te$ and $X-Te-X$, where $X \equiv Ge/Sb$, are reported. It is important to note that QUANTUM ESPRESSO does not give the angular distribution or weight of the configurations. The angular distribution or weight of a configuration refers to the relative number of the configuration as a function of angle. Nevertheless, the calculated bond angles are between 60° and 180°, in agreement with experiment. In a recent experimental study, Akola and Jones [107] have determined the angular distribution of the various possible configurations to be in the range 60° - 120° and 150° - 180° for crystalline GST. In particular, it was established in that study that the angular distribution for configurations centered around $Ge$ and $Sb$ have a pronounced maximum at 90° and a weaker peak at 180°, indicating octahedral features. Moreover, the angular distribution for configurations centered around $Te$ was found to have a pronounced maximum around 90° but a much weaker peak near 180° compared to configurations centered around $Ge$ or $Sb$ [107]. From EXAFS measurements and first principles calculations, it has been shown that the local structure around $Ge$ changes from six-fold co-ordination in the crystalline state to four-fold coordination in the amorphous state [75].

Experimental studies suggest that there is no pressure-induced transition between hexagonal and cubic GST structures. Kolobov *et al* [108] have shown that cubic GST becomes amorphous under hydrostatic pressure at around 10 GPa. This phenomenon has been shown to be general and can be observed for other compositions along the pseudobinary line $(GeTe)_m(Sb_2Te_3)_n$ [109]. Subsequent studies have shown that this pressure-induced amorphization is independent of temperature [110]. Krbal *et al* [97] have shown that while metastable GST becomes amorphous under hydrostatic compression at around 15 GPa, stable GST remains crystalline. Upon higher hydrostatic compression, a body-centered cubic phase is obtained in both cases at around 30 GPa. On hydrostatic decompression, the amorphous phase is retained for the starting cubic phase while the initial structure is recovered for the starting hexagonal phase [97].

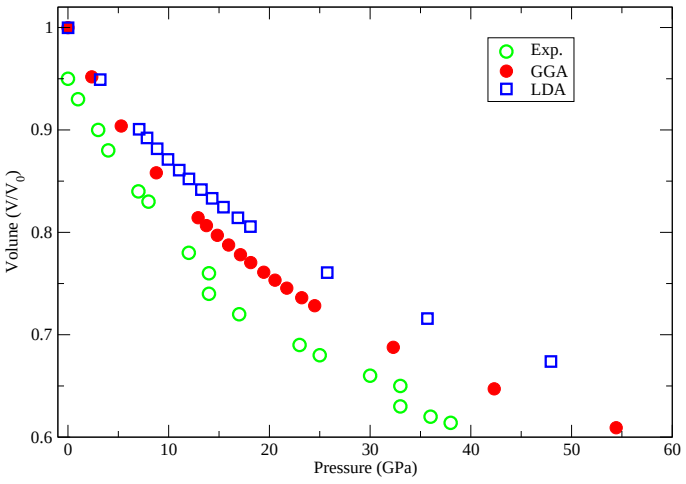


Figure 4.11: Unit cell volume as a function of pressure for hexagonal GST. Experimental data is due to Krbal [97].

A way of determining pressure-induced structural transition is by monitoring discontinuities in the volume versus pressure curves. The dependence of

volume on pressure for hexagonal and cubic GST is reported in Figs. 4.11 and 4.12, respectively. Discontinuities are evident along the experimental curves whereas the theoretical curves do not show any obvious discontinuities. Nevertheless, it is still possible to demonstrate pressure-induced structural transition using alternative ways such as the common-tangent method and the intersection of pressure-enthalpy curves.

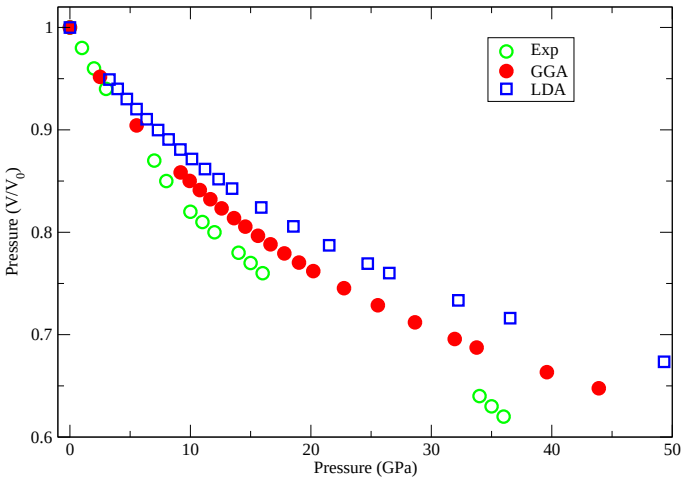


Figure 4.12: Unit cell volume as a function of pressure for cubic GST. Experimental data is due to Krbal [97].

## 4.3 Thermal Properties

Fig. 4.13 and 4.14 show the phonon dispersion spectra and the associated vibrational density of states (VDOS) for hexagonal and cubic GST structures, respectively. It is evident that the phonon spectra for hexagonal and cubic GST structures are almost similar in profile except for the fact that the cubic phase has a more dense set of curves. The absence of negative frequencies in the phonon spectrum for hexagonal GST is an indication that the structure is stable.

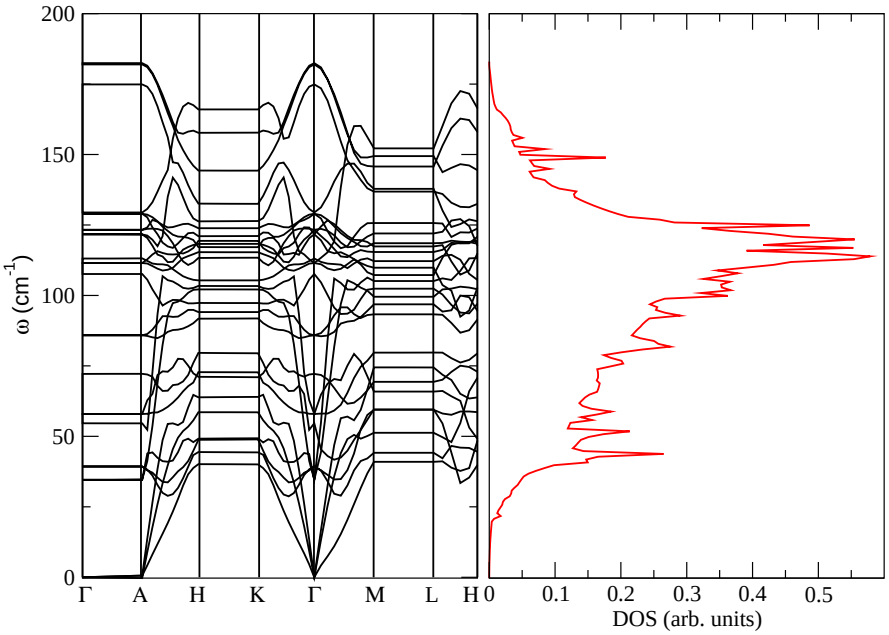


Figure 4.13: Phonon dispersion (left) and the corresponding density of states (right) for the hexagonal GST structure.

On the other hand, the presence of negative frequencies in the phonon spectrum for cubic GST is an indication that the structure is unstable. This structure is often referred to as metastable, and it is the one involved in the reversible crystalline-to-amorphous phase transformation that finds application in phase-change memory technology [111]. The phonon spectrum of hexagonal GST structure shows a set of 27 branches that stretches from 0 $cm^{-1}$ to about 182 $cm^{-1}$. This corresponds to 9 atoms in the unit cell with each atom having 3 modes, giving a total of 27 modes. In addition, the phonon spectrum has 6 acoustic branches (i.e. branches having zero frequency at the Γ-point), leaving a majority of 21 optical branches (i.e. branches having non-zero frequency at the Γ-point). On the other hand, the phonon spectrum of cubic GST structure shows a set of 81 branches spanning from about -21 $cm^{-1}$ to about 186 $cm^{-1}$.

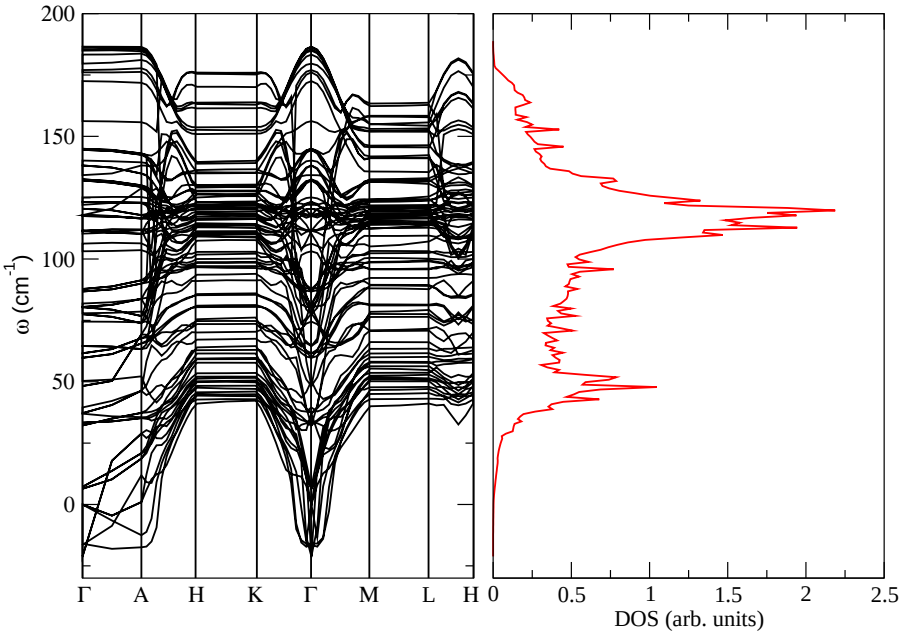


Figure 4.14: Phonon dispersion (left) and the corresponding density of states (right) for the cubic GST structure.

This corresponds to 27 atoms per unit cell, each atom having 3 modes, giving a total of 81 modes. The vibrational density of states gives the number of modes per unit frequency per unit volume of real space.

The top panel of Fig. 4.15 shows the calculated heat capacity ($C_V$) as a function of temperature ($T$) for hexagonal and cubic GST. The bottom panel of Fig. 4.15 zooms in on the same curves in the low temperature region. It is evident that $C_V \rightarrow 0$ as $T \rightarrow 0$ for both hexagonal and cubic GST, in agreement with the Debye model of specific heats. For cubic GST, $C_V$ has a linear dependence on temperature as $T \rightarrow 0$ whereas for hexagonal GST, $C_V$ has a cubic dependence on temperature as $T \rightarrow 0$. However, the Debye model of specific heats predicts that $C_V$ should have a cubic dependence on temperature as $T \rightarrow 0$. Heat capacity can be expressed as:

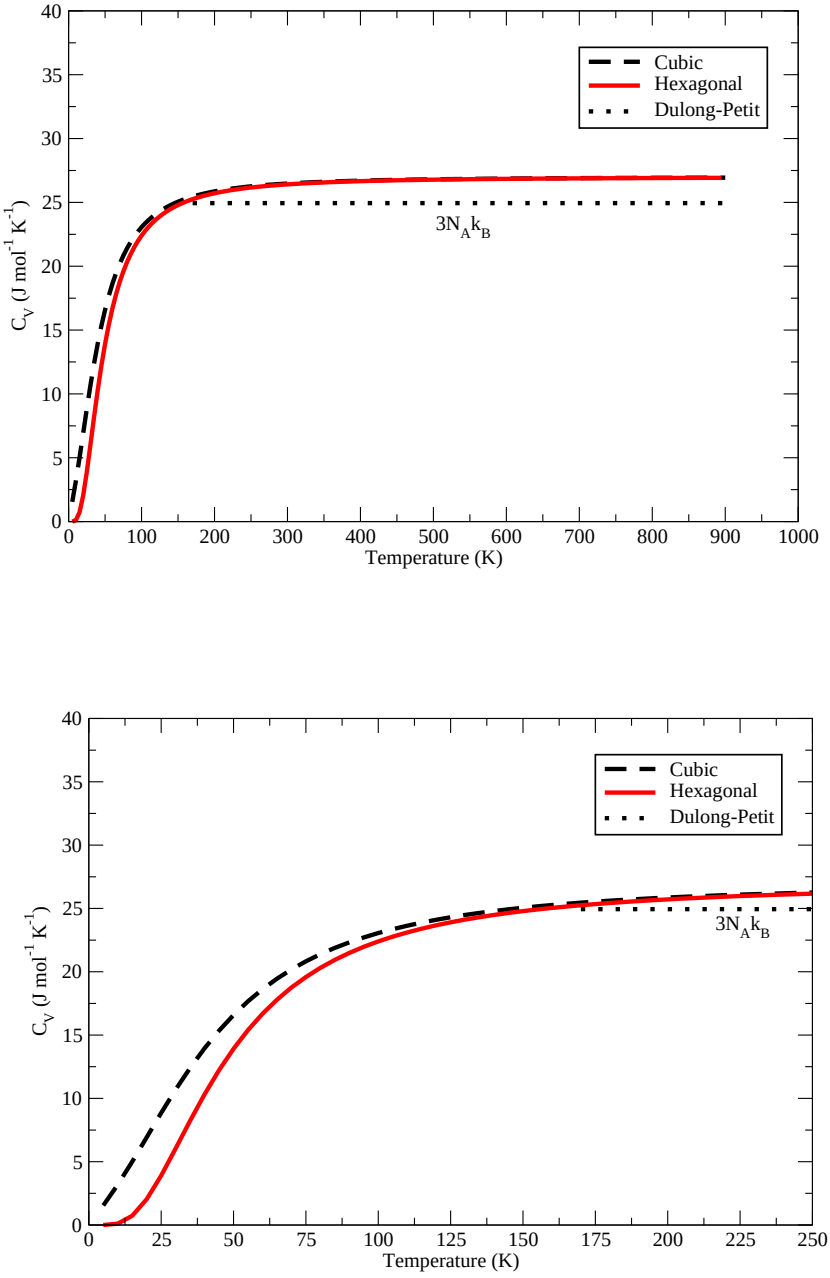


Figure 4.15: The top panel shows heat capacity curves for hexagonal and cubic GST. The bottom panel shows the same curves at low temperatures.

$$C_V = (C_V)_{ele} + (C_V)_{pho}, \tag{4.1}$$

where $(C_V)_{ele}$ is the electronic contribution and $(C_V)_{pho}$ is the phonon/lattice contribution to the heat capacity. $(C_V)_{ele}$ has a linear dependence on temperature whereas $(C_V)_{pho}$ has a cubic dependence on temperature. Zalden *et al* [112] have estimated that the electronic contribution to the specific heat of cubic GST is less than 0.08 J$\cdot$ mol$^{-1}\cdot$ K$^{-1}$, irrespective of the temperature. Hence, as $T \to 0$, the electronic contribution is predominant in the cubic phase. This explains the linear dependence of $C_V$ on $T$ as $T \to 0$ for cubic GST. On the other hand, heat capacity at high temperatures is significantly larger than 0.08 J$\cdot$ mol$^{-1}\cdot$ K$^{-1}$, an indication that the phonon contribution is predominant in that region for cubic GST. In this study, the Debye temperature ($\theta_D$) was found to be 197 K for hexagonal GST and 137 K for cubic GST. Above $\theta_D$, the heat capacity approaches a limiting value. However, this limiting value is apparently larger than the predicted Dulong-Petit limit, $C_V = 3R = 3N_A k_B \approx 24.944$ J $\cdot$ mol$^{-1}$ $\cdot$ K$^{-1}$. The increase of $C_V$ above the Dulong-Petit limit at high temperatures is in agreement with experiment [113–115]. Due to a low Debye temperature, the Dulong-Petit limit is always exceeded [113]. Kalb *et al* [114] attributes this effect to chemical disorder and point defects. According to Kuwahara *et al* [115], the heat capacity slightly increases in the high temperature region as the result of structural relaxation of point defects. Point defects such as vacancies, self-interstitials and extra atoms (not in regular lattice positions) can strongly affect the properties of materials. When point defects are thermally generated, their energy of formation gives an extra contribution to the heat capacity of the crystal. Thus, the creation of point defects provides an additional component to the heat capacity, $(C_V)_{def}$. Hence, $C_V$ can be expressed as:

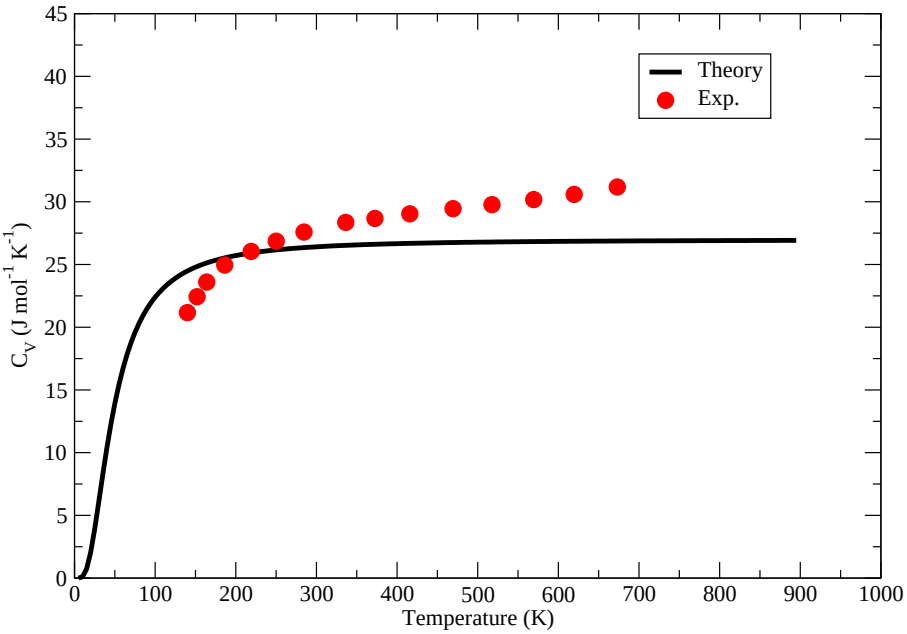


Figure 4.16: Theoretical and experimental heat capacity curves for hexagonal GST. Experimental data is due to Kuwahara *et al* [115].

$$C_V = (C_V)_{pho} + (C_V)_{ele} + (C_V)_{def}, \tag{4.2}$$

where $(C_V)_{def}$ is the contribution to the heat capacity from lattice defects. From Fig. 4.15, it is clear that the cubic phase has a slightly higher heat capacity than the hexagonal phase within the range 0-200 K. Zalden *et al* [112] have shown that the heat capacity of crystalline GST is related to disordered vacancies. In that study, it is apparent that there is an enhancement of the heat capacity for the disordered cubic phase as compared to the ordered hexagonal phase. Configurational disorder results in a higher formation energy required to generate vacancies in cubic GST. This accounts for the slightly higher $C_V$ for cubic GST as compared to hexagonal GST. The calculated heat capacity is compared with experiment in Figs. 4.16 and 4.17. For both hexagonal and

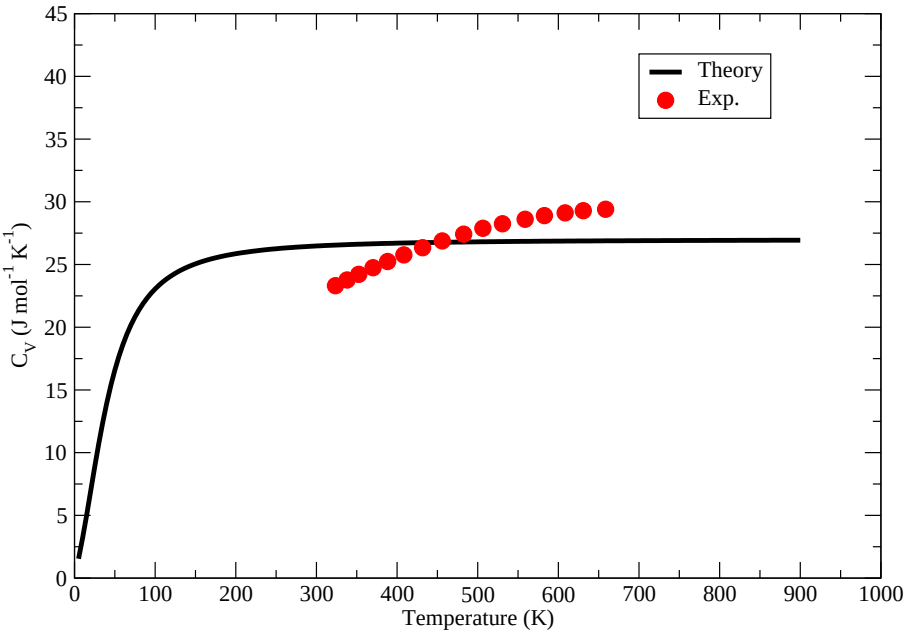


Figure 4.17: Theoretical and experimental heat capacity curves for cubic GST. Experimental data is due to Kalb [114].

cubic GST, the experimental heat capacity is slightly larger than the calculated heat capacity at high temperatures. According to Tsafack *et al* [8], theory does not adequately take into account the contribution of vacancies to the heat capacity. The theoretical curves exhibit the same trend as experimental curves. Moreover, the theoretical curves give an idea of how the heat capacity behaves for temperature ranges where experimental data are not available, in this case $T < 300$ K for the hexagonal phase and $T < 400$ K for the cubic phase.

Fig 4.18 shows the dependence of internal energy, $U$, on temperature, $T$,

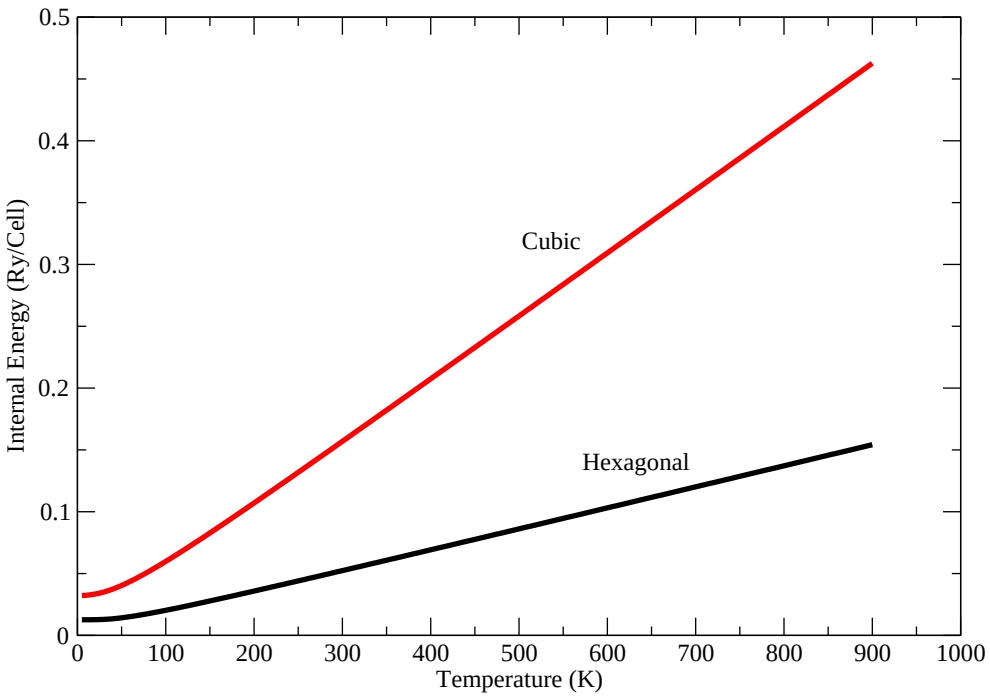


Figure 4.18: Internal energy as a function of temperature for hexagonal and cubic GST.

for hexagonal and cubic GST. Using the first law of thermodynamics:

$$\begin{aligned} dU &= dQ - pdV \\ &= C_v dT - pdV, \end{aligned} \tag{4.3}$$

where $Q$ is heat, $P$ is pressure and $V$ is volume. That is, the only way of changing the internal energy of a system is by raising its temperature ($C_v dT$) or by doing work on it ($-pdV$). However, for solids the term $pdV$ is insignificant and the internal energy is a function of temperature only. Hence, the internal energy is proportional to temperature in agreement with this work.

Fig. 4.19 shows the dependence of entropy on temperature for hexagonal GST. The entropy is usually referenced to its value at very low temperatures,

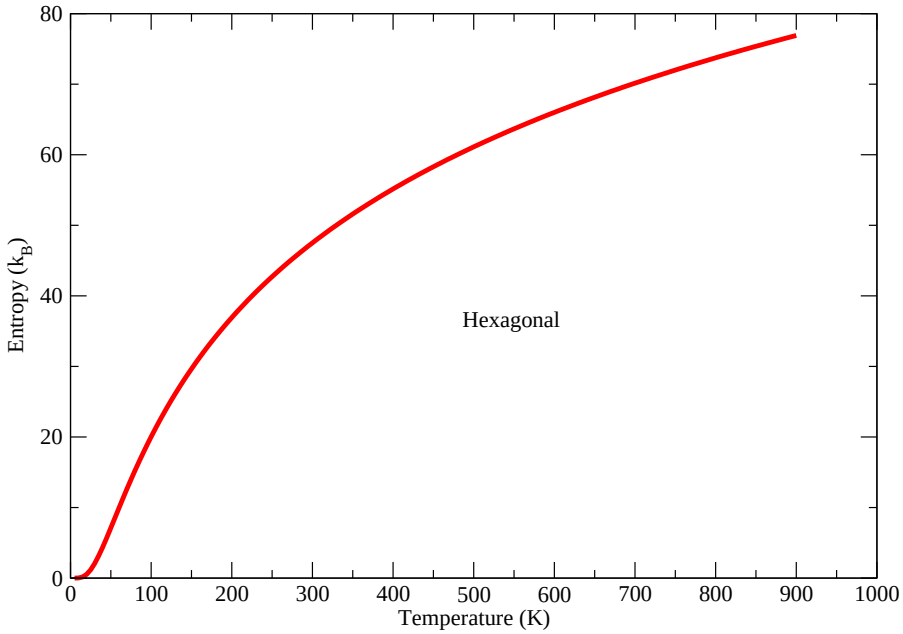


Figure 4.19: Dependence of entropy on temperature for hexagonal GST.

which (according to the law of thermodynamics) equals zero, that is:

$$\lim_{T \to 0} S = 0. \tag{4.4}$$

However, this law only holds for a system having a non-degenerate ground state. A system with a $g_0$-fold degenerate ground state results in a residual entropy at $T = 0$, that is:

$$S(T = 0) = k_B log(g_0). \tag{4.5}$$

It is clear from Fig. 4.19 that the entropy of the hexagonal phase goes to zero upon cooling to 0 K, in agreement with one experimental study [113]. In that study, the cubic phase was found to have a residual entropy at $T = 0$. The

configurational entropy is defined in general by:

$$S_{conf} = -k_B ln(W), \tag{4.6}$$

where $W$ is the number of possible configurations of the whole system for a given energy. Thus, single crystals have no configurational entropy. Compounds from the pseudobinary line $(GeTe)_m(Sb_2Te_3)_n$ possess a large configurational entropy in the metastable cubic phase due to substitutional disorder on the $Ge/Sb$/v sub-lattice [113]. Hexagonal (stable) GST does not have lattice disorder and hence the entropy becomes zero at 0 K. At high temperatures, a system becomes disorderly and unpredictable. Hence, entropy is proportional to temperature.

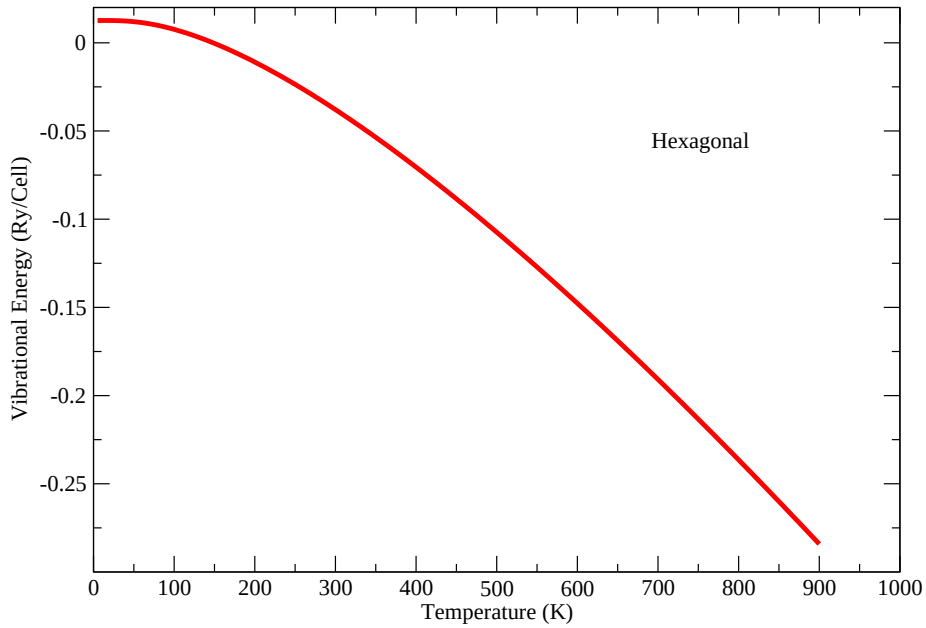


Figure 4.20: Dependence of vibrational energy on temperature for hexagonal GST.

Fig. 4.20 shows the calculated vibrational energy as a function of tempera-

ture for hexagonal GST. All quantum harmonic oscillators undergo fluctuations even in their ground state ($T = 0$ K) and the associated energy is then known as the *zero-point* energy. This is in agreement with this study where a zero-point energy of 0.0126 Ry/atom was calculated for hexagonal GST. Vibrational energy increases with temperature. The negative values of energy is an indication that these states are bound states, that is, energy must be expended to cause fluctuations in atomic positions.

As noted previously, cubic GST is metastable, and hence it has some imaginary (or negative) vibrational frequencies. This brings with it challenges in calculating some thermal quantities such as entropy and vibrational energy using `QHA` code as it is currently.

## 4.4 Electronic Properties

### 4.4.1 Band Structure and Density of States

The calculated band structures and the associated electronic DOS are shown in Figs. 4.21-4.24. For LDA calculations, hexagonal GST is almost semimetallic (Fig. 4.21), that is, the top of the valence band and the bottom of the conduction band are non-degenerate at Γ. On the other hand, cubic GST has a direct band gap of about 0.08 eV at Γ with a marginal intrusion of the Fermi level into the valence band (Fig. 4.23). GGA calculations show that hexagonal GST has a direct band gap of about 0.33 eV at Γ (Fig. 4.22) whereas cubic GST has a direct band gap of about 0.24 eV at Γ and an indirect band gap of about 0.04 eV along the Γ-K line (Fig. 4.24). In general, LDA and GGA results in this work give band gaps that are less than the measured optical band gap of 0.5 eV for both phases [38, 39]. In comparison, Lee and Jhi [40] have calculated an indirect band gap of about 0.26 eV along the Γ-K line for the sequence of Kooi and de Hosson [41]. In yet another theoretical study, Tsafack *et al* found out that hexagonal GST is semi-metallic whereas the cubic phase had a direct

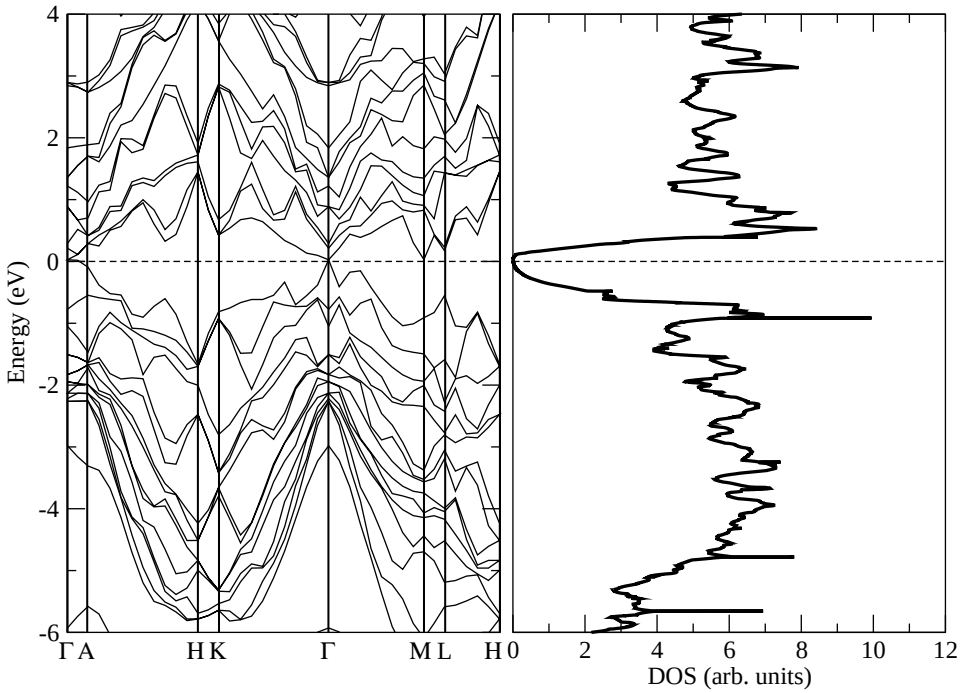


Figure 4.21: The LDA band structure and the associated DOS (right) for hexagonal GST. The Fermi level is shifted to zero.

band gap of about 0.2 eV at Γ and an indirect band gap of about 0.1 eV along the Γ-K line.

Differences in the calculated bad gap values between the theoretical studies mentioned above and this study lies in the approximation for the XC energy functional and treatment of $Te$ $4d$ electrons. The use of different XC terms and the treatment of $Te$ 4 electrons as core or semicore results in different lattice constants and hence band gap values.

The underestimation of band gaps (Appendix A) is a well-known effect of DFT calculations since DFT is a ground state theory and does not take into account many-body effects. This can be corrected through the use of hybrid functionals, projector augmented wave (PAW) methods, DFT + $U$, Quantum

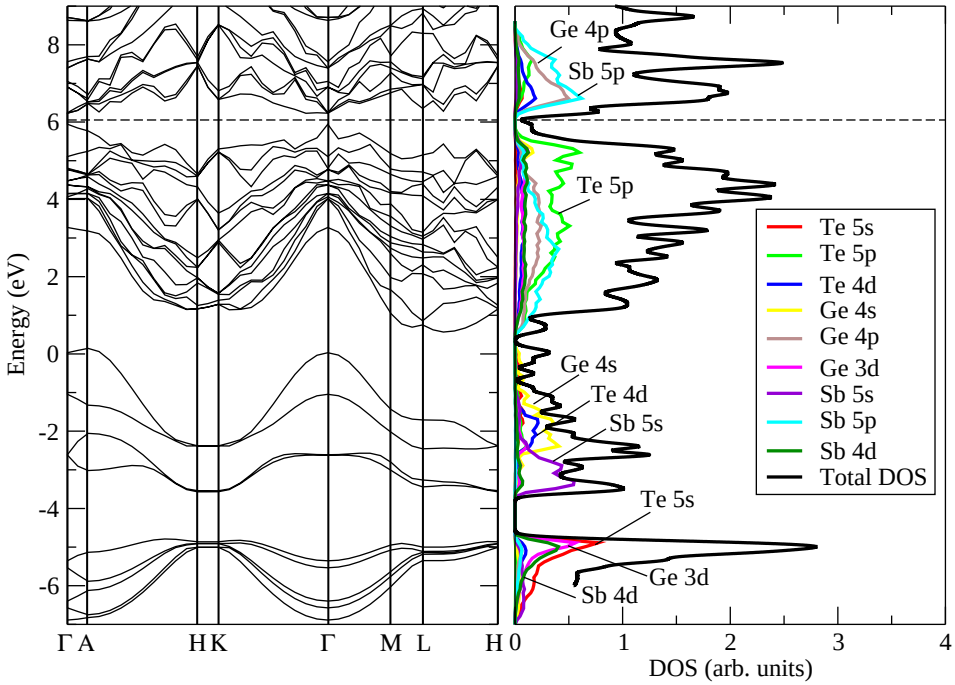


Figure 4.22: The GGA band structure and the associated DOS (right) for hexagonal GST. The Fermi level is shifted to zero.

Monte Carlo (QMC) methods, MBPT and TDDFT. Using PAW method with GGA, Park *et al* [104] have calculated band gap values of 0.41 eV and 0.51 eV for hexagonal and cubic GST, respectively.

In Figs. 4.25 and 4.26, the variation of band gap values with lattice parameters is predicted. In this analysis, the LDA was considered for the XC energy functional. The band gap is almost zero at the equilibrium lattice constants ($c/a$=4.02 for hexagonal GST and $c/a$=12.26 for cubic GST) as expected. However, the band gap increases with rising $a$ (falling $c/a$) up to some maximum value, then falls off. For hexagonal GST, the band gap is maximum ($\sim$ 0.22 eV) at around $c/a$=3.49 whereas for the cubic phase, the band gap is maximum ($\sim$ 0.23 eV) at around $c/a$=10.62. The dependence of the band gap

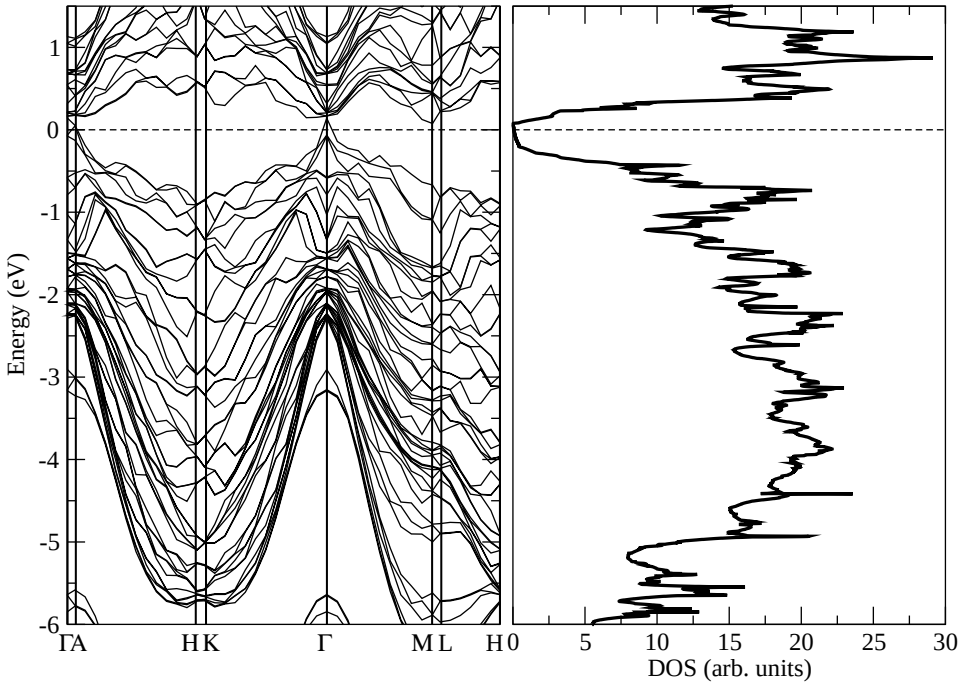


Figure 4.23: The LDA band structure and the associated DOS (right) for cubic GST. The Fermi level is shifted to zero.

on lattice parameters suggests the possibility of tuning electronic properties of GST for various applications.

In order to get a more detailed picture of the electronic structure and bonding in crystalline GST, the projected density of states (PDOS) for hexagonal and cubic GST structures were obtained. These are included in Figs. 4.22 and 4.24 for hexagonal and cubic GST, respectively. The PDOS gives the contribution of individual atomic orbitals to the band structure. In calculating the PDOS, the GGA was considered for the XC energy functional. In addition, the semicore $Ge$ $3d$, $Sb$ $4d$ and $Te$ $4d$ orbitals were included in the valence states. It is evident that there is a certain amount of orbital overlap or hybridization in hexagonal and cubic GST, which is an indication of covalent bonding in

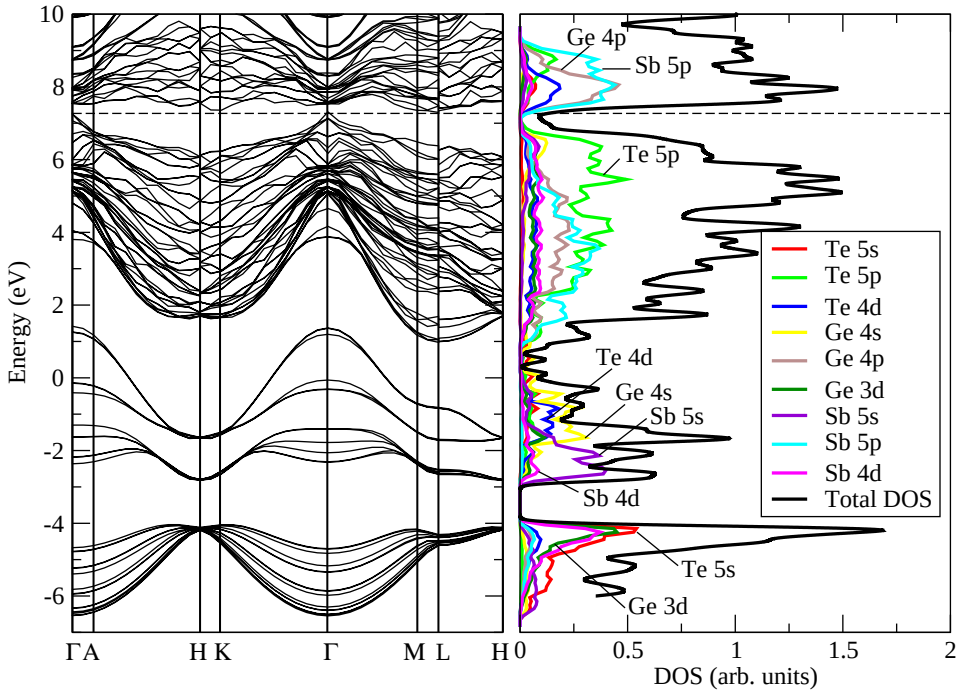


Figure 4.24: The GGA band structure and the associated DOS (right) for of cubic. The Fermi level is shifted to zero.

GST. In both phases, the $Ge$ $s$, $Sb$ $s$, $Te$ $s$, $Ge$ $d$, $Sb$ $d$ and $Te$ $d$ orbitals are located inside the valence band whereas the $Ge$ $p$, $Sb$ $p$ and $Te$ $p$ orbitals are centered near the Fermi level ($\sim$ 7.4 eV). Hence, the $Ge$ $s$, $Sb$ $s$, $Te$ $s$, $Ge$ $d$, $Sb$ $d$ and $Te$ $d$ electrons are more tightly bound than the $Ge$ $p$, $Sb$ $p$ and $Te$ $p$ electrons. Specifically, the $Te$ $5s$, $Sb$ $4d$ and $Ge$ $3d$ orbitals are located deeper in the valence band, suggesting that they are more tightly bound as compared to the $Ge$ $4s$, $Sb$ $5s$ and $Te$ $4d$ orbitals, which are shifted slightly towards the Fermi level. X-ray photoemission spectroscopy (HX-PES) studies by Kim *et al* [116] established that peaks at the lowest binding energy are due to the $Ge$ $4p$, $Sb$ $5p$ and $Te$ $5p$ orbitals; peaks at the second lowest binding energy are due to the $Ge$ $4s$ and $Sb$ $5s$ orbitals; peaks at the highest binding energy are due

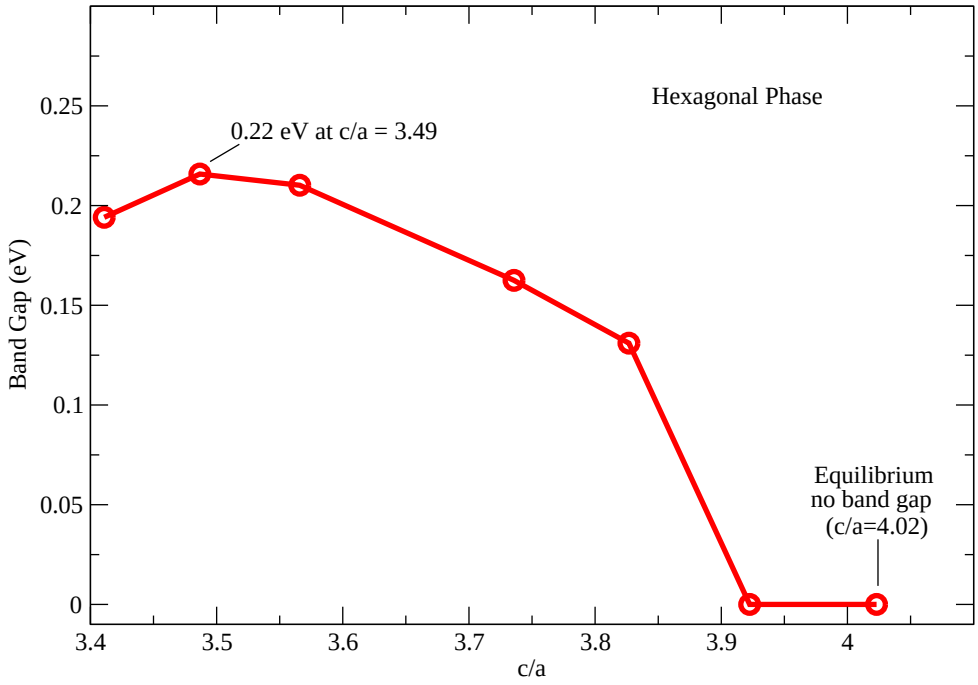


Figure 4.25: Dependence of band gap on lattice parameters $c$ and $a$ for hexagonal GST.

to the $Te$ $5s$ orbital. This is in agreement with this work. Kim *et al* [116] confirmed that such a three-peak structure is characteristic of $(GeTe)_m(Sb_2Te_3)_n$ pseudobinary compounds including $Ge_2Sb_2Te_5$ (GST), which is the subject of this study.

Figs. 4.27 and 4.28 show the calculated band structures along high-symmetry lines for pure and nitrogen-doped GST. The Fermi level is shifted to zero. It is evident that the band gap vanishes with rising $N$ content for both hexagonal and cubic GST. However, Lai *et al* [117] have determined from optical measurements that the optical band gap increases with rising $N$-content, indicating a reduction (an increase) in conductivity (resistivity). Two mechanisms are responsible for the reduction in resistivity with rising $N$-content: Grain

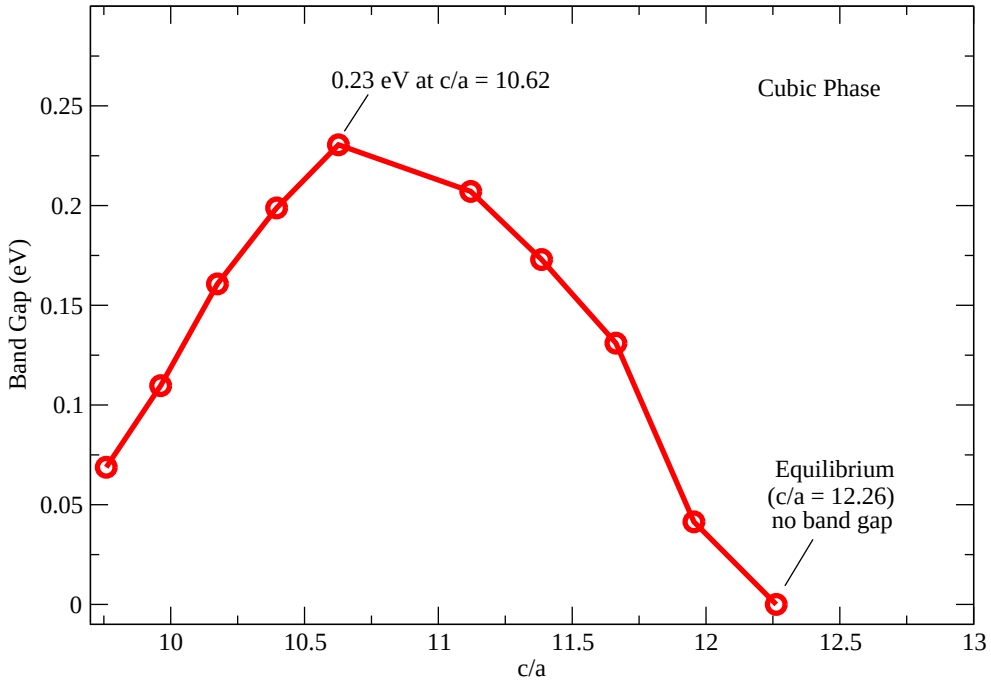


Figure 4.26: Dependence of band gap on lattice parameters $c$ and $a$ for cubic GST.

boundary scattering of mobile carriers and a shift of the Fermi level towards the middle of the band gap due to the relatively larger electronegativity value of $N$ as compared to $Ge$, $Sb$ and $Te$. Clearly, the band structure diagrams do not support the latter case. Thus, the scattering of mobile carriers at grain boundaries could explain the increase in resistivity with rising $N$ content.

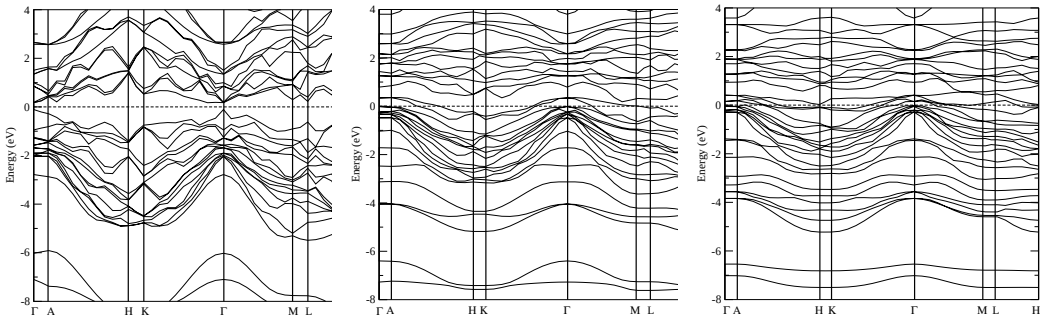


Figure 4.27: Band structure of pure (left) and doped hexagonal GST with nitrogen at 10 at. % (center) and at 25 at. % (right).

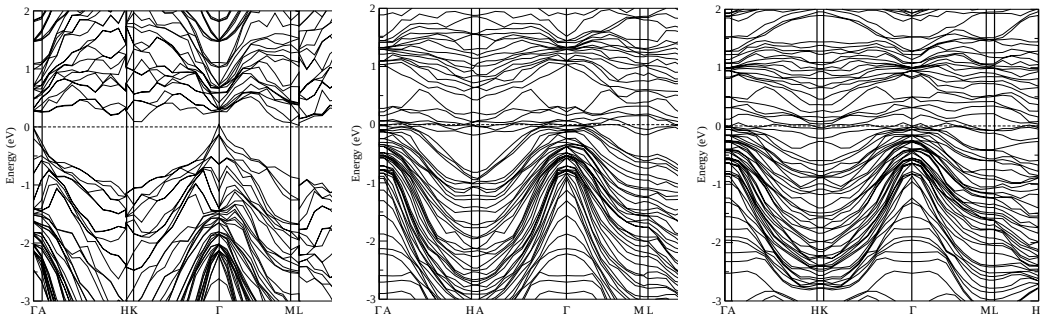


Figure 4.28: Band structure of pure (left) and doped cubic GST with nitrogen at 10 at. % (center) and at 25 at. % (right).

## 4.5 Optical Properties

### 4.5.1 Dielectric Function, Optical Conductivity and Reflectivity Contrast

In Fig. 4.29, the real and imaginary parts of the dielectric function for hexagonal and cubic GST are compared. For both phases, Re($\varepsilon$) is negative in the energy range 1-4 eV. It is evident that for hexagonal GST, Re($\varepsilon$) is even more negative within the same range. Negative values in the real part of the dielectric function are characteristic of metallic systems. This is in agreement with electrical measurements, which indicate that hexagonal GST has metallic-like

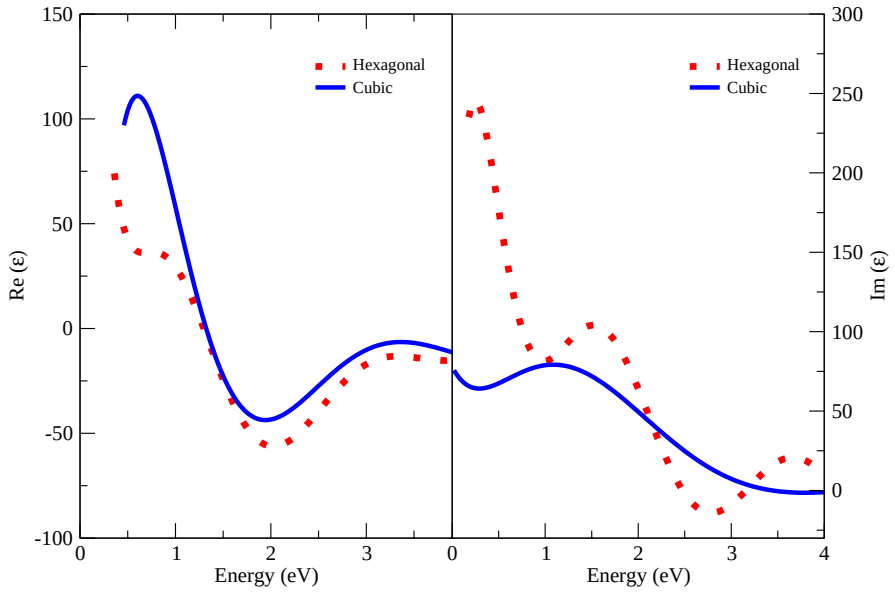


Figure 4.29: A comparison of the real and imaginary parts of the dielectric function for hexagonal and cubic GST.

conductivity [118]. Generally, Re($\varepsilon$) becomes positive at lower energies, in agreement with experiment [118]. The imaginary part of the dielectric function, Im($\varepsilon$), shows a narrower and stronger absorption edge at low energies for the hexagonal phase, in agreement with experiment [118]. This is of special interest since the energy of the semiconductor infrared laser beam used for the write, read and erase operations in optical disk technology is in this range. In Fig. 4.30, the real and imaginary parts of the dielectric function for hexagonal and cubic GST, respectively, are compared with experiment [119] and other theoretical calculations [8]. It is evident that the curves have similar trends. In Fig. 4.31, the real and imaginary parts of the optical conductivity as functions of $N$-content are shown for hexagonal and cubic GST. The real part of optical conductivity, associated with free current, decreases with rising $N$-content in the spectral range 0.5-3 eV. From I-V characteristics, Lai *et al* [117] have shown that the resistivity of crystalline GST increases with rising $N$-content at all annealing temperatures (that is, wether hexagonal or cubic).

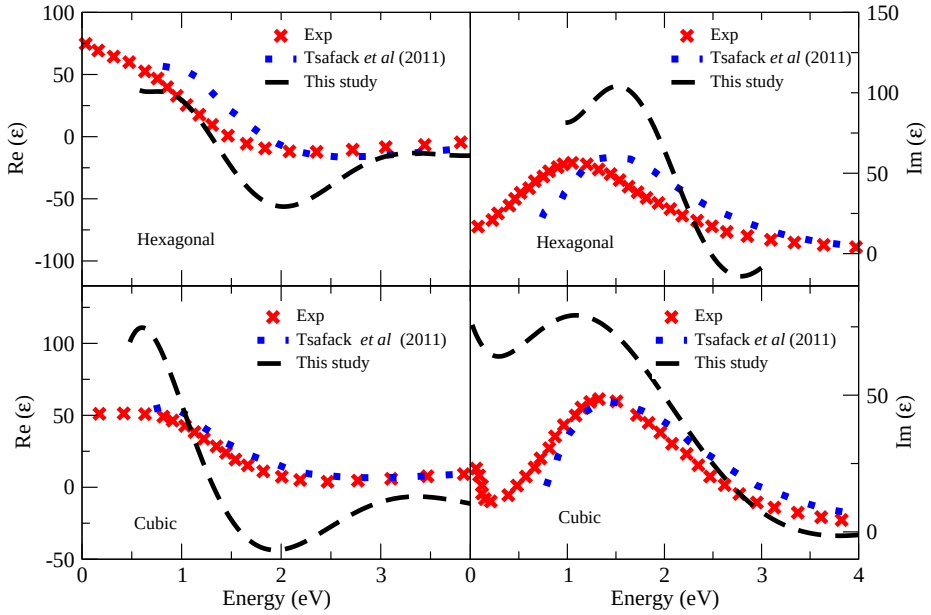


Figure 4.30: Real and imaginary dielectric function for hexagonal and cubic GST as compared to experiment and other calculations.

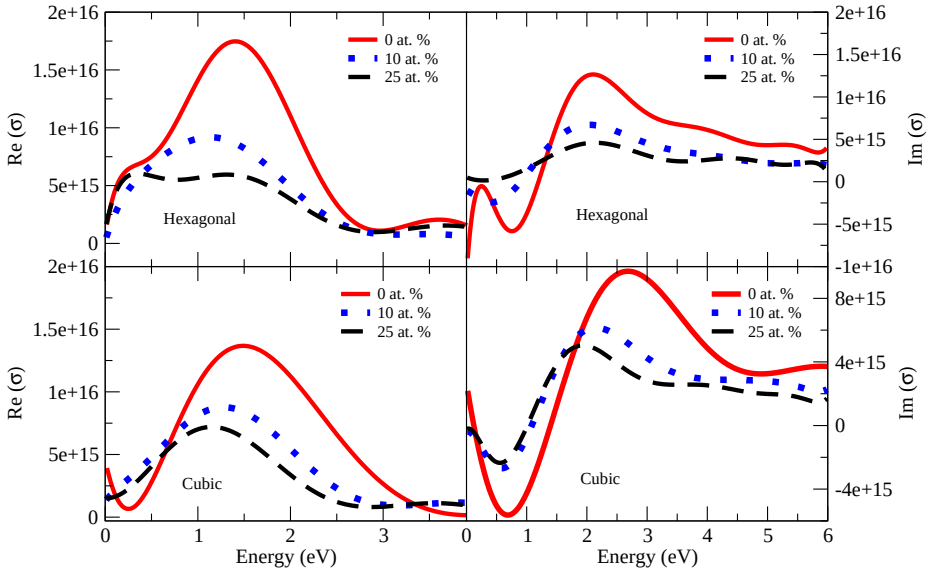


Figure 4.31: Dependence of real and imaginary optical conductivity on nitrogen content for hexagonal and cubic GST.

Two possible reasons can be given for the increase (decrease) in resistivity (conductivity). One is grain boundary scattering. According to the theory of grain boundary scattering [120], carriers can be scattered by grain boundaries during transportation. Some doped nitrogen existing in the grain boundaries suppress grain growth resulting in more grain boundaries and these act as scattering centers for carriers, resulting in an increase (decrease) in resistivity (conductivity). The second reason is the movement of the Fermi level. In crystalline GST, $N$ acts like an acceptor ( due to its relatively larger electronegativity value), making the Fermi level move toward the middle of the band gap, resulting in an increase (decrease) in resistivity (conductivity). Thus, the writing current can be successfully reduced through $N$-doping and this is important for practical application of GST in high-density non-volatile random access memory.

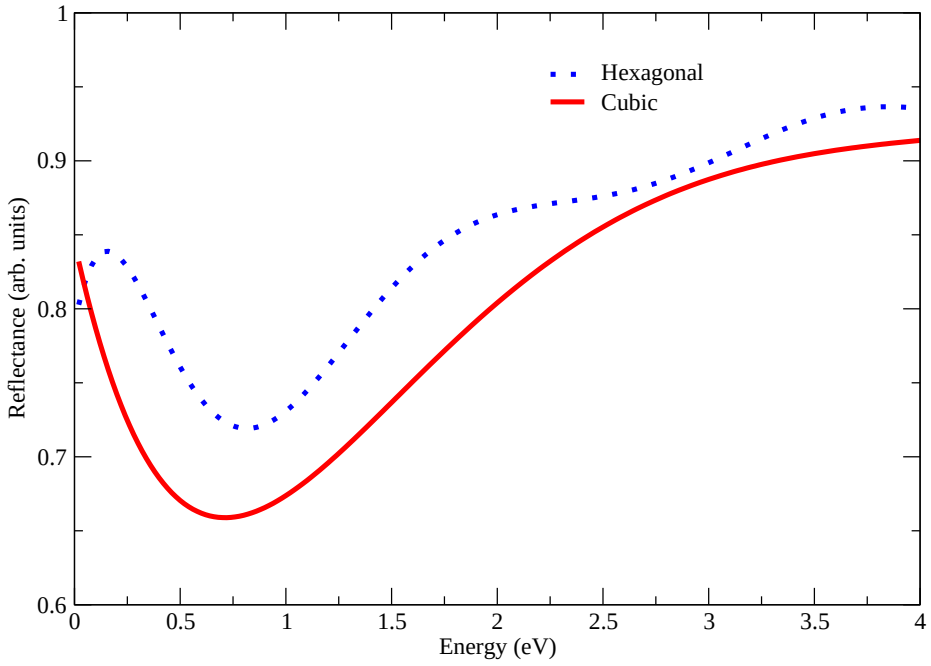


Figure 4.32: Comparison of the reflectivities of hexagonal and cubic GST.

Reflectivity is one of the most important parameters considered in optical phase-change storage. In Fig. 4.32, the reflectivity of hexagonal GST is

compared to that of cubic GST. It turns out that the maximum difference in reflectivity between hexagonal and cubic GST is about 8% and this happens in the spectral range 0.5-1.75 eV, which is the range of application for GST. Using optical ellipsometry, García *et al* [118] have shown that the reflectivity increases by about 7% when samples are transformed from the cubic phase to the hexagonal phase. Fig. 4.33 shows the calculated reflectivity contrast for pure GST as compared to experiment [95] and other theoretical studies [95]. It is evident that the profiles are similar. Moreover, the reflectivity contrast is seen to rise towards the red and infrared spectral range (1-2 eV), which is the range of application of GST [121].

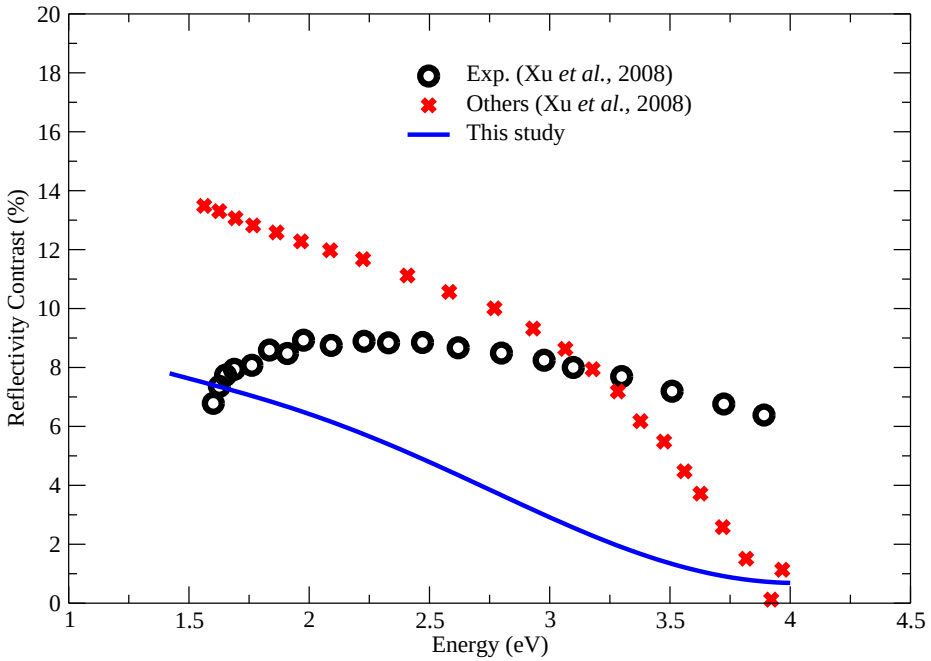


Figure 4.33: Calculated reflectivity contrast as compared to experiment and other theoretical studies.

A main driving force in the search for new materials is to decrease the wavelength of the laser used for writing, reading and erasing bits. By decreasing

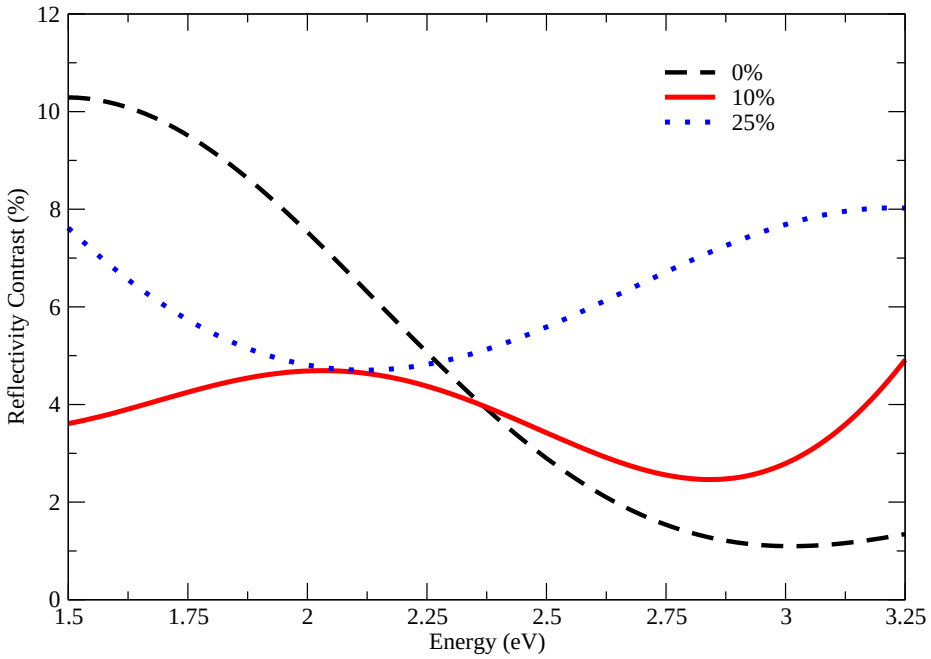


Figure 4.34: Dependence of reflectivity contrast on nitrogen content.

the wavelength, the size of the written bits decreases and, as a result, the storage density increases. As already noted in this study and others [121], GST possesses a large reflectivity contrast in the red and infrared spectral range and is therefore used in CDs and DVDs. If the optical contrast can be optimized at shorter wavelengths, then GST can be used in hight-density optical media such as DVD and Blu-ray disks. Fig. 4.34 shows the dependence of the reflectivity contrast on $N$-content as calculated in this study. It is clear that pure GST has a higher reflectivity contrast in the red and infrared region (1-2 eV). However, $N$-doped GST has a higher reflectivity contrast in the visible and ultraviolet region (2.5-3.5 eV) and this reflectivity contrast increases with rising $N$-content for the levels of doping considered here (10-25 at. %). Thus, in $N$-doping lies the possibility of reducing the size of the written bits by lowering the wavelength of the writing laser. One experimental study [122] shows that $Ag$-doped GST has a higher reflectivity contrast in the blue laser wavelength. At the time of writing, there was no theoretical or experimental

study on $N$-controlled reflectivity contrast of GST.

### 4.5.2 Optical Absorption

Figs. 4.35 and 4.36 show the calculated optical absorption spectra for hexagonal and cubic GST, respectively. For the hexagonal phase, a major peak at about 0.48 eV and a minor peak at about 1.65 eV are observed in the spectrum calculated using TDDFT whereas the spectrum calculated using $GW_0$ gave a major peak at about 0.21 eV and a minor peak at about 1.30 eV.

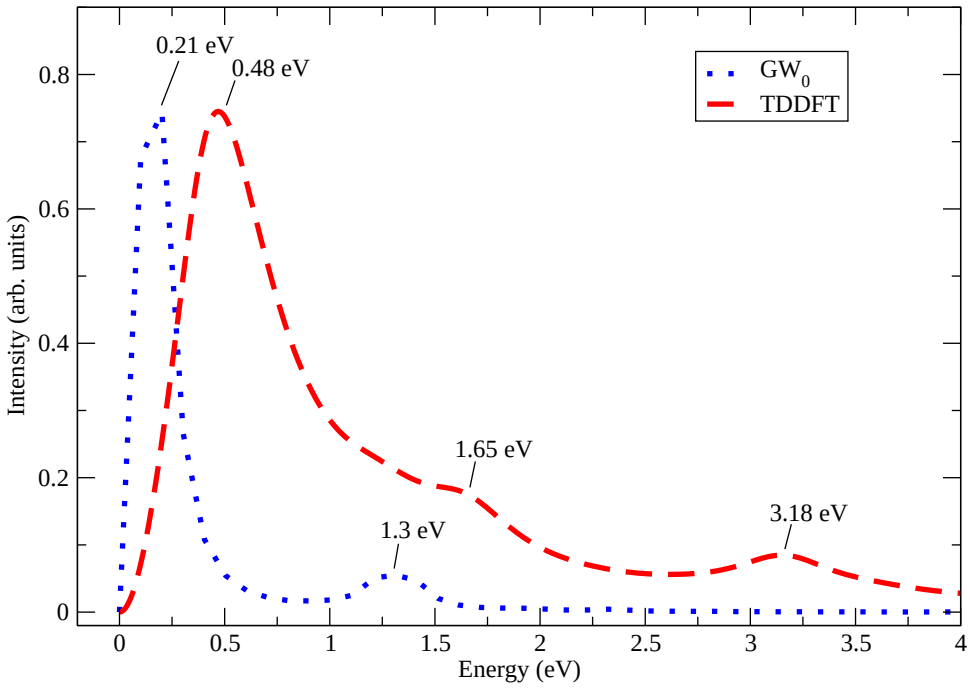


Figure 4.35: Calculated optical absorption spectra for hexagonal GST.

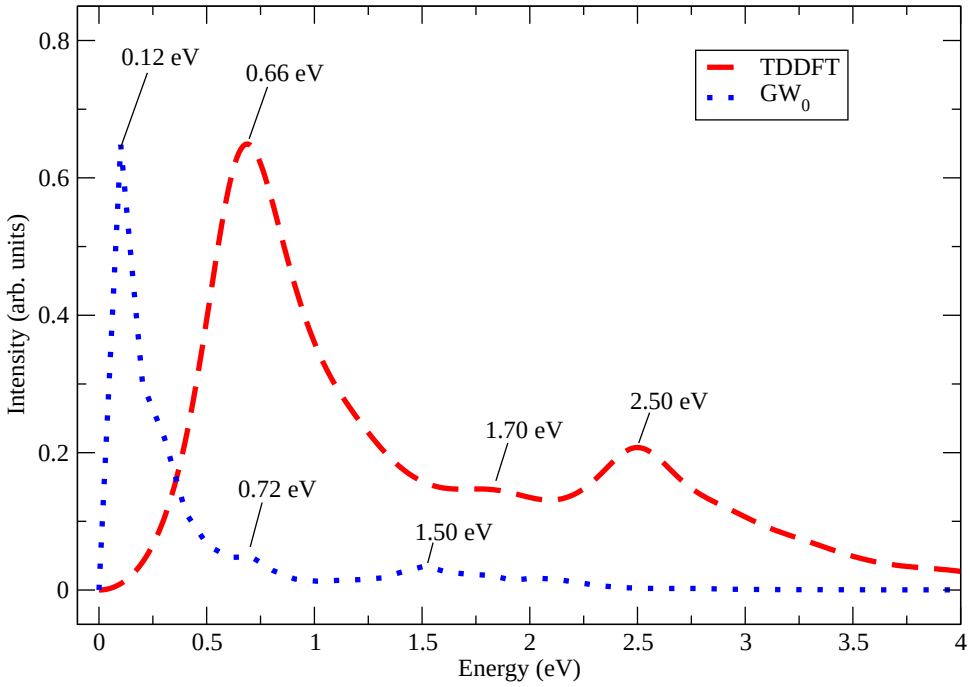


Figure 4.36: Calculated optical absorption spectra for cubic GST.

For the cubic phase, TDDFT gave a major peak at about 0.66 eV and a minor peak at about 1.70 eV whereas $GW_0$ gave a major peak at about 0.12 eV and a minor peak at about 1.50 eV. Major peaks in the calculated spectra correspond to the onset of absorption and they give an estimate of the optical band gap. Minor absorption peaks (peaks at higher energies) in the calculated spectra correspond to optical excitations of unbound states. Experimental findings of Sun *et al* [123] show that the valence band of thermally crystallized GST films (cubic phase) is dominated by $Te$ $p$, $Ge$ $p$ and $Sb$ $p$ states with minor contributions from $Ge$ $s$ and $Sb$ $s$ states, whereas the conduction band is mainly populated by anti-bonding $Ge$ $p$/$Sb$ $p$ states and $Te$ $p$ states. Anti-bonding states are known to be higher in energy and hence less stable than bonding states. Orava *et al* [124] have assigned a peak at 1.77 eV in the

spectrum of cubic GST system to transitions between $Te\ p$ bonding states and $Ge\ p/Sb\ p$ anti-bonding states. Such a peak is obtained in this study for the cubic GST system at 1.70 eV using TDDFT and at 1.50 eV using $GW_0$. Yamanaka *et al* [125] have assigned a peak at 1.8 eV in the spectrum of hexagonal GST structure to transitions between $Te\ p$ and $Sb\ p$ states. Such a peak is obtained in this study for the hexagonal GST system at 1.65 eV using TDDFT and at 1.30 eV using $GW_0$. In general, TDDFT gives better estimates to the optical band gap of GST than the partially self-consistent $GW_0$. To improve on the results of $GW_0$, the fully self-consistent $GW$ is needed. However, as noted earlier, $GW$ is designed for the analysis of excited states of the $(N \pm 1)$ electron systems. Treatment of optical absorption processes where the particle number remains constant requires a two-particle Green function, which leads to the Bethe-Salpeter equation (BSE) of MBPT. TDDFT also treats constant-particle systems. In this study, $GW$ and BSE were not possible since the Yambo code does not go beyond $GW_0$ for metallic or near metallic systems such as $Ge_2Sb_2Te_5$.

# Summary and Conclusions

This study has dealt with first principles calculation of the structural, electronic, optical and thermal properties of hexagonal and cubic GST.

Calculation of thermal properties was performed within the framework of quasi-harmonic approximation as implemented in the code `QHA` within Quantum ESPRESSO distribution. The calculated heat capacity curves are found to exhibit the same trend as experimental curves. Moreover, the calculated heat capacity is found to exceed the classical Dulong-Petit limit at hight temperatures for both hexagonal and cubic $Ge_2Sb_2Te_5$, in agreement with the experimental trend. This effect has been attributed to lattice defects, lattice vacancies in this case. When lattice vacancies are thermally generated, their heat of formation gives an extra contribution to the heat capacity of the crystal. The calculated entropy of hexagonal $Ge_2Sb_2Te_5$ is found to vanish at 0 K, in agreement with the fact that for a system with a non-degenerate ground-state, the entropy should vanish at 0 K. Configurational disorder results in a non-zero entropy at 0 K. Hence, in this study, hexagonal $Ge_2Sb_2Te_5$ has been shown not to have configurational disorder in its ground state, in agreement with experimental studies. The thermal calculations have validated the structural models used in this study as well as the theoretical model used to calculate their properties.

Processes such as optical absorption that involve electronic excitations are out of reach of density functional theory. In this study, the optical absorption spectra of hexagonal and cubic GST have been calculated using the Liouville-Lanczos approach to time-dependent density functional theory as implemented in the Quantum ESPRESSO distribution and many body perturbation theory with the partially self-consistent $GW_0$ approximation to the electronic self en-

ergy as implemented in the Yambo code. Time-dependent density functional calculations give optical band gaps of about 0.48 eV and 0.66 eV for hexagonal and cubic GST, respectively, in reasonably good agreement with experimental studies, which suggest a value of 0.5 eV for both GST phases.

This study has considered the effect of nitrogen doping on the optical properties of hexagonal and cubic GST. The relative concentration of nitrogen was set to 10-20 at. %. Pure GST is found to have a high reflectivity contrast in the spectral range 1-2 eV, in agreement with experimental studies. However, nitrogen-doped GST is found to have a high reflectivity contrast towards shorter wavelengths (2.5-3.5 eV). The reflectivity contrast is found to rise with increasing nitrogen content within 10-20 at. % doping levels. Hence, nitrogen doping of GST provides a way to decrease the wavelength of the writing laser, thereby increasing data storage density in optical memory applications.

# Recommendations

There are a number of additional areas for further research that have been highlighted by the study undertaken in this thesis. They include:

1. Calculation of the temperature variation of entropy for cubic $Ge_2Sb_2Te_5$ using alternative methods such as molecular dynamics (MD).

2. Analysis of pressure-induced structural transformation in hexagonal and cubic $Ge_2Sb_2Te_5$.

# References


[1] **Ovshinsky SR**. Reversible Electrical Switching Phenomena in Disordered Structures. *Phys. Rev. Lett. 21*: 1450, 1968.

[2] **Libera M and Chen M**. Time-Resolved Reflection and Transmission Studies of Amorphous Ge-Te Thin-Film Crystallization. *J. Appl. Phys. 73*: 2272, 1993.

[3] **Yamada N**. Erasable Phase-Change Optical Materials. *Mater. Res. Bull. 21*: 48, 1996.

[4] **Trappe C, Béchevet B, Facsko S and Kurz H**. Real Time Measurement of Phase Change Dynamics. *Jpn. J. Appl. Phys. 37*: 2114, 1998.

[5] **Meijer GI**., Who Wins the Non-Volatile Memory Race? *Science 319*: 1625, 2008.

[6] **Wuttig M and Yamada N**. Phase Change Materials for Rewritable Data Storage. *Nat. Mater. 6*: 824, 2007.

[7] **Yamada N and Matsunaga T**. Structure of Laser-Crystallized $Ge_2Sb_{(2+x)}Te_5$ Sputtered Thin Films for Use in Optical Memory. *J. Appl. Phys. 88*: 7020, 2000.

[8] **Tsafack T, Piccinini E, Lee BS, Pop E and Rudan M**. Electronic, Optical and Thermal Properties of the Hexagonal and Rock Salt-Like $Ge_2Sb_2Te_5$ Chalcogenide from First-Principle Calculations. *J. Appl. Phys. 110*: 063716, 2011.

[9] **Giannozzi P, Baroni S, Bonini N, Calandra M, Car R, Cavazzoni C, Ceresoli D, Chiarotti GL, Cococcioni M, Dabo I, Dal Corso A, Fabris S, Fratesi G, de Gironcoli S, Gebauer R, Gerstmann U, Gougoussis C, Kokalj A, Lazzeri M, Martin-Samos L, Marzari**

**N, Mauri F, Mazzarello R, Paolini S, Pasquarello A, Paulatto L, Sbraccia C, Scandolo S, Sclauzero G, Seitsonen AP, Smogunov A, Umari P and Wentzcovitch RM**. QUANTUM ESPRESSO: A Modular and Open-Source Software Project for Quantum Simulation of Materials. *J. Phys.: Condens. Matter. 21*: 395502, 2009.

[10] **Hohenberg P and Kohn W**. Inhomogeneous Electron Gas. *Phys. Rev B 136*: 864, 1964.

[11] **Kohn W and Sham LJ**. Self-Consistent Equations Including Exchange and Correlation Effects. *Phys. Rev. A 140*: 1133, 1965.

[12] **Thomas LH**. The Calculation of Atomic Fields. *Proc. Cambridge Phil. Soc. 23*: 542, 2004.

[13] **Fermi E**. Un Metodo Statistico per la Determinazione di alcune Priorieta' dell'Atomo. *Rend. Accad. Naz. Lincei 6*: 602, 1927.

[14] **Perdew JP and Zunger A**. Self-Interaction Correction to Density-Functional Approximations for Many-Elecetron Systems. *Phys. Rev. B 23*: 5048, 1981.

[15] **Payne MC, Teter MP, Allan DC, Arias TA and Joannopoulos JD**. Iterative Minimization Techniques for Ab Initio Total-Energy Calculations: Molecular Dynamics and Conjugate Gradients. *Rev. Mod. Phys. 64*: 1045, 1992.

[16] **Filippi C, Umrigar CJ and Taut M**. Comparison of Exact and Approximate Density Functionals for an Exactly Soluble Model. *J. Chem. Phys. 100*: 1290, 1994.

[17] **Perdew JP, Burke K and Ernzerhof M**. Generalized Gradient Approximation Made Simple. **Phys. Rev. Lett. 77**: 3865, 1996.

[18] **Ortiz G and Ballone P**. Pseudopotentials for Non-Local-Density Functionals. *Phys. Rev. B 43*: 6376, 1991.

[19] **Ortiz G**. Gradient-Corrected Pseudopotential Calculations in Semiconductors. *Phys. Rev. B 45*: 11328, 1992.

[20] **Garcia A, Elsässer C, Zhu J, Louie SG and Cohen ML**. Use of Gradient-Corrected Functionals in Total-Energy Calculations for Solids. *Phys. Rev. B 46*: 9829, 1992.

[21] **Filippi C, Singh DJ, Umrigar CJ**. All-Electron Local-Density and Generalized-Gradient Calculation of the Structural Properties of Semiconductors. *Phys. Rev. B 50*: 14947, 1994.

[22] **Lee C, Vanderbilt D, Laasonen K, Car R and Parrinello M**. Ab Initio Studies on High Pressure Phases of Ice. *Phys. Rev. Lett. 69*: 462, 1992.

[23] **Sim F, St. Amant A, Papai I and Salahub DR**. Gaussian Density Functional Calculations on Hydrogen-Bonded Systems. *J. Am. Chem. Soc. 114*: 4391, 1992.

[24] **Laasonen K, Sprik M, Parrinello M and Car R**. "Ab Initio" Liquid Water. *J. Chem. Phys. 99*: 9080, 1993.

[25] **Dal Corso A and Resta R**. Density-Functional Theory of Macroscopic Stress: Gradient-Corrected Calculations for Crystalline Se. *Phys. Rev. B 50*: 4327, 1994.

[26] **Dal Corso A and Resta R**. Density-Functional Theory of the Dielectric Constant: Gradient-Corrected Calculation for Silicon. *Phys. Rev. B 49*: 5323, 1994.

[27] **Perdew JP and Wang Y**. (unpublished); **Perdew JP**. Unified Theory of Exchange and Correlation Beyond the Local Density Approximation. In: Electronic Structure of Solids '91, edited by Ziesche P and Eschrig H, Berlin: Akademie Verlag, 1991.

[28] **Dal Corso A, Pasquarello A and Baldereschi A**. General-Gradient Approximations to Density-Functional Theory: A Comparative Study for Atoms and Solids. *Phys. Rev. B 53*: 1180, 1996.

[29] **Becke AD**. Density-Functional Thermochemistry. IV. A New Dynamical Correlation Functional and Implications for Exact-Exchange Mixing. *J. Chem. Phys. 104*: 1040, 1996.

[30] **Krieger JB, Chen J, Iafrate GJ and Savin A**. In: Electron Correlation and Material Properties, edited by Gonis A and Kioussis N, New York: Plenum, 1999.

[31] **Tao J, Perdiew JP, Staroverov VN, Scuseria GE**. Climbing the Density-Functional Ladder: Nonempirical Meta-Generalized Gradient Approximation Desined for Molecules and Solids. *Phys. Rev. Lett. 91*: 146401, 2003.

[32] **Van Voorhis T and Scuseria GE**. A Novel Form for the Exchange-Correlation Energy Functional. *J. Chem. Phys. 109*: 400, 1998.

[33] **Becke AD**. Density-Functional Exchange-Energy Approximation with Correct Asymptotic Behavior. *Phys. Rev. A 38*: 3098, 1988.

[34] **Hamprecht FA, Cohen AJ, Tozer DJ, Handy NC**. Development and Assessment of New Exchange-Correlation Functionals. *J. Chem. Phys. 109*: 6264, 1998).

[35] **Schmider HL and Becke AD**. Optimized Density Functionals from the Extended G2 Test Set. *J. Chem. Phys. 108*: 9624, 1998.

[36] **Lee C, Yang W and Parr RG**. Development of the Colle-Salvetti Correlation-Energy Formula into a Functional of the Electron Density. *Phys. Rev. B 37*: 785, 1988.

[37] **Adamo C and Barone VJ**. Exchange Functionals with Improved Long-Range Behaviour and Adiabattic Connection Methods Without Adjustable Paramemeters: The mPW and mPW1PW models. *J. Chem. Phys. 108*: 664, 1998.

[38] **Kato T and Tanaka K**. Electronic Properties of Amorphous and Crystalline $Ge_2Sb_2Te_5$ Films. *Jpn. J. Appl. Phys. 44*: 7340, 2005.

[39] **Lee BS, Abelson JR, Bishop SG, Kang DH, Cheong B and Kim KB**. Investigation of the Optical and Electronic Properties of $Ge_2Sb_2Te_5$ Phase Change Material in its Amorphous, Cubic and Hexagonal Phases. *J. Appl. Phys. 97*: 093509, 2005.

[40] **Lee G and Jhi SH**. Ab Initio Study of the Structural and Electronic Properties of the Crystalline $Ge_2Sb_2Te_5$. *Phys. Rev. B 77*: 153201, 2009.

[41] **Kooi BJ and de Hosson JTM**. Electron Diffraction and High-Resolution Transmission Electron Microscopy of the High Temperature Crystal Structures of $Ge_xSb_2Te_{(3+x)}$ (x=1, 2, 3) Phase Change Material. *J. Appl. Phys. 92*: 3584, 2002.

[42] **Marques MAL and Gross EKU**. Time-Dependent Density Functional Theory. In: Lecture Notes in Physics, A Primer in Density Functional Theory, edited by Fiolhais C, Nogueira F and Marques MAL, Berlin: Springer, 2003.

[43] **Runge E and Gross EKU**. Density Functional Theory for Time-Dependent Systems. *Phys. Rev. Lett. 52*: 997, 1984.

[44] **Leeuwen R**. Causality and Symmetry in Time-Dependent Density-Functional Theory. *Phys. Rev. Lett. 80*: 1280, 1998.

[45] **Ullrich CA, Gossmann UJ and Gross EKU**. Time-Dependent Optimized Effective Potential. *Phys. Rev. Lett. 74*: 872, 1995.

[46] **Gross EKU and Kohn W**. Local Density-Functional Theory of Frequency-Dependent Linear Response. *Phys. Rev. Lett. 55*: 2850, 1985.

[47] **Petersilka M, Grossmann UJ and Gross EKU**. Excitation Energies from Time-Dependent Density-Functional Theory. *Phys. Rev. Lett. 76*: 1212, 1996.

[48] **Casida ME**. In: Recent Advances in Density Functional Methods, Part I, edited by Chong DP, Singapore: World Scientific, 1995.

[49] **Castro A, Appel H, Oliveira M, Rozzi CA, Marques MAL, Gross EKU and Rubio A**. Octopus: A Tool for the Application of Time-Dependent Density Functional Theory. *Phys. Stat. Sol. B 243*: 2465, 2006.

[50] **Marques MAL, Castro A, Bertsch GF and Rubio A**. Octopus: A First-Principles Tool for Excited Electron-Ion Dynamics. *Compt. Phys. Comm. 151*: 60, 2003.

[51] **Walker B, Saitta AM, Gebauer R and Baroni S**. Efficient Approach to Time-Dependent Density-Functional Perturbation Thoery for Optical Spectroscopy. *Phys. Rev. Lett. 96*: 113001, 2006.

[52] **Malcioğlu OB, Gebauer R, Rocca D and Baroni S**. turboTDDFT-A Code for the Simulation of Molecular Spectra using the Liouville-Lanczos Approach to Time-Dependent Density-Functional Perturbation Theory. **Comp. Phys. Commun. 182**: 1744, 2011.

[53] **Friedrich C and Schindlmayr A**. Many-Body Perturbation Theory: The GW Approximation. In: Computational Nanoscience: Do it Yourself, edited by Grotendorst J, Blügel S and Max D, Jülich: John von Neumann Institute for Computing, NIC Series, 2006.

[54] **Godby RW and González PG**. Density Functional Theories and Self-Energy Approaches. In: A Primer in Density Functional Theory, edited by Fiolhais C, Nogueira F and Marques MAL, Heidelberg: Springer, 2003.

[55] **Kittel C**. Introduction to Solid State Physics. New York: John Wiley & Sons, 1996.

[56] **Wallace DC**. Thermodynamics of Crystals. New York: Dover, 1998.

[57] **Born M and Oppenheimer R**. On the Quantum Theory of Molecules. *Annalen der Physik 84*: 457, 1927.

[58] **Martin RM**. Electronic Structure: Basic Theory and Practical Methods. Cambridge: Cambridge University Press, 2004.

[59] **DeCicco PD and Johnson FA**. Quantum Theory of Lattice Dynamics. *IV Proc. R. Soc. London A 310*: 111, 1969.

[60] **Pick RM, Cohen MH and Martin RM**. Microscopic Theory of Force Constants in the Adiabatic Approximation. *Phys. Rev. B 1*: 910, 1970.

[61] **Baroni S, de Gironcoli S, Dal Corso A and Giannozzi P**. Phonons and Related Crystal Properties from Density-Functional Perturbation Theory. *Rev. Mod. Phys. 73*: 515, 2001.

[62] **Baroni S and Debernardi A**. 3rd-Order Density-Functional Perturbation Theory - A Practical Implementation with Applications to Anharmonic Couplings in Si. *Solid State Commun. 91*: 813, 1994.

[63] **Debernardi A, Baroni S and Molinary E**. Anharmonic Phonon Lifetimes in Semiconductors from Density Functional Perturbation Theory. *Phys. Rev. Lett. 75*: 1819, 1995.

[64] **Lazzeri M, Calandra M and Mauri F**. Anharmonic Phonon Frequency Shift in $MgB_2$. *Phys. Rev. B 68*: 220509, 2003.

[65] **Bonini N, Lazzeri M, Marzari N and Mauri F**. Phonon Anharmonicities in Graphite and Graphene. *Phys. Rev. Lett. 99*: 176802, 2007.

[66] **Yao D, Zhou X, Wu L, Song Z, Cheng L, Rao F, Liu B and Feng S**. Investigation on Nitrogen-Doped $Ge_2Sb_2Te_2$ Material for Phase Change Memory Applications. **Solid-State Electron 79**: 138, 2013.

[67] **Liu B, Song Z, Zhang T, Feng S and Chen B**. Effect of N-Implantation on the Structural and Electrical Characteristics of $Ge_2Sb_2Te_5$ Phase Change Film. **Thin Solid Films 478**: 49, 2005.

[68] **Jang MH, Park SJ, Lim DH, Cho M-H, Do KH, Ko D-H and Sohn HC**. Phase Change Behavior of Oxygen Incorporated $Ge_2Sb_2Te_5$ Films. *Appl. Phys. Lett. 95*: 012102, 2009.

[69] **Xu C, Liu B Song ZT, Feng SL and Chen B**. Characteristics of Sn-Doped $Ge_2Sb_2Te_5$ Films Used for Phase-Change Memory. *Chin. Phys. Lett. 22*: 2929, 2005.

[70] **Ling Y, Lin Y, Quiao B, Lai Y, Feng J, Tang T, Cai B and Chen B**. Effects of Si Doping on Phase Transition of $Ge_2Sb_2Te_5$ Films by In Situ Resistance Measurements. *Jpn. J. Appl. Phys. 45*: L349, 2006.

[71] **Kojima R, Okabayashi S, Kashihara T, Horai K, Matsunaga T, Ohno E, Yamada N and Ohta T** Nitrogen Doping Effect on Phase Change Optical Disks. *Jpn. J. Appl. Phys. 37*: 2098, 1998.

[72] **Xia J-L, Liu B, Song Z-T., Feng S-L. and Chen B**. Electrical Properties of Ag-Doped $Ge_2Sb_2Te_5$ Films Used for Phase Change Random Access Memory. *Chn. Phys. Lett. 2005*: 934, 2005.

[73] **Popescu M, Velea A, Sava F, Lőrinczi A, Tomescu A, Simion C, Matei E, Socol G, Mihailescu IN, Andonie A and Stamatin I**. Steucture and Properties of Silver Doped $SnSe_2$ and $Ge_2Sb_2Te_5$ Thin Films Prepared by Pulsed Laser Deposition. *Phys. Status Solidi A 207*: 516, 2010.

[74] **Wang K, Steimer C, Wamwangi D, Ziegler S and Wuttig M**. Effect of Indium Doping on $Ge_2Sb_2Te_5$ Thin Films for Phase-Change Optical Storage. *Appl. Phys. A 80*: 2005.

[75] **Wełnic W and Matthias W**. Reversible Switching in Phase Change Materials. *Mater. Today 11*: 20, 2008.

[76] **Gonze X, Stumpf R and Scheffler M**. Analysis of Separable Potentials. *Phys. Rev. B. 44*: 8503, 1990.

[77] **Goedecker S, Teter M and Hutter J**. Separable Dual-Space Gaussian Pseudopotentials. *Phys. Rev. B. 54*: 1703, 1996.

[78] **Hartwigsen C, Goedecker S and Hutter J**. Relatisistic Separable Dual-Space Gaussian Pseudopotentials from H to Rn. *Phys. Rev. B 58*: 3641, 1998.

[79] **Do GS, Kim J, Jhi SH, Louie SG and Cohen ML**. Ab Initio Calculations of Pressure-Induced Structural Phase Transitions of $GeTe$. *Phys. Rev. B. 82*: 054121, 2010.

[80] **Van Lenthe E, Snijders JG, Baerends EJ**. The Zero-Order Regular Approximation for Relativistic Effects: The Effect of Spin-Orbit Coupling in Closed Shell Molecules. *J. Chem. Phys. 105*: 6505, 1996.

[81] **Monkhorst HJ and Pack JD**. Special Points for Brillouin Zone Integration. *Phys. Rev. B 13*: 5188, 1976.

[82] **Petrov II, Imanov RM and Pinsker ZG**. Electron-Diffraction Determination of the Structure of $Ge_2Sb_2Te_5$ and $GeSb_4Te_7$. *Kristallografiya 13*: 339, 1968.

[83] **Matsunaga T, Yamada N and Kubota Y**. Structures of Stable and Metastable $Ge_2Sb_2Te_5$, an Intermetallic Compound in the $GeTe - Sb_2Te_3$ Pseudobinary Systems. *Acta Crystallogr. B 60*: 685, 2004.

[84] **Kokalj A**. Computer Graphics and Graphical User Interfaces as Tools in Simulations of Matter at the Atomic Scale. *Comp. Mater. Sci. 28*: 155, 2003.

[85] http://www.xcrysden.org/ [Jan. 2016].

[86] **Park YJ, Lee JY, Youm MS and Lee HS**. Crystal Structure and Atomic Arrangement of the Metastable $Ge_2Sb_2Te_5$ Thin Films Deposited on $SiO_2$/Si Substrates by Sputtering Method. *J. Appl. Phys 97*: 093506, 2005.

[87] **Kolobov AV, Frenkel AI, Fons P, Ankudinov AL, Tominaga J and Uriga T**. Understanding the Phase-Change Mechanism of Rewritable Optical Media. *Nature Mater. 3*: 703, 2004.

[88] **Nonaka T, Ohbayashi G, Toriumi Y, Mori Y and Hashimoto H**. Crystal Structure of $GeTe$ and $Ge_2Sb_2Te_5$ Meta-Stable Phase. *Thin Solid Films 370*: 258, 2000.

[89] **Kolobov AV, Fons P, Tominaga J, Frenkel AI, Ankudinov AL, Yannopoulos SN, Andikopoulos KS and Uruga T**. Why Phase-Change Media are Fast and Stable: A New Approach to an Old Problem. *Jpn. J. Appl. Phys. 44*: 3345, 2005.

[90] **Miller FM**. Chemistry: Structure and Dynamics. New Yor: McGraw Hill, 1984.

[91] **Murnaghan FD**. The Compressibility of Media under Extreme Pressures. *Proc. Nat. Acad. Sci. 30*: 224, 1944.

[92] **Baroni S, Giannozzi P and Esaev E**. Thermal Properties of Materials from Ab Initio Quasi-Harmonic Phonons. *Rev. Mineral. and Geochem. 71*: 39, 2010.

[93] **Maxwell JC**. A Dynamical Theory of the Electromagnetic Field. *Phil. Trans. Royal Soc. 155*: 459, 1865.

[94] **Jackson JD**. Classical Electrodynamics. New York: John Wiley, 1975.

[95] **Xu M, Wei S-J, Wu S, Pei F, Li J, Wang SY and Chen LY**. Theoretical and Experimental Unvestigations of the Optical Properties of $Ge_2Sb_2Te_5$ for Multi-State Optical Data Storage. *JKPS 53*: 2265, 2008.

[96] **Marini A, Hogan C, Grüning M and Varsano D**. Yambo: An Ab Initio Tool for Excited State Calculations. *Comp. Phys. Comm. 180*: 1392, 2009.

[97] **Krbal M, Kolobov AV, Haines J, Fons P, Levelut C, Le Parc R, Hanfland M**. Initial Structure Memory of Pressure-Induced Changes in the Phase-Change Alloy $Ge_2Sb_2Te_5$. *Phys. Rev. Lett. 103*: 115502, 2009.

[98] **Sosso GC, Caravati S, Gatti C, Assoni S and Bernasconi N**. Vibrational Properties of Hexagonal $Ge_2Sb_2Te_5$ from First Principles. *J. Phys.: Condens. Matter. 21*: 245401, 2009.

[99] **Becke AD**. Density-Functional Thermochemistry. III. The Role of Exact Exchange. *J. Chem. Phys. 98*: 5648, 1993.

[100] **Sun Z, Zhou J and Ahuja R**. Structure of Phase Change Materials for Data Storage. *Phys. Rev. Lett. 96*: 055507, 2006.

[101] **Sousa SF, Fernandes PA and Ramos MJ**. General Performance of Density Functionals. *J. Phy. Chem. A 111*: 10439, 2007.

[102] **Lee G-D, Lee MH, Ihm J**. Role of d-Electrons in the Zinc-Blend Semiconductors ZnS, ZnSe, and ZnTe. *Phys. Rev. B 52*: 1459, 1995.

[103] **Khenata R, Bouhemadou A, Sahnoun M, Reshack AH, Baltache H and Rabah M**. Elastic, Electronic and Optical Properties of ZnS, ZnS and ZnTe under Pressure. *Comput. Mater. Sci. 38*: 29, 2006.

[104] **Park J, Eom SH, Lee H, Da Silva JLF, Kang YS, Lee TY, Khang YH**. Optical Properties of Pseudobinary $GeTe$, $Ge_2Sb_2Te_5$, $Ge_1Sb_2Te_5$ and $Sb_2Te_3$ from Fllipsometry and Density Functional Theory. *Phys. Rev. B 80*: 115209, 2009.

[105] **Da Silva JLF, Walsh A and Lee H**. Insight into the Structure of the Stable and Metastable $(GeTe)_m(Sb_2Te_3)_n$ Compounds. *Phys. Rev. B 78*: 224111, 2008.

[106] **Jeong TH, Kim MR, Seo H, Park JW and Yeon C**. Crystal Structure and Microstructure of Nitrogen-Doped $Ge_2Sb_2Te_5$. *Jpn. J. Appl. Phys. 39*: 2775, 2000.

[107] **Akola J and Jones RO**. Density Functional Study of Amorphous, Liquid and Crystalline $Ge_2Sb_2Te_5$ Homopolar Bonds and/or AB Alternation. *J. Phys.: Condens. Matter 20*: 465103, 2008.

[108] **Kolobov AV, Haines J, Pradel A, Ribes M, Fons P and Tominaga J**. Pressure-Indiced Site-Selective Disordering of $Ge_2Sb_2Te_5$: A New Insight into Phase-Change Optical Recording. *Phys. Rev. Lett. 97*: 035701, 2006.

[109] **Kolobov AV, Haines J, Pradel A, Ribes M, Fons P, Tominaga J, Steimer C, Aquilanti G and Pascarelli S**. Pressure-Induced Amorphization of Quasi-Binary $GeTe - Sb_2Te_3$: The Role of Vacancies. *Appl. Phys. Lett. 91*: 021911, 2007.

[110] **Krbal M, Kolobov AV, Haines J, Pradel A, Ribes M, Fons P, Tominaga J, Levelut C, Le Parc R and Hanfland M**. Temperature Independence of Pressure-Induced Amorphization of the Phase-Change Memory Alloy $Ge_2Sb_2Te_5$. *Appl. Phys. Lett. 93*: 031918, 2008.

[111] **Siegrist T, Merkelbach P and Wuttig M**. Phase Change Materials: Challenges on the Path to a Universal Storage Device. *Annu. Rev. Condens. Matter Phys. 3*: 215, 2012.

[112] **Zalden P, Siegert KS, Rols S, Fischer SE, Schlich F, Hu T and Wuttig M**. Specific Heat of $(GeTe)_x(Sb_2Te_3)_{1-x}$ Phase-Change Materials: The Impact of Disorder and Unharmonicity. *Chem. Mater. 26*: 2307, 2014.

[113] **Zalden PE**. Phase-Change Materials: Structure, Vibrational States and Thermodynamics of Crystallization. PhD Thesis, RWTH Aachen University, 2012.

[114] **Kalb JA**. Stresses, Viscous Flow and Crystallization Kinetics in Thin Films of Amorphous Chalcogenides used for Optical Data Storage. PhD Thesis, RWTH Aachen University, 2002.

[115] **Kuwahara M, Suzuki O, Yamakawa Y, Taketoshi M, Yagi T, Fons P, Fukaya T, Tominaga J and Baba T**. Temperature Dependence of the Thermal Properties of Optical Memmory Materials. *Jpn. J. Appl. Phys. 46*: 3909, 2007.

[116] **Kim JJ, Kobayashi K, Ikenaga E, Kobata M, Ueda S, Matsunaga T, Kifune K, Kojima R, Yamada N**. Electronic Structure of Amorphous and Crystalline $(GeTe)_{1-x}(Sb_2Te_3)_x$ Investigated Using Hard X-Ray Photoemission Spectroscopy. *Phys. Rev. B 76*: 115124, 2007.

[117] **Lai Y, Qiao B, Feng J, Ling Y, Lai L, Tang T, Cai B and Chen B**. Nitrogen-Doped $Ge_2Sb_2Te_5$ Films for Nonvolatile Memory. *J. Elect. Mater. 34*: 176, 2005.

[118] **García-García E, Mendoza-Galván A, Vorobiev Y, Moralez-Sánchez E, González-Hernándes J, Matínez G and Chao BS**. Optical Properties of Ge:Sb:Te Ternary Alloys. *J. Vac. Sci. Technol. A 17*: 1805, 1999.

[119] **Shportko K, Kremers S, Woda M, Lencer D, Robertson J and Wuttig M**. Resonant Bonding in Crystalline Phase Change Materials. *Nat. Mater. 7*: 653, 2008.

[120] **Hoffmann KE and Schmoranzer H**. Inelastic and Elastic Multiple Scattering of Fast Electrons Described by a Transport Equation. In: Electrom Beam Interactons with Solids, AMF O'Hare, Il: SEM Inc., 1984.

[121] **Yamada N, Kojima R, Uno M, Akiyama T, Kitaura H, Narumi K and Nishiuchi K**. Phase-Change Material for Use in Rewritable Dual-Layer Optical Disk. *Proc. SPIE 4342*: 55, 2002.

[122] *Lie C-T., Kuo P-C, Hsu W-C, Wu T-H, Chen P-W and Chen S-C.* $Ge_2Sb_2Te_5$ Thin Film Doped with Silver. *Jpn. J. Appl. Phys. 42*: 1026, 2003.

[123] **Sun Z, Kyrsta S, Music D, Ahuja R and Schneider JM**. Structure of the $Ge - Sb - Te$ Phase Change Materials Studied by Theory and Experiment. *Solid State Comm. 143*: 140, 2007.

[124] **Orava J, Wagner T, Sik J, Prikryl J, Frumar M and Benes L**. Optical Properties and Phase Change Transition in $Ge_2Sb_2Te_5$ Flash Evaporated Thin Films Studied by Temperature Dependent Spectroscopic Ellipsometry. *J. Appl. Phys. 104*: 043523, 2008.

[125] **Yamanaka S, Ogawa S, Morimoto I and Ueshima Y**. Electronic Structures and Optical Properties of $GeTe$ and $Ge_2Sb_2Te_5$. *Jpn. J. Appl.Phys. 37*: 3327, 1998.

# Publications Arising Out of the Study

1. **Odhiambo H and Othieno H**. *Ab Initio* Study of the Structural, Vibrational and Thermal Properties of $Ge_2Sb_2Te_5$. *IJCMSE 2*: 1550009-1, 2015.

2. **Odhiambo H, Amollo G, Makau N, Dusabirane F. Othieno H and Oduor A**. *Ab Initio* Study of the Electronic and Optical Properties of Hexagonal and Cubic $Ge_2Sb_2Te_5$. *ARP 10*: 69, 2015.

# Relevant Schools and Conferences Attended

1. *1st-31st May, 2016*: Condensed Matter and Statistical Physics (CMSP) Section, The Abdus Salam International Centre for Theoretical Physics (ICTP), Trieste, Italy.

2. *2nd-6th December, 2013*: Centre for High Performance Computing (CHPC) National Meeting, Cape Town International Convention Centre, Republic of South Africa.

3. *3rd-7th December, 2012*: Centre for High Performance Computing (CHPC) National Meeting, Durban International Convention Centre, Republic of South Africa.

4. *28th May-8th June, 2012*: African School on Electronic Structure Methods and Applications (ASESMA), University of Eldoret, Kenya.

# Appendices

## Appendix A
## Underestimation of the Band Gap in DFT

This theoretical treatment of the underestimation of band gaps in DFT is based on Ref. [8].

If one electron in the state $\upsilon$ is removed from the system, $E_N - E_{N-1} = \epsilon_\upsilon$, where $E_N$ is the energy of the system with $N$ electrons. Likewise, an addition of an electron in the state $c$ leads to $E_{N+1} - E_N = \epsilon_c$. The difference between the largest addition energy and the smallest removal energy defines the energy band gap

$$E_g = \epsilon_c - \epsilon_\upsilon = E_{N-1} + E_{N+1} - 2E_N. \qquad (A.1)$$

In solids, this is the onset of the continuum of optical transitions, if the gap is direct (if the lowest empty state and the highest filled state have the same $k$ vector). From atomic and molecular physics, the highest occupied and the lowest unoccupied states are respectively called HOMO (Highest Occupied Molecular Orbital) and LUMO (Lowest Unoccupied Molecular Orbital), while addition and removal energy are respectively refereed to as electron affinity, **A**, and ionization potential, **I**. Due to the discontinuity of the XC potential, it is safe to say, $E_g = \mathbf{I} - \mathbf{A}$ which in turn can be written as

$$\begin{aligned} E_g &= \mu(N+\delta) - \mu(N-\delta), \\ &= \left.\frac{\delta E}{\delta n(\mathbf{r})}\right|_{N+1} - \left.\frac{\delta E}{\delta n(\mathbf{r})}\right|_{N-1}, \end{aligned} \qquad (A.2)$$

where $\delta \to 0$. This is substituted into the explicit Kohn-Sham form for the energy functional, $E[n(\mathbf{r})]$. The Hartree and external potential terms of the functional will yield no discontinuity and no contribution to $E_g$. Only the kinetic and XC terms may have a discontinuity and contribute to $E_g$. For a non-interacting system, only the kinetic term contributes, and the gap is exactly given by the auxiliary non-interacting system gap

$$\begin{aligned} E_g^0 &= \left.\frac{\delta T_0}{\delta n(\mathbf{r})}\right|_{N+1} - \left.\frac{\delta T_0}{\delta n(\mathbf{r})}\right|_{N+1}, \\ &= \epsilon_{LUMO} - \epsilon_{HOMO}. \end{aligned} \tag{A.3}$$

It is remarked that even the kinetic energy of non-interacting electrons, considered as a function of the density, must have a discontinuous derivative when crossing an integer number of electrons. This is one reason why it is so difficult to produce explicit functionals of the charge density for $T_0$ that are able to yield good results: no single functional form will yield the discontinuity, but this is needed in order to get the correct energy spectrum. For the interacting system

$$\begin{aligned} E_g &= \left.\frac{\delta T_0}{\delta n(\mathbf{r})}\right|_{N+1} - \left.\frac{\delta T_0}{\delta n(\mathbf{r})}\right|_{N+1} + \left.\frac{\delta E_{XC}}{\delta n(\mathbf{r})}\right|_{N+1} - \left.\frac{\delta E_{XC}}{\delta n(\mathbf{r})}\right|_{N-1}, \\ &= E_g^0 + E_g^{xc}. \end{aligned} \tag{A.4}$$

Note that the kinetic energy term is evaluated at the same charge density as for the non-interacting system, so it coincides with the auxiliary non-interacting system gap. By virtue of eqn. (A.4), the gaps calculated through DFT are not by construction equal to the true gap because they are missing a term, $E_g^{xc}$, coming from the discontinuity of derivatives of XC functionals. This is absent by construction from any current approximated functional, be it LDA, GGA or more complex. There is some evidence that this missing term is responsible for a large part of the band gap problem, at least in common semiconductors.